7-2017

Sensitivity Enhancement of Metal-Oxide Chemical Sensors for Detection of Volatile Organic Compounds

John F. Hughes
jfh4193@rit.edu

Recommended Citation

Hughes, John F., "Sensitivity Enhancement of Metal-Oxide Chemical Sensors for Detection of Volatile Organic Compounds" (2017). Thesis. Rochester Institute of Technology. Accessed from

Sensitivity Enhancement of Metal-Oxide Chemical Sensors for Detection of Volatile Organic Compounds

JOHN F. HUGHES

Sensitivity Enhancement of Metal-Oxide Chemical Sensors for Detection of Volatile Organic Compounds

By
John F. Hughes
A Thesis Submitted in Partial Fulfillment
of the Requirements for the Degree of
Master of Science
in
Microelectronic Engineering

Approved by

Dr. Lynn Fuller, *Advisor* Date
Professor

Dr. Karl Hirschman, *Committee Member* Date
Director, SMFL, Professor

Dr. Michael Jackson, *Committee Member* Date
Associate Professor

Dr. Sohail Dianat Date
Department Head, Electrical and Microelectronic Engineering

Dr. Robert Pearson Date
Program Director, Microelectronic Engineering

Department of Electrical and Microelectronic Engineering

R·I·T | KATE GLEASON
College of ENGINEERING

Rochester Institute of Technology
Rochester, New York
July 2017

Acknowledgements

I would like to thank the technicians and process engineers of the RIT SMFL for their consistent help and dedication for making this thesis possible, especially John Nash and Peter Morici, who have dedicated so much time in helping me with equipment certification and facilitating chemical chamber testing in the semiconductor parameter analyzer laboratory.

I would like to thank Dr. Pearson, Dr. Gupta, and Dr. Kurinec for their time and effort in materials analysis and simulation work.

I would like to thank my colleague Timothy Tong for his support in peer-editing my manuscript and giving his valuable advisement in the development of this document.

Lastly, I would like to thank my committee members Dr. Hirschman and Dr. Jackson for their time and assistance. Thank you Dr. Fuller for giving me both the opportunity to work with you and valuable insights regarding my research.

Dedication

To my family, my friends, and my wonderful significant other.

Abstract

Metal-oxide chemical sensor technology has been praised as a cheap and efficient method of detecting both reducing and oxidizing gases depending on the metal-oxide's carrier type. The research conducted in this thesis explored methods of enhancing the sensitivity of an n-type metal-oxide material (indium tin oxide, ITO) to a volatile organic compound (VOC) through changes in both device and testing characteristics. Two methods of testing prototype sensors were developed which consisted of short and long-term exposure to ethanol at different temperatures and concentrations. Maximum sensitivity at 2000 ppm was achieved in devices with thin, annealed metal-oxide layers with a high temperature of operation; this sensitivity measurement was achieved using a prolonged exposure test with 100-nm of annealed ITO at an operating temperature of 360°C and yielded a sensitivity of 32.5%. A fabrication process consisting of two lift-off processes for the metal-oxide and contact metal was developed to create the prototype devices. Preliminary characterization on the metal-oxide materials confirmed its thickness, crystallinity / crystal structure, and grain size. In addition to the electrical tests, a future work chemical sensor was thermally and electrically simulated using SolidWorks and Silvaco Atlas, respectively; a proposed fabrication process of the device is also presented, along with a basic outline of future work experiments to further study sensitivity enhancements through other metal-oxide materials, noble catalytic metals, device architecture, and signal processing of proposed electrical testing.

Contents

List of Figures

List of Tables

List of Equations

Chapter 1

Thesis Background and Organization

1.1 Introduction

The ability to both qualify and quantify chemistry is crucial in the development of technology which impacts people's lives. Whether it deals with determining the dose of corticosteroids required for an asthma inhaler to detecting carbon monoxide leaks in buildings, society inherently relies on chemical sensors every day to ensure a high quality of life. Today, chemical sensor technologies are no longer limited to industrial settings as they were in the past. As chemical sensors are further miniaturized and easily manufactured at low cost, their applications, especially with personal devices and the Internet of Things (IoT), grow exponentially. In fact, in the next few years, the financial growth of chemical sensor technologies is expected to go up by 10.2% CAGR with an overall market of $31.2 billion [1]. This large growth yields great opportunities to research marketable solutions for the pressing needs of industrial, domestic, and academic customers.

1.2 Motivations and Focus of Research

A promising, low-cost technology analyzed in recent years is chemical detection via metal-oxide materials. Metal-oxide materials have enabled chemical sensors to be efficient in detecting both reducing and oxidizing gases (especially the former) depending on carrier type and concentrations of the sensing material. These devices find their niche especially in the detection of volatile organic compounds (VOCs). VOCs are common chemicals used in industry and domestic applications which, if not handled properly, can cause both acute and chronic health problems such as asphyxia, nausea, irritation, blindness, cancer, and death. In addition, the odor thresholds of certain VOCs tend to be small and, after the VOC concentration surpasses this threshold, the olfactory receptor neurons in the nose become saturated and are unable to detect higher, dangerous concentrations. This makes VOCs a much more potent threat.

This thesis focuses on methods of improving the sensitivity of metal-oxide materials to VOCs. To accomplish this, a thorough understanding of chemical interactions which cause chemicals to be “sensed” is first made along with information as to what makes a favorable metal-oxide for use in this chemical sensing technology. Then, device and testing parameters which have the greatest potential of sensitivity enhancement are determined and varied to understand optimal conditions for high sensitivity. A simple fabrication process, which develops prototype metal-oxide sensors that facilitate simple electrical testing, is made. Proper testing apparatuses and procedures that safely determine sensitivity readings to ethanol are also developed. In addition, a simulated metal-oxide chemical sensor, along with a simple fabrication process, is proposed for future work. Lastly, other facets of metal-oxide chemical sensing technology are also explored for future endeavors as well.

1.3 Organization of Thesis

Chapter 1 has talked about both the relevance of the research conducted in this thesis and a high-level overview of what will be discussed in this manuscript.

Chapter 2 gives a fundamental understanding of the systems engineering behind development of chemical sensor technology, the operating mechanisms of metal-oxide chemical sensors, reasoning behind choices of metal-oxide selection, and an overview of the device and testing parameters explored in this research.

Chapter 3 gives an in-depth description of the fabrication techniques utilized to make the prototype chemical sensors tested in this thesis, including thermal oxidation, sputtering, photolithography, and lift-off processing.

Chapter 4 describes the thin film characterization techniques used for materials analysis of the fabricated sensors, including determinations of sheet resistance, crystallinity, thickness, grain size, and surface morphology. Micrographs are also analyzed at different steps of the fabrication process for quality assurance.

Chapter 5 presents the electrical testing performed on the prototype devices for both short and long-term exposure to ethanol. Testing procedures and apparatuses are described in detail along with the electrical testing results as device and testing parameters are varied.

Chapter 6 discusses the design of a micrometer-scaled metal-oxide chemical sensor, including thermal and electrical simulations which further characterize it. A basic fabrication process that is compatible with the Rochester Institute of Technology’s clean room is developed.

Chapter 7 presents ideas, other than the chemical sensor developed in Chapter 6, for future research that can be done regarding metal-oxide chemical sensors regarding device materials, architectures, and electrical testing.

Chapter 8 gives an executive summary of the research conducted in this thesis, key takeaways from the data collected, and general outlooks regarding future endeavors of research related to this chemical sensor technology.

Chapter 2

Fundamentals of Chemical Sensors and Testing Parameters

2.1 Introduction

This chapter discusses operating principles and systems design of generic chemical sensor technology with specifics to metal-oxide chemical sensors. The physical and chemical mechanisms that provide device functionality for metal-oxide chemical sensors are discussed in detail. Parameters that were varied to investigate changes of sensitivity are also discussed, including the hypothesized effects on sensitivity they may have. Lastly, the chemical sensor design used to test these theories is shown, including material specifications and a basic layout.

2.2 Chemical Sensors

A chemical sensor, by definition, is a type of device that converts information relating to the material characteristics of a chemical into an analytically useful signal [2]. Sensors can range from small sizes in the form of personal breathalyzers to relatively large pieces of equipment such as a spectrophotometer to classify material properties of a specific chemical. The underlying principle behind each sensing technology, however, is similar in nature. Modern chemical sensors are operated to measure changes (i.e. electrical, optical, piezoelectric, etc.) in the sensing system, or the receptor, with respect to the introduction of a chemical, or analyte. At given operating conditions, the analyte will change a physical property of the receptor via chemical interactions; this change, in return, can be output as a change in an electrical characteristic of the receptor such as voltage, current, or resistance. This electrical change is monitored using outside circuitry and further analyzed and output digitally through a data processor. A basic process flow [3] diagram of a basic chemical sensor system is shown in Figure 2.1.

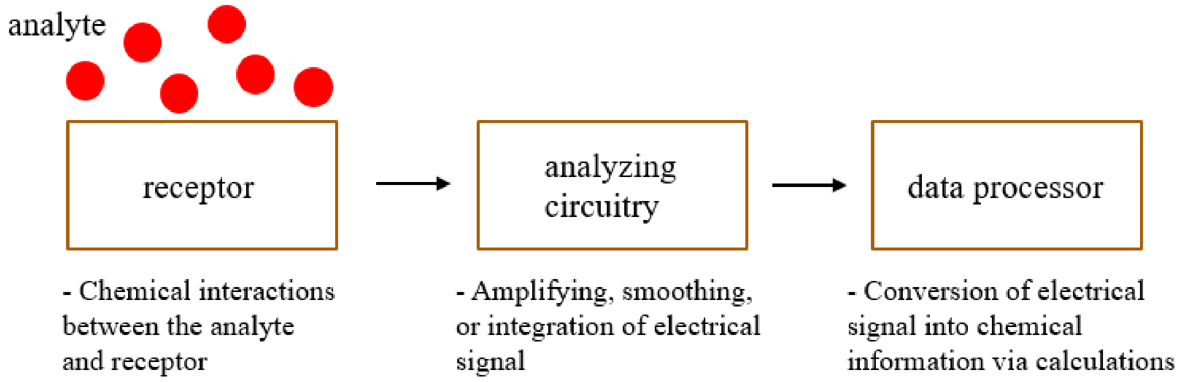

Figure 2.1. Basic chemical sensor system.

The type of chemical sensor used in a given application depends on the type of analyte and the environmental surroundings. For example, chemical sensors based solely on changes of electrical parameters are not suitable for use in military or space applications as both battlefields and space yield large amounts of electromagnetic interference. In those applications, other novel devices such as fiber-optic sensors can be used to ensure unperturbed analytical signals for accurate measurement of an analyte. Regardless of the sensing mechanism, more precise measurements generally require more expensive sensor instrumentation. Metal-oxide chemical sensors have been found to be reliable in detecting reducing gases although more research is needed to ensure optimal analyte selectivity. They offer a low-cost sensor alternative for applications in medical equipment, industrial and domestic ventilation control, fire detection, the Internet of Things (IoT), and a wide variety of other applications with detectable concentrations as low as 0.1 part per billion (ppb) [4].

2.3 Sensing Mechanisms of Metal-Oxide Chemical Sensors to Ethanol

N-type metal-oxide chemical sensors utilize oxygen-rich solid-state materials which change electrical characteristics based on chemical interactions of the analyte with adsorbed oxygen on the available surface area of the metal-oxide. A variety of materials, such as conductive transition metal-oxides (i.e. Fe_2O_3, Mn_2O_3) and conductive non-transition-metal oxides (i.e. SnO_2, ZnO), have been used for gas detection of either oxidizing or reducing gases [5]. These chemical interactions, which include adsorption, chemisorption, and desorption, require thermal energy for the analyte gas to successfully react with the sensing layer. These interactions are explained in further detail in the following subsections.

2.3.1 Adsorption

Adsorption refers to the physical binding of gas or liquid particles, the adsorbate, to a surface of a given material, the adsorbent. The first step in the sensing process requires the adsorption of oxygen to adsorption sites which exist on the metal-oxide surface; thus, this type of chemical sensor requires ambient air as it requires gaseous oxygen to function. At a high enough temperature (at least 250°C [6]), the oxygen molecules will adsorb to the metal-oxide surface and create a highly-resistive layer on the order of the Debye length, which can be theoretically calculated using Equation 2.1.

$$\lambda_D = \sqrt{\frac{\epsilon_0 k_B T}{q^2 N_C}} \tag{2.1}$$

ϵ_0 represents the permittivity of free space, k_B represents the Boltzmann constant, T represents the temperature, q is the charge of an electron, and N_c is the charge carrier density. The adsorption process can be modeled based on a derivation of the Langmuir isotherm model [3] shown in Equation 2.2.

$$\frac{d\theta}{dt} = k_{ads}\theta C - k_{des}(1 - \theta) \tag{2.2}$$

θ represents the fraction of available oxygen adsorption sites, C represents the concentration of adsorbate, and k_{ads} and k_{des} represent the rate constants of the adsorption and desorption reactions, respectively. This isotherm model serves as a basic adsorption/desorption characteristic model which makes the following assumptions:

1. Surface homogeneity (similar size and shape of adsorption sites)
2. Monolayer adsorption
3. Adsorption is reaction-rate limited (i.e. no further adsorbate will adsorb when each nucleation site is filled)
4. Each interaction between the adsorbate and nucleation site releases a constant amount of heat energy
5. The adsorption and desorption rates are independent of intermolecular interactions (i.e. heat of adsorption is the same in either high or low-populated adsorption areas)

The adsorption of oxygen and subsequent exchange of electrons is highly dependent on the temperature of the metal-oxide. Equation 2.3 reflects the adsorption sensitizing reaction [7] that takes place at an elevated temperature of roughly 300°C.

$$O_2 + 2e^- \rightarrow 2O^- \tag{2.3}$$

As shown, the adsorption reaction requires two electrons from the metal-oxide itself, which explains why the resistance subsequent to oxygen adsorption increases. Due to the exchange of electrons, this type of adsorption is known as chemisorption, which is indicative of chemical interactions between the adsorbate and adsorbent.

2.3.2 Chemical Reactions of Ethanol Oxidation

After the sensitizing adsorption reaction occurs and the adsorption sites are filled with oxygen, the analyte can be “sensed” by the metal layer through a chemical reaction with the adsorbed oxygen. The actual reactions and resulting products are dependent on the type of chemical analyte. In this thesis, the reactions of ethanol with adsorbed oxygen are predominantly studied. At high temperatures similar to the sensitizing adsorption reaction with oxygen, ethanol will react with the adsorbed oxygen in two different chemical reactions (Equations 2.4a, 2.4b, 2.5a, and 2.5b) dependent on the type of adsorption site (basic for Rxn. 1 and acidic for Rxn. 2) [8].

$$\text{Rxn. 1:}\quad \begin{cases} [O] + C_2H_5OH(g) \rightarrow CH_3CHO + H_2O & \text{(2.4a)} \\ 2CH_3CHO + 3O_2 \rightarrow 2CO_2 + 4H_2O & \text{(2.4b)} \end{cases}$$

$$\text{Rxn. 2:}\quad \begin{cases} [O] + C_2H_5OH(g) \rightarrow C_2H_4 + 4H_2O & \text{(2.5a)} \\ C_2H_4 + 3O_2 \rightarrow 2CO_2 + 2H_2O & \text{(2.5b)} \end{cases}$$

The first reaction, represented by Equations 2.4a and 2.4b, details the oxidative hydrogenation reaction that occurs on basic adsorption sites; the second reaction, represented by Equations 2.5a and 2.5b, details the dehydration reaction that occurs on acidic adsorption sites. The basicity and acidity of an adsorption site depends on the type of salt the metal-oxide forms; oxides with more metallic elements yield basic salts whereas oxides with non-metallic elements yield acidic salts. The first reaction is more prevalent and is preferred in the indium tin oxide (ITO) material system used in this thesis given the high percentage of basic ITO over acidic ITO in the mixture and the lower energy required to form acetaldehyde (Rxn. 1) compared to ethylene (Rxn. 2). As the two reactions occur, the electrons trapped by the adsorbed oxygen are reinjected into the conduction band of the metal-oxide (Figure 2.2) [6].

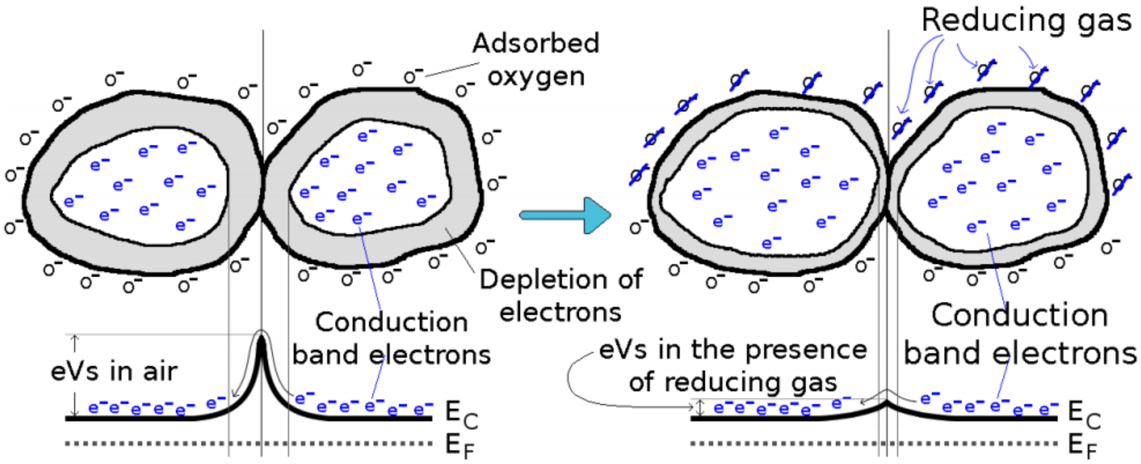

Figure 2.2. Reinjection of electron carriers into conduction band of metal-oxide.

As a result of the reinjection of carriers, the conductivity of the metal-oxide subsequently increases and can be output as an electrical signal. The high temperatures required for both reactions are normally obtained via pulsed voltage (on the scale of µs) of the heating element of the device to conserve power output much like the MEMS heating elements in inkjet print heads.

2.4 Basic Material Characteristics of ITO

As mentioned before, a wide variety of metal-oxide materials are used in gas sensor technologies with different electrical and mechanical properties. In this thesis, ITO (90% In_2O_3 to 10% SnO_2) was chosen as the metal-oxide sensing layer. Although ITO is normally used as transparent conductors in a variety of optoelectronics, there have been certain publications, such as in Vaishnav et al., which have proven its sensitivity to low molecular weight alcohols such as ethanol [8]. This allows for safer testing compared to other gases. Basic properties of ITO, including its electronic configuration, thermal stability, and crystalline structure are discussed below.

2.4.1 Electronic Properties of ITO

The predominant metallic constituent of ITO, indium, forms an “n-type”, electron-rich metal-oxide which allows localized oxidation of the metal-oxide’s surface at high temperatures for the sensitizing reaction described earlier. For reliable output signals, n-type sensing materials such as ITO are advantageous because of their reversibility to their steady-state position. N-type materials form a highly resistive surface after the sensitizing reaction and, after exposure to a reducing gas, will revert back to its highly resistive state in normal, atmospheric conditions. P-type materials, however, operate opposite to that of n-type materials; as they are exposed to the analyte, there is an increase of resistance as electrons from the adsorbed oxygen are injected back into the conduction band and further recombine with holes in the valence band. N-type materials, in most cases, make better sensing materials as increases in conductivity are more easily measurable with parameter analyzers and the electrical signal is found to be more producible in n-type materials compared to p-type ones [9]. Both the electronic configurations of indium and tin are also favorable in metal-oxide chemical sensing technology as they both have a filled d-orbital shell. Pre-transition (d^0), transition (d^n, $0 < n < 10$), and post-transition (d^{10}) metal-oxides are able to be used as metal-oxide sensing layers. However, pre-transition metal-oxides are less susceptible to oxidation compared to transition and post-transition metal-oxides due to their large band gap and inability to produce carriers easily for oxygen to adsorb with; it is imperative to ensure the sensitizing adsorption reaction of oxygen occurs so the reducing gas can interact with it. Some transition and post-transition metals can be used efficiently; however, post-transition metals are more favorable due to their stability of having a full d-orbital shell and having a preferred crystal structure. Transition metal-oxides will react with the oxygen due to their high catalytic activity with multiple oxidation states and this may significantly change the properties of the sensing layer, including band gap, structural integrity, and electron configuration. Post-transition metals with a filled d-orbital have the ability to chemisorb oxygen to its surface and reinject the carrier after the oxygen is reduced [9]. ITO also has a bandgap between 3.5 eV and 4.2 eV [10] which makes it suitable for operating at the required high temperatures for the adsorption and chemical reactions required for device functionality.

2.4.2 Thermal Stability of ITO

Thermal stability is important in a metal-oxide sensing material to ensure the material can both withstand high temperatures and maintain steady-state resistance values with changes of temperature. Compared to normal tin oxide films, ITO has been found to be much more thermally stable regarding resistance variation [8]. In addition, the thermal stability increases as the metal-oxide grain size increases as well; annealing the metal-oxide allows the metal-oxide to recrystallize and form these larger grains required for this stability enhancement [11]. This effect from annealing the metal-oxide material is investigated in device fabrication/testing and will be further discussed later in this chapter.

2.4.3 Crystalline Structure of ITO

Indium oxide, the main constituent of ITO, has two crystal structures: cubic bixbyite and rhombohedral. In the case with the deposition process used in this thesis, the indium oxide exhibits the cubic bixbyite structure; rhombohedral structures are formed at elevated substrate temperatures during sputtering. Cubic bixbyite is a base-centered cubic structure similar to the sesquioxide structure found in rare-earth metal-oxides. A unit cell for indium oxide ($In_{32}O_{48}$, consisting of 16 In_2O_3 units), where black molecules represent indium atoms and empty spheres represent oxygen atoms, is shown in Figure 2.3 [12].

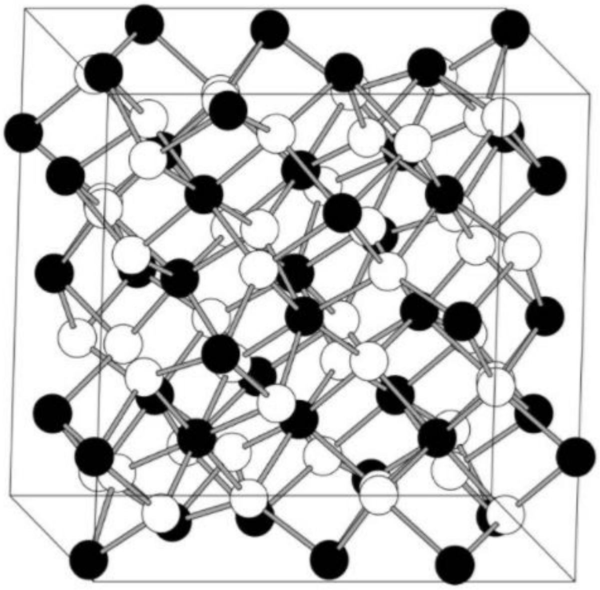

Figure 2.3. Cubic bixbyite crystal structure of indium oxide.

The lattice constant, a, of indium oxide in particular is roughly 10.1 Å as taken from literature [13]. Although the addition of tin oxide will subtly change the lattice constant, the average lattice constant of ITO can be assumed to be that of indium oxide for rough calculations. A publication has found the lattice constant of ITO to increase steadily upon the addition of tin oxide until the tin oxide content reached 10% by weight, where the value of the lattice constant plateaued to roughly 10.125 Å [14]. Even without annealing the metal-oxide material, sesquioxides tend to have favorable catalytic characteristics such as high adsorption capacity due to the high specific surface area of the cubic bixbyite structure [15]. This ensures ample amounts of oxygen adsorption sites for the sensitizing reaction and mitigates reaction-rate limitations from potential analyte oversaturation.

2.5 Variable Parameters Used in Fabrication/Testing

Certain device and testing parameters were varied to understand the parameters' effects on device performance. To minimize the number of wafer splits in this thesis, two parameters (metal-oxide thickness and crystallinity) were varied in the device fabrication and two parameters (device operating temperature and VOC concentration) were varied in electrical testing. Each parameter's values are summarized in Table 2.1 and further discussed in the following subsections. Given the two thicknesses, two crystalline phases, three operating temperatures, and four VOC concentrations, a design of experiments was created with these parameters to ensure all 48 combinations were tested.

Table 2.1. Testing parameters and their associated values.

Parameter	Annealed ITO
Thickness	100 nm, 400 nm
Crystallinity	Amorphous (as-deposited), Polycrystalline (annealed)
Device Operating Temperature	160°C, 260°C, 360°C
VOC concentration	500 ppm, 1000 ppm, 1500 ppm, 2000 ppm

2.5.1 Effects of Metal-Oxide Thickness on Sensitivity

As said before, oxygen will adsorb to the metal-oxide surface but only on the order of the Debye length into the material. Because the output electrical signal relies on the change of resistance facilitated by the highly-resistive metal-oxide surface, it is crucial to ensure the actual metal-oxide layer is also on the scale of the Debye length. Thinner films will ensure the current flowing through the metal-oxide is forced through the resistive zone [16]. A basic diagram (not to scale) illustrating the effects of thin and thick films on current flow is shown in Figure 2.4.

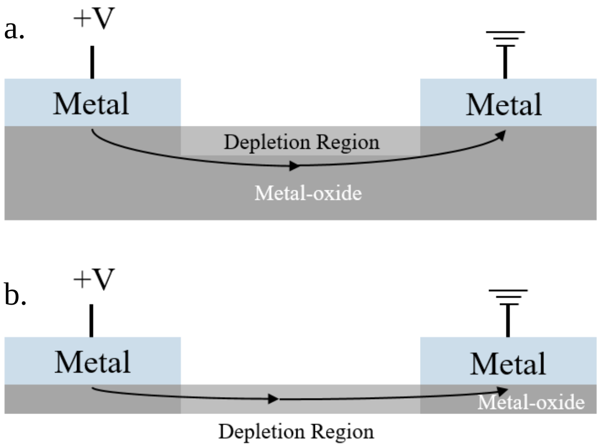

Figure 2.4. Thick (a) / thin (b) metal-oxide film current flow with surface depletion.

Rough calculations of a Debye length, using electrical/material properties obtained from a similar ITO deposition process to what was used in this thesis [10], yields an average Debye length of 3 nm. With this being said, films on the scale of nanometers are desired to ensure optimal changes of resistance. However, thinner metal-oxide films come at the cost of decreased uniformity and consistency. Ultra-thin metal-oxide films of ITO have been shown to have undesired hollows and pitting at thicknesses in the range of 5 to 20 nm [17] which may cause shorting of the metal-oxide path in some cases. The metal-oxide thicknesses tested in this thesis (100 nm and 400 nm) are large relative to the theoretical Debye length, but they were used to ensure film uniformity.

2.5.2 Effects of Metal-Oxide Crystallinity on Sensitivity

Increasing the metal-oxide surface area increases the number of potential oxygen adsorption sites. Surface area is increased in this thesis by annealing the metal-oxide in an inert ambient. As-deposited metal-oxide tends to have smaller conglomerations of packed grains which limit adsorption of oxygen to the top surface of the layer. However, annealing a metal-oxide tends to increase the grain size and crystallize the film [18] to increase the surface area and conductivity of the film. The metal-oxide layer becomes porous as the grain size increases, which allows oxygen adsorption and subsequent chemical reaction within the layer rather than just at the geometric surface. A basic diagram of mass transport of the gas in compact and porous layers is shown in Figure 2.5 [3].

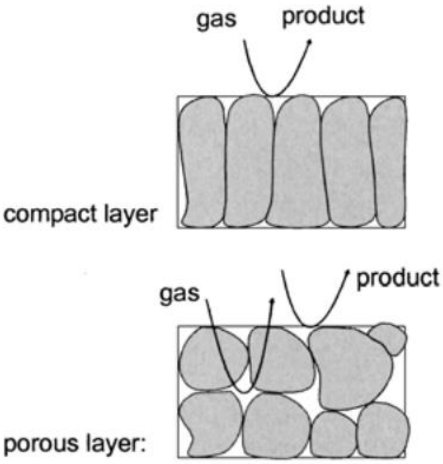

Figure 2.5. Mass transport of gas in compact and porous grain layers.

Surface area enhancement ensures quicker response times with changes of analyte concentration as demonstrated by the Langmuir isotherm model discussed. The change in open adsorption sites with respect to analyte concentration is much greater for materials with higher surface areas compared to materials with low surface areas. This is due to the increase of the adsorption and desorption rate constants which are partially related to the number of adsorption sites. A basic graph demonstrating changes of the fraction of adsorption sites with respect to oxygen with a decrease in concentration for low and high surface area materials is given in Figure 2.6. This graph is relatable to initial electrical testing of the chemical sensors in Chapter 4 in which $\theta(1)$ assumes complete reaction of the analyte with the adsorbed oxygen and $\theta(0)$ represents the material's steady state in which all adsorption sites are filled with oxygen.

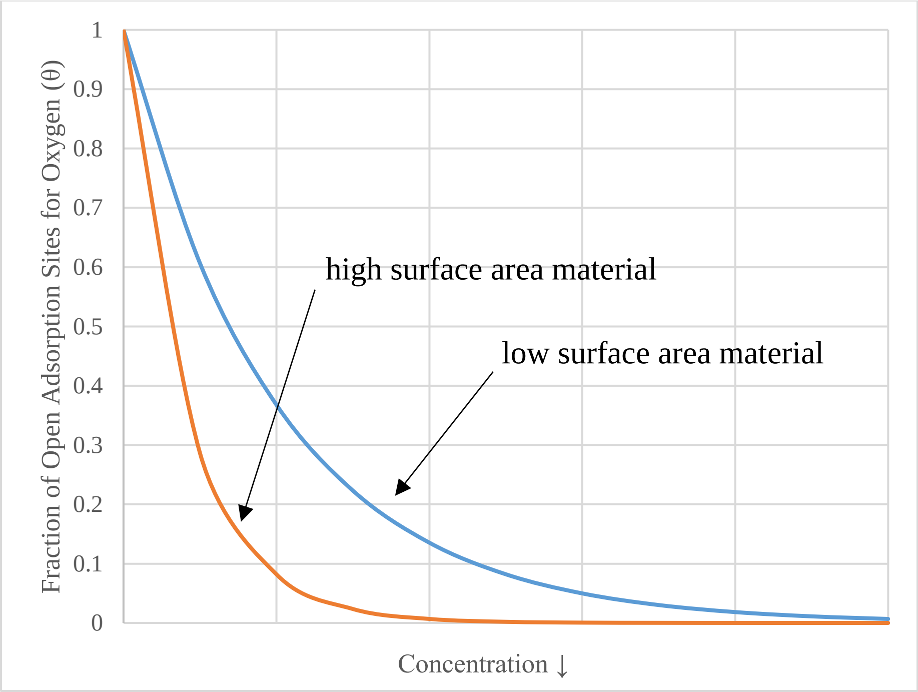

Figure 2.6. Change of adsorption sites with respect to change of concentration.

In addition to the increase of surface area, the increase of conductivity allows the resistance of the metal-oxide to reach lower values to the point where a measurable electrical signal can be output efficiently. Annealing the metal-oxide layer, as shown in Chapter 4, improved the sheet resistance uniformity across the wafer. This ensures a robust fabrication process with predictable device performance with all devices across the wafer.

2.5.3 Effects of Rate Kinetics on Sensitivity

Higher temperatures generate lattice vibration in metals which creates carrier scattering in the metal-oxide. This, in turn, causes the conductivity to decrease. However, this type of chemical sensor depends on the oxygen/adsorbent and analyte/oxygen interactions for output of electrical signals. Temperature plays a significant role in both the sensitizing reaction and the analyte reaction. Because both are chemical interactions, each requires a certain amount of energy to react which is usually facilitated in the form of heat energy. Although the metal-oxide resistance increases, both the sensitizing and analyte rates of reaction are increased at high temperatures. The basic reaction can be modeled in a classic rate law shown in Equation 2.6.

$$r = k(T)[A]^x[O(ad.)]^y \tag{2.6}$$

r represents the rate of reaction, [A] represents the concentration of the analyte, [O(ad.] represents the concentration of adsorbed oxygen, k(T) represents the rate constant which is dependent on temperature, and x and y represent stoichiometric coefficients in the balanced reaction depending on the analyte. As temperature increases, the rate constant will also increase which ultimately increases the rate of reaction. This allows for both more adsorbed oxygen and further analyte reaction which, in turn, increases the conductivity more as more electrons are reinjected back into the metal-oxide. In addition to temperature, Equation 2.6 shows that increasing the analyte concentration will also increase the rate of reaction. Both temperature and analyte concentration play important roles in sensitivity of metal-oxide chemical sensors. Although all the aforementioned device and testing parameters will inherently change the resistance value, it is important to study the percent change of resistance from steady-state resistance values of the specific sensor rather than the actual change of resistance.

2.6 Investigated Device Structures

Due to the complexity and time associated with fabricating and characterizing complex devices, a simpler, proof-of-concept chemical sensor was fabricated in this thesis which utilized an external heater placed underneath the substrate material. In most devices incorporated in microsystems, however, a built-in MEMS heater is normally integrated underneath the metal-oxide layer to raise the temperature of the sensing layer to the point where chemical interactions may occur. Both chemical sensor structures – a basic device structure and the device structure used in this thesis – are discussed further in the following subsections. The design parameters and reasoning behind their incorporation are described for the proof-of-concept sensor.

2.6.1 Basic Metal-Oxide Chemical Sensor Structure

The device structure for a common metal-oxide chemical sensor consists of a base material which acts as a thermal and electrical insulator for the device. A relatively thermally-conductive layer (i.e. silicon nitride) is placed in between the metal-oxide and a MEMS heater which allows the device to heat up to the required temperatures for chemical reactivity. An example of a basic device structure (not to scale) is shown in Figure 2.7.

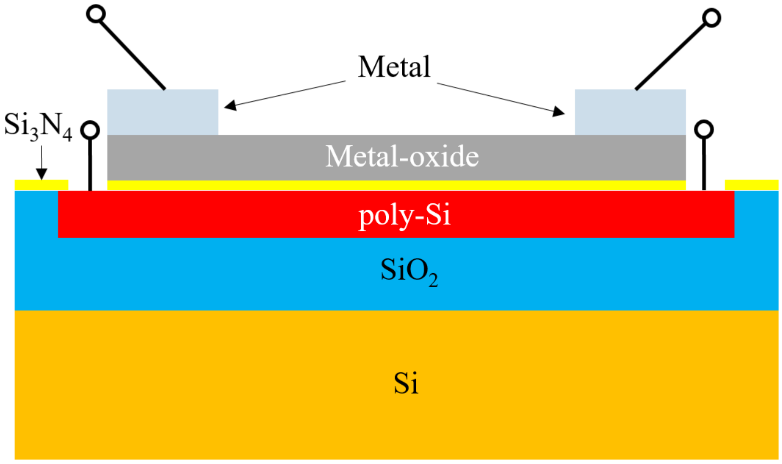

Figure 2.7. Basic structure of metal-oxide chemical sensor.

The substrate used to build devices such as these is usually silicon oxide on silicon as silicon is relatively cheap and is able to withstand high-temperature processes easily. An arbitrary amount of silicon oxide is grown to ensure any doping which may be in the silicon does not affect electrical measurements taken from the metal-oxide. In addition, the resistance of the polysilicon heater underneath the silicon nitride can be tuned using doping techniques such as ion implantation to vary the voltage and resulting power required to heat it to certain temperatures. A characteristic device which utilizes this structure is discussed further in Chapter 6, along with thermal and electrical simulations of the device. Because the device dissipates a large amount of heat, the heater normally has to be run at a higher temperature to account for heat conduction to the substrate and convective heat loss to the surrounding air. Furthermore, to ensure heat is not dissipated into nearby integrated electronics in a microsystem, the device itself may be suspended in air by etching underneath the device. Through-silicon vias (TSVs) may also be added to ensure quicker response times due to the long metal connections used to connect the sensor electrodes to the integrated circuitry. Figure 2.8 represents the integration of both a suspended device and TSVs in a chemical sensor microsystem [6].

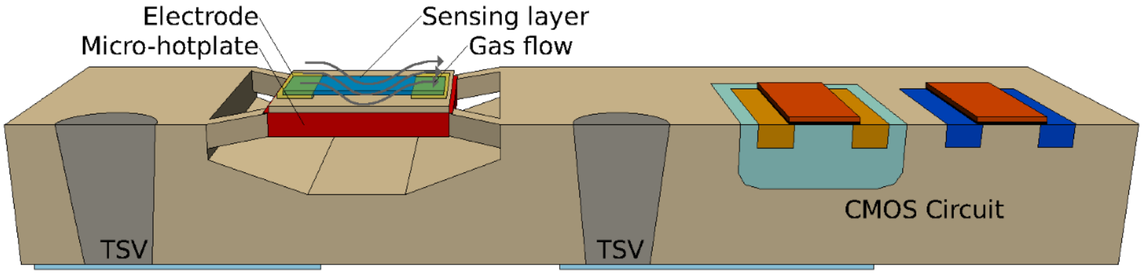

Figure 2.8. Suspended device and TSV integration in chemical sensor microsystem.

2.6.2 Proof-Of-Concept Metal-Oxide Chemical Sensor Structure

The proof-of-concept sensor structure utilizes the same principle of the basic structure, but there is not a built-in MEMS heater; instead, the physical sensor was placed on an external metal-ceramic heater (for chemical chamber testing) to heat it to the required temperature. The 2-D structure, along with the actual proof-of-concept sensor dimensions, are both shown in Figure 2.9.

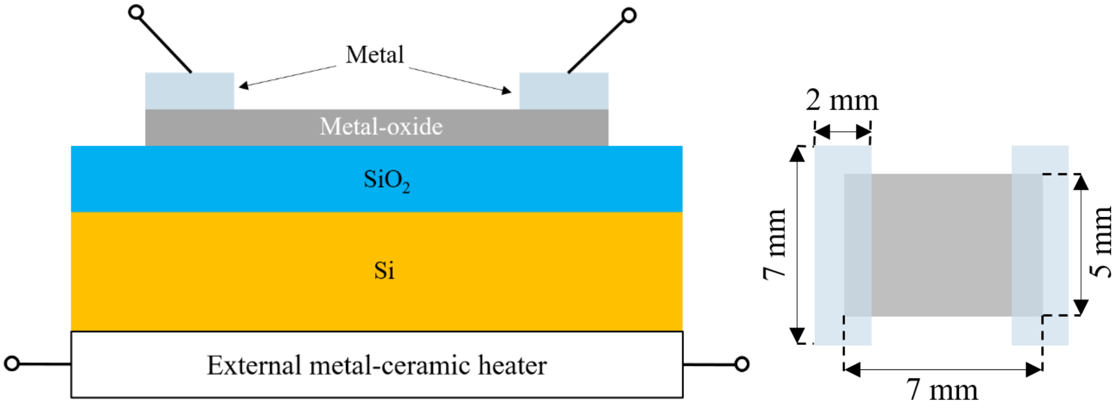

Figure 2.9. Proof-of-concept device structure and top-layer dimensions.

The dimensions of this proof-of-concept structure were also made larger to ensure easier testability with larger metal contacts to probe to in the chemical chamber tests. The larger sensing area also ensured more obvious changes of resistance of the sensor that could be easily measured with the semiconductor parameter analyzer used in testing. The fabrication processing was also much easier given the device dimensions; due to difficulties with the photolithography steppers in the clean room throughout the duration of this project, the large dimensions allowed the use of the contact printer with masks easily made using cellulose acetate transparency paper.

2.7 Conclusion

The basic process flow of chemical sensor functionality was described. The two-step sensing process of metal-oxide chemical sensors, which consists of an adsorption sensitizing reaction and subsequent chemical reaction of the analyte, was discussed. The electronic, thermal, and structural properties of the material used as the metal-oxide in this thesis, ITO, were discussed. The device and testing parameters tested in this thesis, and their proposed effects on device sensitivity, were discussed in detail. Lastly, the device structures of a basic metal-oxide chemical sensor and the proof-of-concept sensor were discussed, including details regarding why the latter structure was fabricated and tested in this thesis.

Chapter 3

Fabrication Process of Chemical Sensors

3.1 Introduction

This chapter describes each processing step used to fabricate the proof-of-concept chemical sensors tested in this thesis. The basic process flow is discussed. The fabrication processes were done in the Semiconductor & Microsystems Fabrication Laboratory (SMFL) at the Rochester Institute of Technology's Kate Gleason College of Engineering.

3.2 Basic Fabrication Sequence

This section summarizes a high-level process sequence (Figure 3.1) which will be explained in further detail in future sections of Chapter 3.

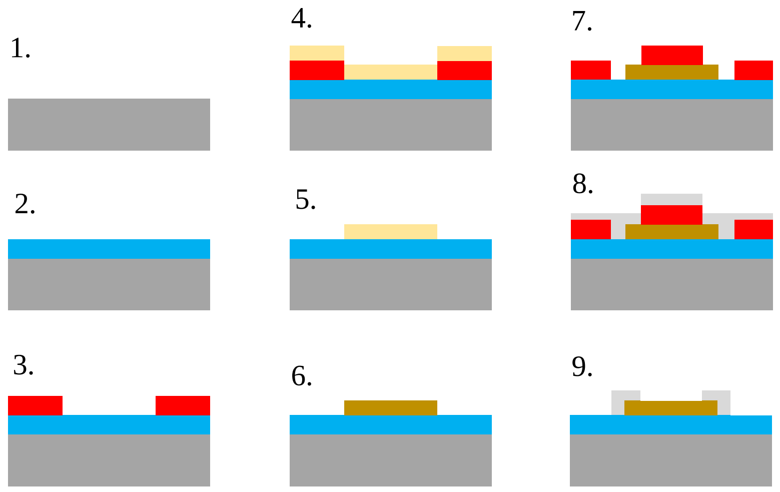

1. RCA clean of substrate surface
2. 6500 Å wet oxide growth
3. Preparation of lift-off process for ITO
4. ITO deposition (target 1000 Å, 4000 Å splits)
5. Lift-off process of ITO-covered photoresist
6. Annealing of ITO (optional)
7. Preparation of lift-off process for Al
8. Al deposition (target 3000 Å)
9. Lift-off process of Al-covered photoresist

Figure 3.1. Basic fabrication process flow with cross-sections at each step.

3.3 RCA Substrate Cleaning

The chemical sensors were fabricated using silicon wafers as the base substrate material. The wafers used were p-type, boron-doped, (100) crystal orientation, and had a sheet resistance between 5-15 Ω/sq. confirmed via four-point probe measurement. To remove any native oxides or impurities from the surface of the silicon, an RCA clean was performed on the device wafers before thermal oxidation. The RCA clean consists of four subprocesses: a Standard Clean 1 (SC-1), an additional oxide strip, a Standard Clean 2 (SC-2) and a spin-dry-rinse (SRD) of the wafer [19].

3.3.1 Standard Clean 1 (SC-1)

The wafers were first put in an ammonium peroxide mixture (APM) for ten minutes. This mixture removes any organic compounds or particles on the surface of the wafer. The mixture was made under a fume hood with 4500 mL of water, 300 mL of 30 mol% ammonium hydroxide and 900 mL of hydrogen peroxide. The wafers were submerged in the mixture in a Teflon wafer boat for 10 minutes at 75°C and subsequently rinsed in deionized water for 5 minutes.

3.3.2 HF Oxide Strip

An additional step to the standard RCA clean is removal of both the oxide formed from SC-1 and a small amount of ionic contaminants on the substrate surface. This is accomplished through chemical treatment of the wafers using a 6-L solution of 50:1 water to 49 mol% hydrofluoric acid (HF) made in a fume hood. After SC-1, the device wafers were put in a Teflon wafer boat and submerged in the mixture for 1 minute and subsequently rinsed in deionized water for 5 minutes.

3.3.3 Standard Clean 2 (SC-2)

SC-2 consists of a hydrochloric acid (HCl) and peroxide mixture (HPM) used to remove the rest of the ionic impurities on the wafer surface. This process also grows a thin passivating layer of oxide to prevent inevitable contamination of the silicon surface after removal from the mixture. The mixture was made under a fume hood with 4500 mL of water, 300 mL of 37 mol% HCl and 900 mL of hydrogen peroxide. After the HF oxide strip, the wafers were submerged in the mixture in a Teflon wafer boat for 10 minutes at 75°C and subsequently rinsed in deionized water for 5 minutes.

3.3.4 Spin-Rinse-Dry (SRD)

Lastly, to ensure the substrate surface was not in contact with impurities after the wafer was removed from the mixture, the Teflon wafer boat was placed in an SRD machine for 5 minutes where it was cascade-water rinsed and subsequently dried.

3.4 Thermal Oxidation of Silicon Substrate

A wet-oxide growth process was performed in Bruce Furnace Tube #1 using Recipe 406 in the RIT furnace recipe database. The target thickness of this wet-oxide growth process was 6500 Å. The wafers are put into a quartz boat and loaded into the furnace. The recipe, including the temperature, duration, gas flow rates, and brief description of each interval, is summarized in Table 3.1.

The wafers were slowly pulled out of the furnace after wet oxidation to prevent thermal shock of the oxide layer grown on the silicon; substrate cracking may result if the wafers are pulled too quickly out of the furnace into room temperature conditions.

Table 3.1. Bruce Furnace Tube #1; Recipe 406 – Wet Oxide Growth (6500 Å).

Interval	Description	Temperature	Time at Step	N_2 flow rate (lpm)	O_2 flow rate (lpm)	H_2 flow rate (lpm)
0	Boat Out / Load	25°C	N/A	N/A	N/A	N/A
1	Boat In / Push	800°C	12 min	10	0	0
2	Stabilization	800°C	15 min	10	0	0
3	Ramp-up	800°C to 1100°C	30 min	5	0	0
4	Soak	1100°C	5 min	0	5	0
5	Soak	1100°C	65 min	0	10	10
6	Anneal	1100°C	5 min	15	0	0
7	Ramp-down	1100°C to 800°C	55 min	10	0	0
8	Boat Out / Pull	800°C	15 min	15	0	0

3.5 Lift-off Processing of Metal-Oxide and Metal Contacts

The basic lift-off process used in this study consists of three main steps: preparation of the lift-off photoresist, a sputtering process of the sensitive metal-oxide layer or metal contact layer and the lifting off of the material-covered photoresist. The lift-off photoresist acts a hard mask for deposition processes and can be used to make features with thicknesses less than 500 nm. For both the metal-oxide and aluminum deposition processes, the preparation and removal of the photoresist are the same.

3.5.1 *Preparation of Lift-off Photoresist*

Photoresist processing was done using the Semiconductor Systems, Inc. (SSI) 150 Wafer Track. The system consists of two separate wafer tracks; Track 1 is used for photoresist coating and Track 2 is used for photoresist development. The device wafers were loaded into a wafer boat on Track 1. The recipes “COATNLOF” and “DEVNLOF” were used for Track 1 and Track 2, respectively, and are both summarized, along with the flood UV exposure step, below.

The coating process first starts with a priming step which allows better adhesion of the photoresist to the wafer surface; hexamethyldisilazane (HMDS) was used as the primer in this process. The wafer was heated to 140°C and HMDS was dispensed for 30 seconds; the wafer was then primed for 60 seconds. The wafer was then put onto a spin-coater where the lift-off photoresist was manually dispensed onto the wafer surface using a filled, 7-mL pipette. AZ n-LOF-2020 Image Reversal Resist, a negative photoactive lift-off photoresist, was used in both lift-off processes. After puddle dispensing the photoresist, the spin coater was ran at 2500 RPM for 60 seconds to ensure an average photoresist thickness of roughly 2500 nm. Afterwards, a soft post-coat bake (PCB) was performed at 110°C for 60 seconds to both solidify the photoresist and evaporate any remaining solvents after the spin-coat. The wafers are then automatically loaded into the wafer boat on the end of the track.

A flood UV exposure was done on the Karl Suss 150 Contact Printer with clear-field masks to expose the photoresist. Figure 3.2 shows the layout of the sensing metal-oxide and metal contact layers, respectively. Each clear-field mask has an alignment marking at the center to ensure alignment to each layer. Due to the large feature sizes of the devices, the masks were easily designed to scale in Adobe Photoshop CC and printed out on cellulose acetate transparency paper using an industrial laser printer with solid black toner.

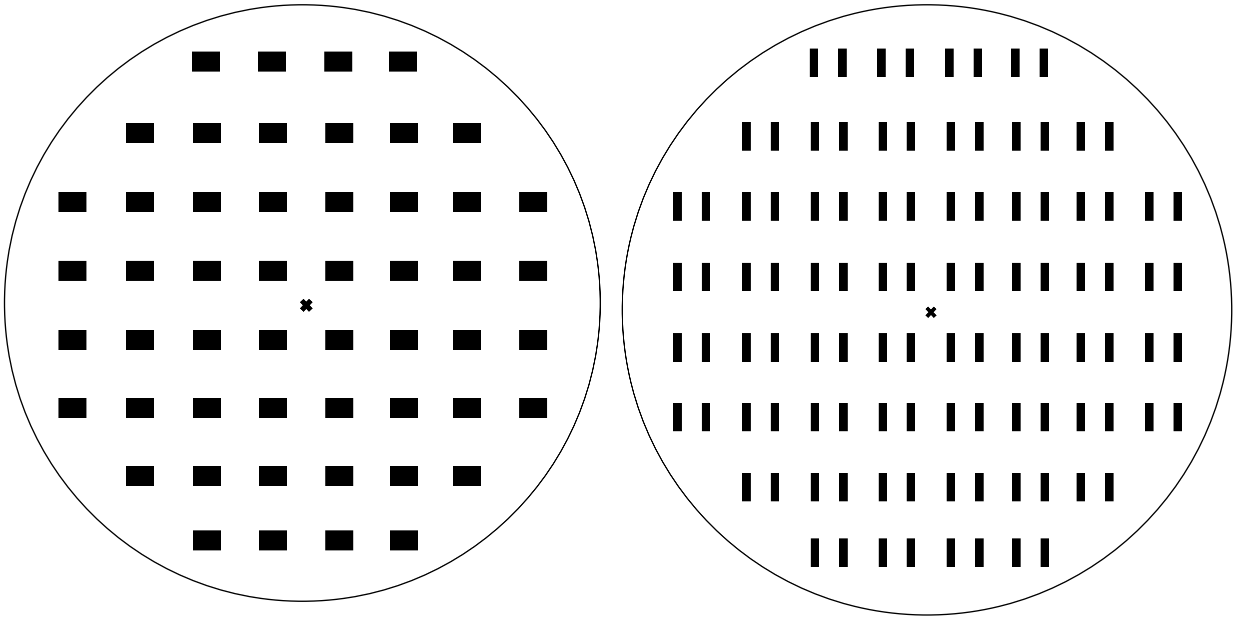

Figure 3.2. First-layer metal-oxide sensing area (left) and second-layer metal contacts (right) clear-field masks.

The width of the metal-oxide sensing area feature on the mask was aligned to be parallel to the flat of the wafer for first-level lithography. The transparency was carefully placed on the photoresist-covered wafer ensuring the laser-printed side was facing upwards; this mitigates any contamination that may result from contact between the black toner and photoresist. Small amounts of dust that were collected on both sides of the transparency from normal storage were cleaned off using a compressed air gun; both inorganic and organic solvents cannot be used to clean the mask as they may dissolve the black toner and/or the transparency itself.

The time of exposure was calculated by dividing the required dose of exposure of the photoresist from its technical data sheet [20] (65 mJ/cm^2) by the average intensity of the contact printer (~19 mW/cm^2); this gives an exposure time of roughly 3.4 seconds. Overexposure of the photoresist is preferable over underexposure as underexposure will cause incomplete chemical reaction in the clear-field areas of the photoresist; this will undesirably remove areas of the clear-field area in a strong base developer. The sidewalls of the photoresist may be tapered from potential overexposure, but the change of feature sizes (on the scale of micrometers) will not be enough to cause catastrophic device failure given the allotted amount of overlay (on the scale of millimeters) in the mask design.

After UV exposure, the wafers were placed back into a wafer boat and loaded on to SSI Track 2. A post-exposure bake (PEB) was done at 110°C for 60 seconds to promote crosslinking in the exposed photoresist material and effectively allow exposed portions to become base insoluble. The wafer was then placed on a spin-coater where the wafer was slowly spun and the photoresist developer, 0.05 N tetramethylammonium hydroxide (TMAH) CD-26 Developer, was dispensed onto the wafer surface for 5 seconds; the spin-coater was stopped and, for an additional 5 seconds, more developer solution was dispensed. The developer solution was left on the photoresist to puddle develop for 70 seconds. The spin-coater was then turned on and spun for 30 seconds at 1000 RPM to ensure full coverage of the wafer with the developer. To dry the wafers, the spin-coater was run at 3750 RPM for 30 seconds. The wafers were then loaded back onto the wafer boat on the opposite side of the track. A hard bake was not done for this photoresist as it may damage its sidewall profile and structural integrity.

3.5.2 Sputtering of Metal-Oxide and Metal Contact Layers

Thin film deposition was performed using the CVC 601 DC Sputtering System. Sputtering is a physical vapor deposition (PVD) process in which inert, high-energy gas ions in the process chamber ambient (usually argon) bombard a sputtering target and the target material is ejected and deposited onto the substrate surface. This specific sputtering system sputters the material upwards with the substrates located above the target. The mean-free-path length (usually denoted as λ) of the process chamber must be large enough for the sputtered material to travel from the target to the substrate, so a very-high vacuum (~10^{-6} – 10^{-10} torr) is recommended for optimal sputtering conditions.

The tool itself has a continuously-rotating platen with 6”-diameter substrate holders where the wafers are placed face-down; rotating the wafers during a sputtering process improves thickness uniformity. However, due to slight misalignments that occur in the installation of each sputtering target, there is always a characteristic “parabolic” shape that results from any sputtering process done in the tool as shown in Figure 3.3 resulting in higher sputtered thicknesses on opposite sides of the wafer [21]. This non-uniformity can be mitigated via metal shielding plates of the back sides of the substrate holders.

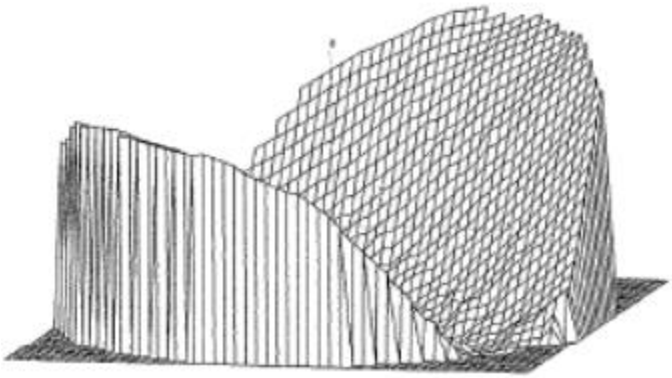

Figure 3.3. Uniformity profile of sputtering process in CVC 601 DC Sputter Tool.

To maintain consistency with measurements for each device wafer, each of the wafers were aligned arbitrarily with the flat facing the left in the substrate holder closest to the operator as demonstrated in Figure 3.4. The rest of the substrate holders in the platen were filled with dummy wafers.

Figure 3.4. Alignment of wafer flat to the left in sputtering chamber platen.

The sputtering tool has a dual-vacuum pump system consisting of a mechanical roughing pump and a high-vacuum cryopump to allow the process chamber to reach an acceptable vacuum pressure. After the wafers were loaded into the substrate holders of the platen, the process chamber lid was shut and the vacuum system was initiated. The roughing pump brought the chamber pressure down to a set point of roughly 40 mTorr in 15 minutes and the cryopump continued the pump-down process to roughly 10^{-6} to 10^{-7} torr in 16 to 18 hours.

Both sputtering process parameters of the metal-oxide (ITO) and the aluminum contacts are summarized in Table 3.2. Pulsed DC sputtering with a low sputtering power was used over traditional sputtering methods for ITO to greatly reduce arcing and particle generation so purer metal-oxide films could be fabricated [22]. Higher purity ITO films allow for a greater amount of adsorption sites for VOC detection; however, due to the low sputtering power and the fact that it is a pulsed DC sputter, the deposition rate is significantly smaller compared to traditional DC sputtering processes.

Table 3.2. Process parameters for metal sputtering processes.

	ITO Sputtering Process	**Al/Si Sputtering Process**
Base pressure (torr)	10^{-6} - 10^{-7}	10^{-6} - 10^{-7}
Process pressure (torr)	5×10^{-3}	5×10^{-3}
Argon flow rate (sccm)	40	28
Sputtering power (W)	180	2000
Type of sputter process	Pulsed DC sputter Pulse width = 1600 ns Pulse frequency = 250 kHz	Standard DC sputter
Deposition rate (nm/min)	4	30
Target description	6” inch diameter 90% indium oxide 10% tin oxide Purity: 99.9999%	6” inch diameter 99% aluminum 1% silicon Purity: 99.9999%

Before any sputtering processes are done to the actual wafers, the targets are conditioned via pre-sputtering. This ensures that any impurities from the target surface are cleaned off and that the number of arcs generated from sputtering runs are mitigated [21]. Using the same parameters outlined in Table 3.2 for each sputtering process, the target shutter is placed over the respective target to block the substrate and the sputtering processes in both cases are run for 5 minutes.

3.5.3 Photoresist Lift-off via Ultrasonic Wet Bench

The lift-off photoresist was removed using an ultrasonic wet bench and an organic solvent which dissolves the photoresist and lifts off the metal layer on top. The wet bench is equipped with a large tank of water and a wire frame suspension. A square, glass container filled with roughly 100 mL of Nano™ Remover PG Solvent Stripper was prepared in a fume hood; the individual wafer was then submerged carefully into the glass container ensuring the surface of the wafer was completely covered by the solvent. The glass container was then set into the wire frame and the water in the tank was filled up enough to completely touch the bottom of the glass container. When the power is turned on in the tank, ultrasonic vibrations are induced in the water and transferred to the glass and, ultimately, the wafer; the vibrations are strong enough to initiate immediate removal of the photoresist material. If certain areas of the lift-off photoresist could not lift-off initially, a light scrape in the metal/photoresist layer outside of the device region was made using a wafer tweezer's edge to generate initial points of contact between the solvent and the photoresist.

Because the solvent itself became filled quickly with the lifted-off metal, the metal-filled solvent solution was, at times, taken and filtered through a Chemwipe into a glass beaker to remove a majority of the lifted-off metal. This mitigated redepositing of the metal back on the wafer surface and allowed for solvent reuse for other wafers. The wafers were then put into a separate glass container in a fume hood where acetone was sprayed onto the surface to remove minute amounts of metal that may have settled on the wafer surface. The average time taken for removal of the metal/photoresist layer was roughly 30 minutes for each wafer for both deposited metals. The wafers were then dried using a compressed-air gun ensuring all organic solvents were removed.

3.6 Metal-Oxide Annealing Process

To study the effects of crystalline structure on device performance, some control and device wafers were annealed using a high-temperature, inert ambient in Bruce Furnace Tube #8 before metal contact lift-off processing. The wafers were loaded into a quartz boat for processing. The annealing process is summarized in Table 3.3.

Table 3.3. Bruce Furnace Tube #1; Recipe 835 – 1 hour, 450°C Anneal in Nitrogen.

Interval	Description	Temperature	Time at Step	N_2 flow rate (lpm)
0	Idle	300°C	N/A	N/A
1	Load	300°C	N/A	5
2	Ramp-up	300°C to 450°C	15 min	10
3	Anneal	450°C	60 min	0
4	Pull Out	450°C	15 min	0

The furnace tube was also heated up to 300°C prior to the annealing process to cut down on residency time of the wafers in the furnace tube. Similarly to the aforementioned oxidation process, the wafers are slowly pulled out to prevent thermal shock to the substrate.

3.7 Wafer Cleaving

After each wafer is fabricated, they are each cleaved using a diamond scribe. The scribe was scratched on the edge of the wafer and manually broken; due to the crystal structure of the silicon wafers, the wafer is cleaved in a straight line through the wafer from the point of where the wafer was scratched. Each of the devices were stored in a small plastic container to be stored for electrical testing.

3.8 Conclusion

The process flow of the proof-of-concept chemical sensor fabrication, including both cross-sectional diagrams of the devices at each step and in-depth explanations regarding each process step, is presented. The processes mentioned in this chapter are crucial elements of fabrication and include detailed information of the RCA cleaning process, oxide growth process, lift-off photoresist preparation, sputtering processes for both metal depositions, lift-off photoresist dissolution using an organic solvent, wafer cleaving and the additional high-temperature annealing process utilized for some splits before the metal contact layer is fabricated. The parameters used in each process are also summarized.

Chapter 4

Qualitative and Quantitative Characterization of Chemical Sensors

4.1 Introduction

This chapter describes characterization methods utilized to verify qualitative and quantitative metrics established for the proof-of-concept chemical sensors. Each method used, including thickness measurements, sheet resistance characterization, and microscopic inspection, is discussed in detail. The measurements were done in both the SMFL and the Advanced Materials Laboratory at the Rochester Institute of Technology's Kate Gleason College of Engineering.

4.2 Thickness Measurements

Two thickness measuring tools were used to measure oxide, metal-oxide, and metal contact thicknesses for deposition rate confirmation. The Prometrix SM300 SpectraMap was used to measure global thickness whereas the Tencor P2 Profilometer was used to measure localized feature thicknesses of the metal-oxide regions and metal contacts.

4.2.1 Prometrix SM300 SpectraMap Measurements

The oxide thicknesses on both the control and device wafers, along with the metal-oxide thicknesses on the control wafers, were measured using global measurements from the Prometrix SM300 SpectraMap. The SpectraMap uses average indices of refraction of the materials being measured to calculate the thickness of the top film in a thin film stack. Films below the desired film to be measured must be explicitly defined in the machine to ensure selective measurement of the top film [23]. After the wet oxidation process of both the control and device wafers, a control wafer is taken for oxide thickness measurements. A rough estimate of the metal-oxide thickness was also determined using the same control wafer after an ITO sputtering process with a target thickness of 1000 Å; a custom thickness measurement for ITO, with an average index of refraction of 2.33 obtained from terahertz spectroscopy of the ITO sample, was used. The statistics of both measurements are summarized in Table 4.1. The measured oxide was roughly 300 Å more than the target oxide thickness in the process, but the oxide layer was found to be conformal with low standard deviation. The ITO film was found to be very close to the target thickness of 1000 Å with a slightly higher standard deviation.

Table 4.1. Statistics of oxide and ITO measurements for single control wafer.

t (Å)	**SiO_2**	**ITO**
Average	6826.6	986.2
Standard Deviation	16.1	24.3
Standard Deviation (%)	0.236%	2.5%
Minimum	6794.4	960.3
Maximum	6862.5	1012.2
Range	68.1	51.9

4.2.2 Tencor P2 Profilometer Measurements

A profilometer utilizes a small stylus which is moved across the edge of a film to obtain a change of vertical height which is defined as the film thickness. To reduce the amount of noise on the measurement, a longer distance scan of 100 µm was done on each film measurement to obtain a more pronounced change between the film and the baseline oxide layer. Localized thickness measurements of the metal-oxide sensing layer and metal contacts were taken at five distinct locations, which are labeled in Figure 4.1, on wafers with different sputter target thicknesses of 1000 Å and 4000 Å. The thicknesses of the features at each location on the wafer for both wafers of differing ITO thickness are summarized in Table 4.2. The material thicknesses across the wafer of both the 1000 Å and 4000 Å ITO deposition processes were found to be similar, but the former process was much closer to its target thickness.

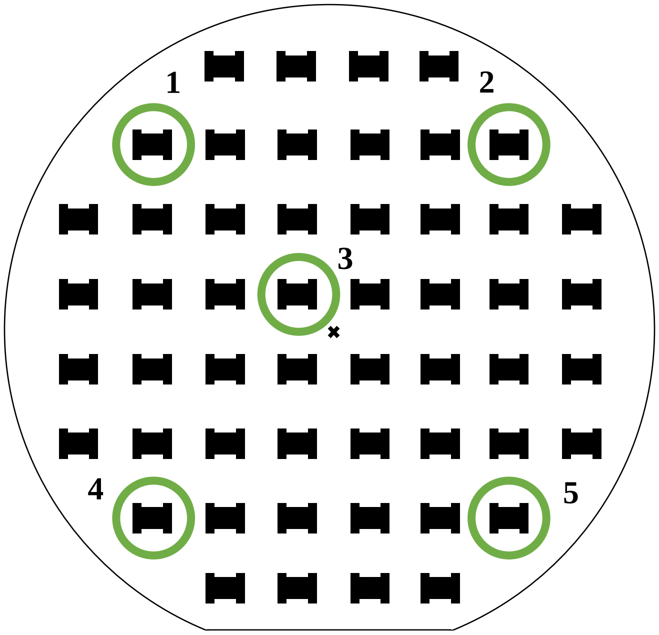

Figure 4.1. Numbered device locations used for thickness measurements.

The metal contact thickness for both wafer splits were similar and very close to the target thickness of 3000 Å. Thickness measurements of Locations 1, 2, 4, and 5 were slightly greater than thickness measurements of features at Location 3; this is consistent with the characteristic “parabolic” shape of thickness profiles sputtered in the CVC 601 DC Sputter Tool discussed in Chapter 3.

Table 4.2. Material thickness versus target thickness of ITO and Al features.

Location	Actual Thickness with 1000 Å Target Thickness of ITO (Å)	Actual Thickness with 4000 Å Target Thickness of ITO (Å)	Actual Thickness with 3000 Å Target Thickness of Al (Å)
1	987.3	3567.4	2934.2
2	985.4	3522.1	2951.6
3	948.9	3409.2	2809.7
4	982.5	3545.0	2975.1
5	988.8	3582.6	2967.0

4.3 Sheet Resistance Measurements

The CDE ResMap 4-Point Resistivity Mapper was used to measure sheet resistance of the ITO on both control wafers to see effects of annealing metal-oxide films. Four-point probe measurements were performed on both control wafers to measure sheet resistance of a 1000 Å metal-oxide layer on 6500 Å of oxide. This is summarized in Table 4.3.

Table 4.3. Statistics of ITO sheet resistance of both control wafers.

R_s (Ω/sq.)	As-deposited ITO	Annealed ITO
Average	660.8	125.9
Standard Deviation	363.7	27.9
Standard Deviation (%)	55%	22%
Minimum	194.6	95.9
Maximum	1433.1	188.8
Range	1238.5	92.9

The sheet resistance measurements indicate that annealing the metal-oxide at a high temperature in the presence of an inert gas drastically decreased the average sheet resistance across the wafer. This is consistent with the theory of recrystallization of the metal-oxide structure under high-heat conditions; crystalline, semiconducting materials tend to have higher conductivity which has been shown with the annealed ITO over the as-deposited ITO [18]. The increase in crystallinity is further demonstrated in Section 4.3.1. In addition, the sheet resistance uniformity is also improved significantly after the annealing process as well. This is beneficial regarding bulk fabrication of devices and ensures a robust, predictable process.

4.4 Microscopic Inspections

Thin film characterization was performed via x-ray diffraction (XRD) and scanning electron microscopy (SEM) to study the effects of annealing on both crystallinity and surface morphology. Basic microscope inspections were also conducted after each step in the fabrication process to ensure completeness of the lift-off processing.

4.4.1 Bruker D8 High-Resolution X-Ray Diffractometer Measurements

The two control wafers in this experiment, after sheet resistance analysis was complete, were further studied via XRD to verify crystalline planes, crystal structure, and an estimated characteristic grain dimension. An XRD instrument was utilized which studies thin film materials as opposed to powders.

The control wafers were cleaved using a diamond scribe; a 9-cm^2 square from each wafer was cleaved and used as samples for XRD analysis. The intensity plots are obtained by measurement of the x-ray intensity when the test material is positioned on a goniometer and set at different angles. Each prevalent peak represents a distinct crystal orientation in the material described as (hkl), with h, k, and l being the Miller indices. The more peaks an intensity graph has, the more crystalline the material is. The intensity graphs for the ITO samples are shown in Figures 4.2 and 4.3.

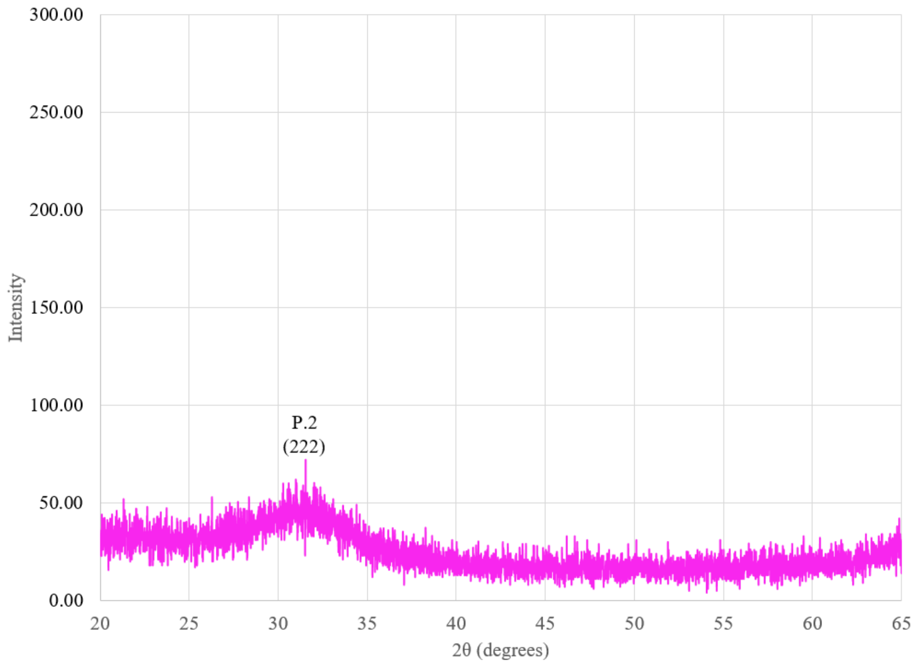

Figure 4.2. XRD intensity graph of as-deposited ITO.

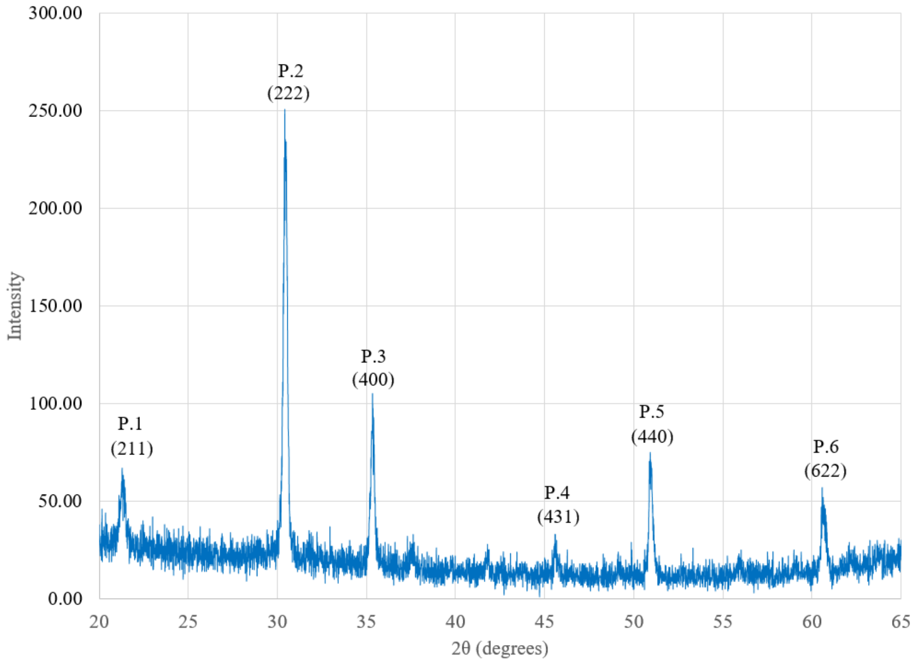

Figure 4.3. XRD intensity graph of annealed ITO.

Annealing the metal-oxide sensing layer, as demonstrated by Figures 4.2 and 4.3, generated more intensity peaks; this is indicative of a change of crystalline structure from an amorphous to polycrystalline state. Each peak's associated crystal plane (denoted in both Figures 4.2 and 4.3) can be determined through a ratio analysis of the sine-squared values of theta at each peak. The smallest sine-squared value is taken and divided through the sine-squared values obtained for the other peaks. Each ratio, denoted as R in Table 4.4, represents ($h^2 + k^2 + l^2$), or the summation of squares of each Miller index in a proposed crystal plane (hkl); ($h^2 + k^2 + l^2$) is directly related to the lattice constant of the material in a cubic crystal system. The ratio of each peak is multiplied by equivalent positive integers until two conditions are met: the determined ratio for each peak must be roughly equal to an integer value and the determined peak ratios should all relate to the theoretically-determined lattice constant of the material in question. Table 4.4 summarizes the ratio analysis performed on the set of data for the annealed ITO.

Table 4.4. Ratio Analysis of XRD Peaks.

Peak #	**2θ**	**$\sin^2\theta$**	**R, $\sin^2\theta$ / 0.0344**	**2R**	**3R**	**4R**	**5R**	**6R**
1	21.37°	0.0344	1	2	**3**	4	5	**6**
2	30.42°	0.0688	2.00	4.00	**6.01**	8.01	10.0	**12.0**
3	35.34°	0.0921	2.68	5.36	**8.04**	10.7	13.4	**16.1**
4	45.58°	0.1500	4.36	8.73	**13.1**	17.5	21.8	**26.2**
5	50.87°	0.1845	5.37	10.7	**16.1**	21.5	26.8	**32.2**
6	60.4°	0.2530	7.36	14.7	**22.1**	29.4	36.8	**44.2**

The ratios of each peak when multiplied by either 3 or 6 (bolded) were very close to integer values; however, upon further analysis, the ratios multiplied by 6 were much closer to the theoretically-determined lattice constant of indium oxide which was taken to be 10.1 Å from literature [13]. Equation 4.1 relates the material's lattice constant with Bragg's Law and Miller indices in a cubic crystal system [24].

$$\frac{n\lambda}{2sin\theta} = \frac{a}{\sqrt{h^2 + k^2 + l^2}} \tag{4.1}$$

Lambda (λ) represents the wavelength of x-ray used (taken to be 1.54 Å for Cu-K alpha radiation in this XRD instrument), theta represents the angle at which the peak occurs, a represents the material's lattice constant, and h, k, and l are the Miller indices of the plane. First-order diffraction is normally assumed in XRD analysis, so n is equal to 1. The values of the lattice constants for each value in the sets of 3R and 6R were found to be 7.2 Å and 10.2 Å, respectively. As a result, the rounded values of the 6R set were used for crystal plane determination.

Each value of ($h^2 + k^2 + l^2$) is characteristic to a family of crystal planes denoted as {hkl}. In a cubic crystal system, each plane in a family of crystal planes is crystallographically equivalent to the others regardless of both the sign and position of the Miller indices in the parentheses [25]; however, when describing the determined crystal plane from XRD analysis, the indices are usually arranged from largest to smallest in the parentheses. Given the largest rounded value of ($h^2 + k^2 + l^2$) to be 44 for Peak 6, a 3-D, 7 × 7 × 7 matrix was programmed in MATLAB to determine all possible 343 (7^3) permutations of ($h^2 + k^2 + l^2$) with integer values between 0 and 6 for h, k, and l. The experimental, rounded values of ($h^2 + k^2 + l^2$) in Table 4.4 were compared with the values from the 3-D matrix and verified via literature values from the Powder Diffraction File [26] (PDF) Database in Table 4.5.

Table 4.5. Experimentally-determined crystal planes versus PDF database.

Peak #	2θ	Rounded ($h^2 + k^2 + l^2$) (experimental)	Potential Crystal Plane(s)	Crystal Plane at each 2θ from PDF Database
1	21.37°	6	(211)	(211)
2	30.42°	12	(222)	(222)
3	35.34°	16	(400)	(400)
4	45.58°	26	(431), (510)	(431)
5	50.87°	32	(440)	(440)
6	60.4°	44	(622)	(622)

Because there are two sets of solutions that satisfy ($h^2 + k^2 + l^2$) for Peak 4, both (431) and (510) were found to be potential crystal planes. Along with the crystal planes, the crystal structure of ITO can also be found using guidelines summarized in Table 4.6. Using these guidelines for cubic crystal structures, the cubic bixbyite structure of ITO, which is base-center cubic structure, is verified; adding up the Miller indices of each specific crystal plane found yields all even numbers which is consistent with the rule defining base-center cubic structures.

Table 4.6. Determinations of crystal structure via Miller indices [27].

Crystal Structure	Diffraction Occurs	Diffraction Does Not Occur
Simple cubic	Value of ($h^2 + k^2 + l^2$) exists	Value of ($h^2 + k^2 + l^2$) does not exist
Base-centered cubic	$h + k + l \equiv$ even number	$h + k + l \equiv$ odd number
Face-centered cubic	h, k, and l are comprised of both odd and even numbers	h, k, and l are either all odd or all even numbers

Short-width, high-intensity peaks are indicative of larger, loose characteristic grains which are optimal for metal-oxide chemical sensor technology; they provide greater surface area for reaction and space for vapor to travel through. Although grain size can be determined using other crystallography methods more accurately, a rough estimate of the minimum grain characteristic length can be obtained via the Scherrer equation [28] using data from an XRD intensity graph (Eq. 4.2).

$$D_t(2\theta) = \frac{K\lambda}{\beta cos\theta} \tag{4.2}$$

D_t represents the characteristic grain dimension, K represents the Scherrer constant (taken to be 0.94 for cubic crystallite shapes [29]), λ represents the wavelength of Cu-K alpha x-rays (1.54 Å), β represents the full width at half maximum (FWHM) of the most prevalent peak (in radians), and θ represents the Bragg angle (in radians) [28]. Both rough estimates of the crystallite sizes and the parameters used to calculate them are summarized in Table 4.7; the increase in crystalline size is drastic when the ITO film is annealed.

Table 4.7. Calculated mean size dimension with specific parameters.

	As-deposited ITO	**Annealed ITO**
β (Δθ)	0.166	0.00873
2θ (rad)	0.545	0.545
D_t (nm)	1.03	19.4

4.4.2 Amray 1830 Scanning Electron Microscopy

The topology of the as-deposited and annealed metal-oxide surfaces were studied using a scanning electron microscope to understand the effects of annealing on surface roughness of the metal-oxide layer. A 25-cm^2 square was cleaved from the center of each control wafer for the study. The sample was placed on a goniometer which was placed inside the microscope chamber. An electron beam from a lanthanum hexaboride (LaB_6) source is utilized to bombard the sample [30]; the electron beam must reach the sample's surface without interactions from the chamber ambient, so a high vacuum between 10^{-5} and 10^{-6} torr was established before microscopy is conducted. This also ensures the sensitive filament does not burn out at atmospheric pressure.

The micrographs (Figure 4.4) were taken towards the edges of the samples to focus on small particulates that were created when the wafers were cleaved. The magnification of both micrographs was roughly 10,000x.

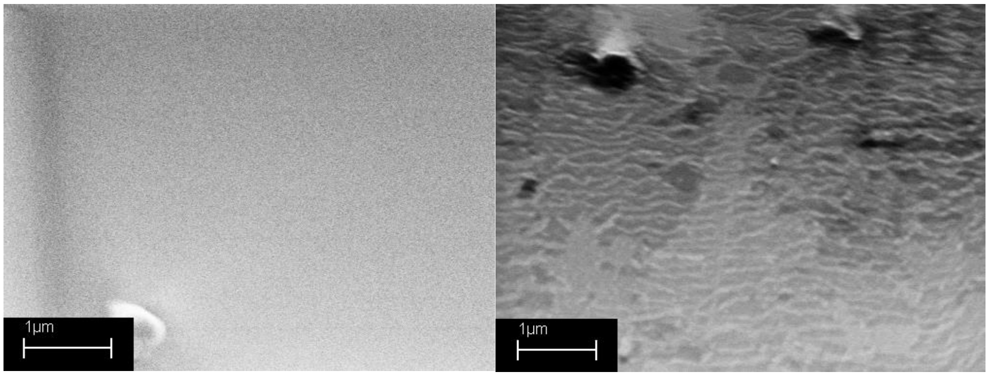

Figure 4.4. Surface morphology of as-deposited (left) and annealed (right) ITO.

As demonstrated, annealing the metal-oxide generates surface topology which was relatively consistent with what was found from the Scherrer equation. The as-deposited ITO had a very smooth surface with small crystallites that could not be imaged via SEM accurately. On the other hand, the annealed ITO had noticeable grain boundaries with grooves which allow for increased surface area for adsorption sites. The surface-area-to-volume ratio is technically greater for the as-deposited ITO grains compared to the annealed ITO; however, the benefit of the increase of surface area for these smaller grains is inhibited due to their closely-packed formation which decreases the amount of available adsorption sites and the ability for gases to react with adsorbed oxygen at those sites [31].

4.4.3 Leica Microscopy

Microscopy was done using the Leica inspection station in the SMFL after each processing step to ensure the lift-off processes of each of the metals were successful. Because the feature sizes of the devices were on the order of millimeters and were therefore too large to be seen using this specific microscope, the lowest order of magnification (5x) was utilized. The edge boundary of the left side of the metal-oxide square was imaged after each process to qualify the lift-off resist and to determine if any metal still remained in undesired locations either through incomplete lift off of the photoresist or redeposition of the lifted-off metal during the lift-off process. Figure 4.5 demonstrates the process flow of the fabrication with each step and material labeled.

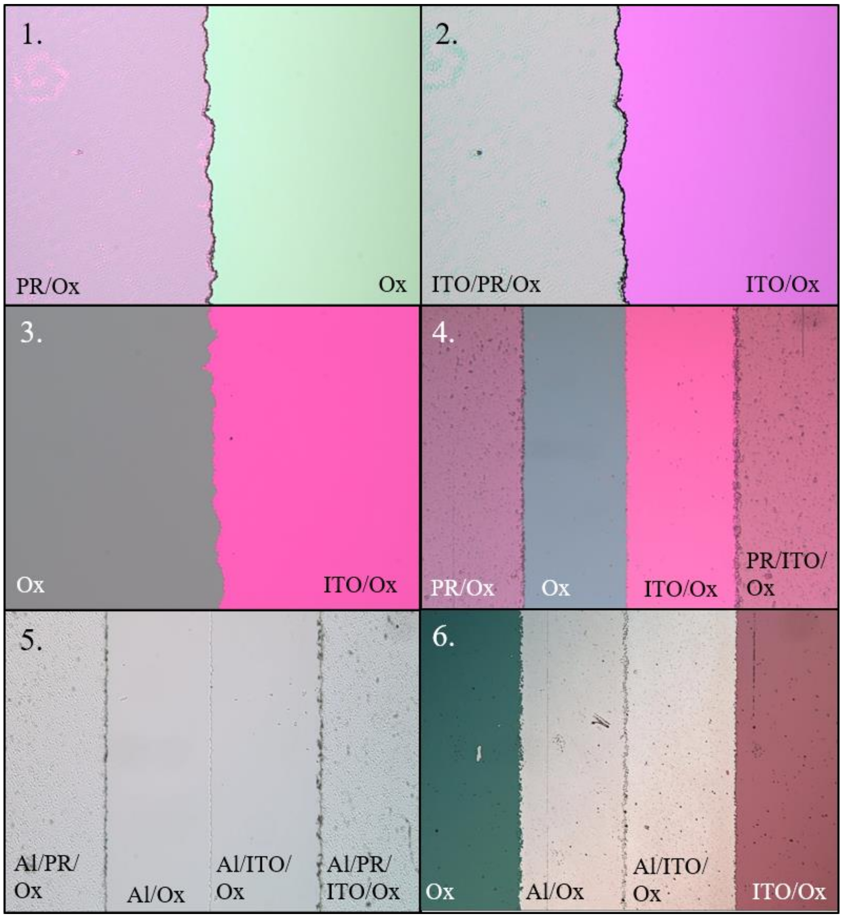

Figure 4.5. Micrographs steps in fabrication for 100 nm ITO thickness.

The numbers at the top left of each micrograph correspond to the steps in the process and are summarized as follows:

1. Preparation of lift-off photoresist (PR) before ITO sputter on oxide (Ox)
2. After ITO sputter, before ITO lift-off process
3. After ITO lift-off process
4. Preparation of lift-off photoresist before Al sputter on ITO on oxide (Ox)
5. After Al sputter, before Al lift-off process
6. After Al lift-off process

As shown in micrographs 1, 2, and 3, the lift-off photoresist had, and subsequently imaged, a rough ITO edge boundary. This, in most cases, is due to light scattering occurring between both the mask and the photoresist surface. However, due to the large feature sizes of these chemical sensors, the change of dimension from the edge roughness is not enough to inhibit the performance of the devices. Nevertheless, a way to mitigate light scattering for lift-off processing of smaller feature sizes is to ensure as close contact as possible between the mask and the resist surface [32]. However, in practical applications, the transparency mask will always have small amounts of particulates on its surface due to the presence of static charge on the cellulose acetate’s surface; quartz would make a better mask material as it is much easier to clean and will not be soluble with organic solvents like cellulose acetate and the printed ink pattern.

During the timeframe in which the second lift-off process was completed, the SSI Track had technical difficulties regarding its spin-coating system on Track 1; the spin-coater could not keep a constant rotational speed for the duration in which the photoresist was spun on. This may potentially be the reason why the lift-off photoresist had holes in it (micrographs 4 in Figure 4.5) as there was most likely variations of photoresist thickness across the wafer due to the varying rotational speeds which would be most noticeable after the post-exposure bake. Particulates from the cellulose acetate mask could have also contributed to the holes in the photoresist, but the masks went through the same cleaning procedure and, as demonstrated in micrograph 1 in Figure 4.5, the lift-off photoresist had excellent uniformity.

Comparing the lift-off processes through these micrographs, it is demonstrated that the ITO lift-off process was much more successful compared to the Al lift-off process based on the greater amount of particulates generated on the device surface after the Al lift-off process. The particulates shown on the Al contact surface in micrograph 6 of Figure 4.5 could have been generated through two sources: potential particulates from the photoresist preparation or from redeposition of the lifted-off metal dispersed in the photoresist remover. The same amount of photoresist remover was used in both lift-off processes which may explain the increase of particulates because more Al was deposited (300 nm) compared to ITO (100 nm). This alone would increase the metal particulate concentration in the solvent during the lift-off process and subsequently increase chances of redeposition. This can also be shown through micrographs of the 100 nm and 400 nm target deposition processes of ITO as well (Figure 4.6).

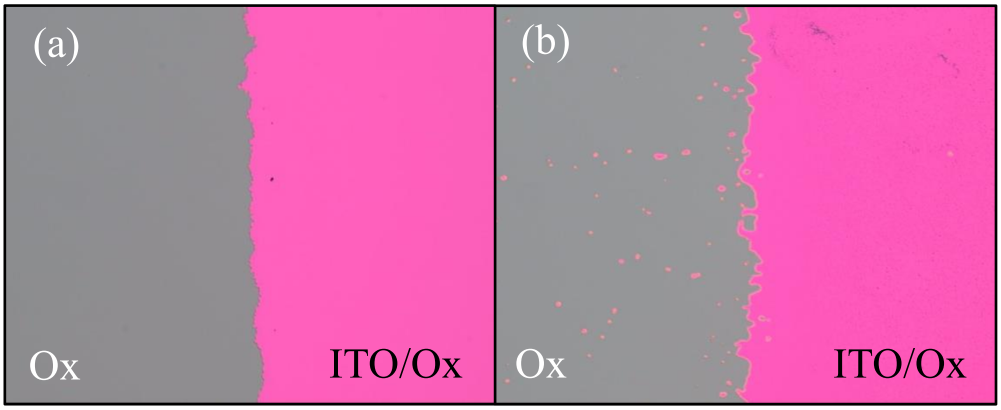

Figure 4.6. Lift-off process of ITO for 100 nm (a) and 400 nm (b) thickness.

This reaffirms the importance of ensuring small deposited material thicknesses for lift-off processing. The remover solution was filtered and an additional acetone rinse was done on the wafer surface before each of the micrographs were taken, but even then, it has proven to not remove all particulates generated in the photoresist dissolution.

4.5 Conclusion

The characterization methods utilized in this thesis, including thickness measurements, sheet resistance characterization, and microscopic inspection, are discussed. All of the thicknesses measured in both the control wafers and test wafers were found to be relatively precise, but the lower thickness deposition of ITO was found to be more comparable with the target thickness compared to the higher thickness deposition of ITO. The sheet resistance of the ITO was found to be lower and more uniform when it was annealed compared to when it was measured as-deposited. Using XRD, the annealed ITO yielded more noticeable peaks compared to as-deposited ITO which indicates higher crystallinity. The crystalline structure of ITO was also proven using the sine-squared indexing method of finding crystalline planes and relating these findings to guidelines of Miller indices in each plane and how it relates to crystal structure. The grain sizes of as-deposited and annealed ITO were calculated by the Scherrer equation and the characteristic length of annealed ITO grains were found to be greater compared to as-deposited ITO grains. This increase in surface roughness in annealed ITO was also demonstrated through SEM analysis of the ITO-covered control wafers. Lastly, micrographs obtained using a Leica microscope demonstrated the effects of light scattering due to mask interference. The micrographs also showed higher effectiveness of particulate removal from the wafer with lower metal thickness deposition processes.

Chapter 5

Sensitivity Measurements of Chemical Sensors

5.1 Introduction

This chapter describes the initial and standard methods used to test the sensitivity of the fabricated metal-oxide chemical sensors. The testing procedures for both initial and standard methods used, along with associated apparatuses and equipment used to obtain the measurements, are discussed. The results obtained from both procedures are analyzed in this chapter and conclusions are drawn regarding the effects of metal-oxide thickness, crystalline structure/morphology, volatile organic compound concentration, and temperature on chemical sensitivity and metal-oxide activation energy.

5.2 Initial Testing Procedure and Results for Short Exposures

Before rigorous testing was done on individual devices in consistent ambient conditions, initial tests were done on the device wafer in 35% relative humidity (RH) to confirm response to volatile organic compounds, analyze recovery time curves, and investigate effects of humidity on device performance. The 400-nm metal-oxide thickness lots were not completed yet, so the 100-nm as-deposited and annealed ITO devices were tested. To maintain consistency with differences of metal-oxide thickness across the two wafers, a device in proximity to the alignment mark in the center was tested in the same place across the device wafers. Due to safety concerns with the hot plate in the electrical testing laboratory, the maximum temperature utilized in the initial tests was 350°C.

5.2.1 *Initial Testing Apparatus*

A hot plate was used to bring the wafer, and subsequently the metal-oxide layer, to uniform, high temperatures to ensure adsorption of ambient oxygen to the metal-oxide and chemical reaction of the volatile organic compound with the adsorbed oxygen. Surface temperatures were confirmed using a thermocouple. Probes were placed on the metal contacts of an individual device on the wafer for resistance measurements. The probes were wired to an electrical box which was connected to an HP 4145B Semiconductor Parameter Analyzer to actively measure the resistance over time using Metrics Interactive Characterization Software (ICS). The hot plate set-up is shown in Figure 5.1.

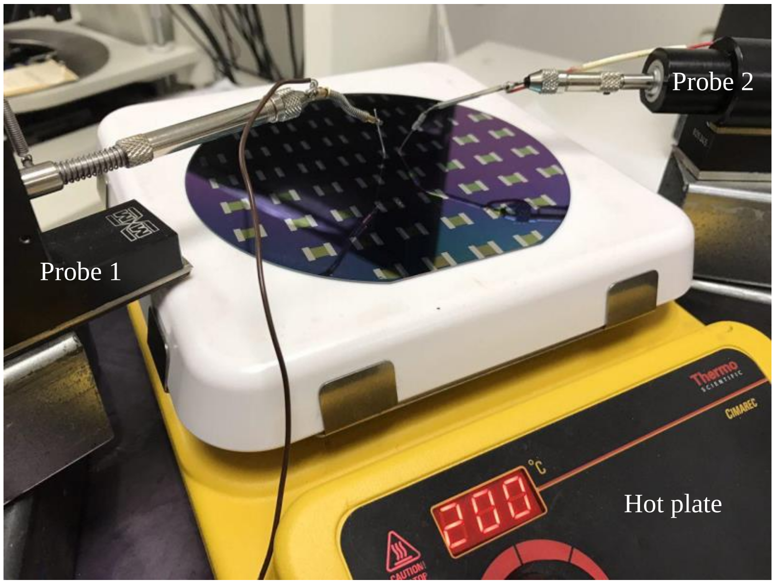

Figure 5.1. Initial chemical sensitivity testing set-up for short exposures.

A resistor was modeled in the ICS and both leads to the resistor were defined as SMU1 (Probe 1) and SMU2 (Probe 2). SMU1 was set to supply a constant voltage of 3 V and SMU2 was grounded. Both the voltage and current drops were measured automatically across the resistor; the resistance, given constant voltage and changing current over time, was calculated in the software using Ohm's Law and output in a data file. The sensitivity of the devices in both the initial and standard testing procedures was calculated in the same manner using Equation 5.1, as defined by Chandra et al [16].

$$S = \frac{R_0 - R_G}{R_G} \tag{5.1}$$

R_0 and R_G represent the steady-state resistances before and after exposure to ethanol, respectively. This is done to normalize the resistances to solely measure chemical sensitivity as crystal structure, thickness, and temperature of the metal-oxide will change the measured resistance as well. Two 100-mL spray bottles with fine mist spray nozzles were filled with the testing solutions: water and an ethanol solution of roughly 40% by volume ethanol and the rest tap water. The ethanol was diluted with water to increase its flash point to make it safer to work with in a semi-open setting. For each test, the measurement was ran for thirty seconds and then the solution was sprayed once above the apparatus. A portion of the high heat transferred via conduction from the hot plate surface to the wafer was transferred from the wafer surface to the air via convection; this created a small, high-heat region above the wafer surface to quickly evaporate the mist droplets.

It is imperative to ensure small, less-concentrated droplets are created from the spray when doing this test; larger droplets have smaller surface-area-to-volume ratio and will land and skid across the wafer surface due to the Leidenfrost effect; the bottom of a large droplet will evaporate more quickly than the top and, as a result, create an insulating barrier of vapor between the liquid and the hot surface and cause delayed evaporation. To ensure optimum surface-area-to-volume ratio of the fine droplets in the mist for evaporation, the bottles were sprayed about a half a meter above the actual apparatus upwards so the droplets would spread far enough apart from air resistance to mitigate surface cooling which may result from highly concentrated mist. The concentration naturally "decreased" over time as the alcohol was dispersed in the surrounding ambient and the evaporation rate was assumed to be similar for each tested temperature.

5.2.2 Short Response of 100-nm, As-Deposited ITO to Ethanol

The response to the ethanol solution was studied with an as-deposited ITO chemical sensor in the center of the device wafer at different temperatures. The sensitivity data was taken and is summarized in Figure 5.2.

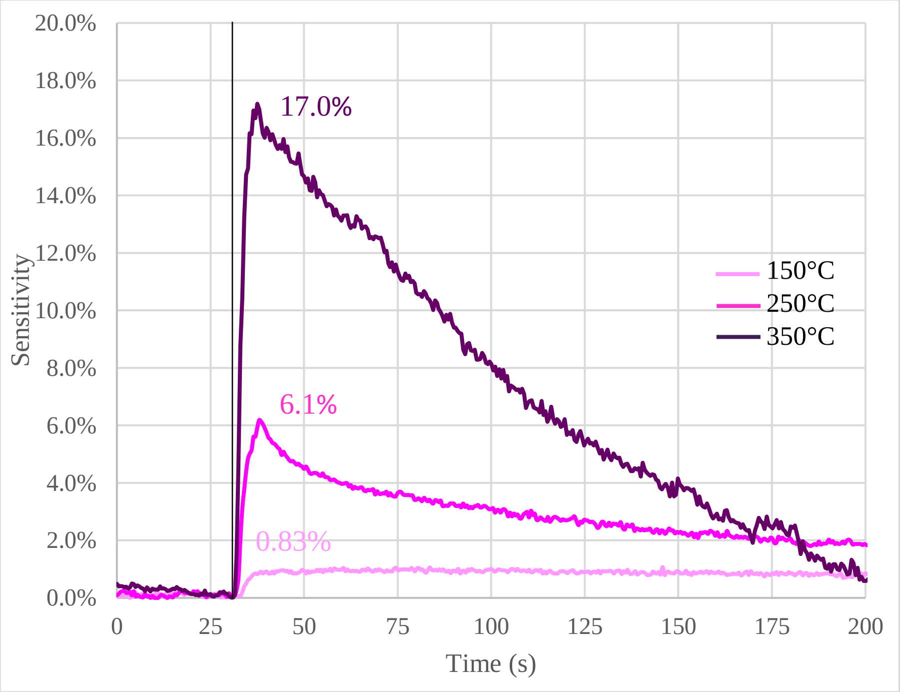

Figure 5.2. 100-nm, as-deposited ITO short response to EtOH at varied temperatures.

As shown, higher temperatures of operation result in much greater sensitivity readings from short ethanol exposure and faster recovery time to 0% sensitivity. This is due to more energy available which allows for enhanced adsorption of oxygen and increased rate of reaction of the ethanol. The steady decrease of sensitivity after ethanol exposure for the trials at different temperatures is characteristic with relative low surface area for adsorption as described by the Langmuir adsorption isotherm model discussed in Chapter 2. Higher temperatures of device operation recovered more closely to their original resistance values at 0% sensitivity which may demonstrate greater reactivity of the ethanol and evaporation of the water in the solution. Lower temperatures reached lower resistance equilibrium states which may indicate blocking of oxygen adsorption sites due to incomplete, aforementioned phenomena of ethanol and water with the metal-oxide.

5.2.3 Short Response of 100-nm, Annealed ITO to Ethanol

The response to the ethanol solution was also studied with the 100-nm, annealed ITO chemical sensors at different temperatures with a chemical sensor at the center of the device wafer and is summarized in Figure 5.3.

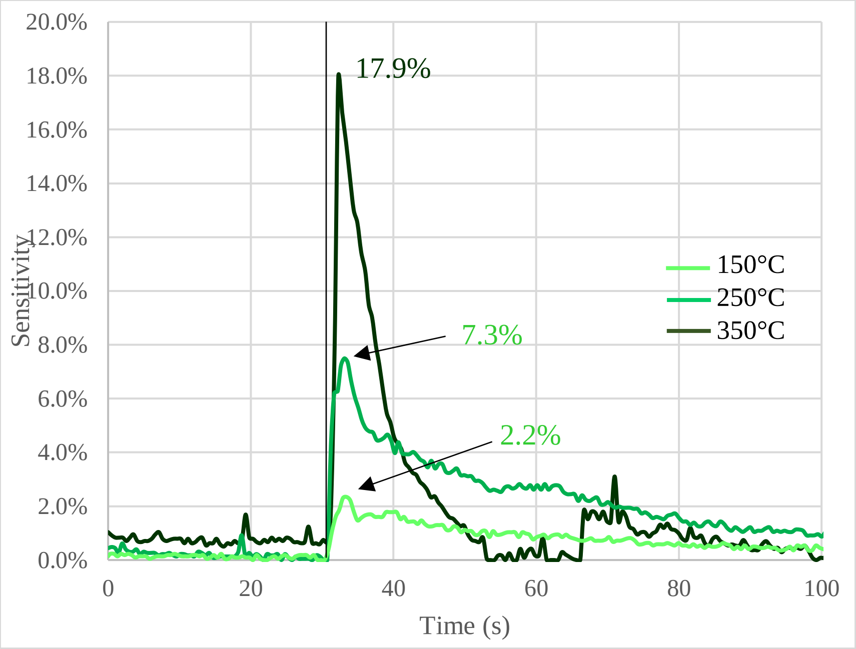

Figure 5.3. 100-nm, annealed ITO short response to EtOH at varied temperatures.

Annealing the ITO slightly improved the sensitivity of the devices at each operating temperature from short exposure to ethanol. However, the recovery time improved significantly and was shorter compared to as-deposited ITO chemical sensors. This demonstrates higher surface area based on the Langmuir adsorption isotherm model compared to the as-deposited ITO and also confirms what was found in the characterization of the metal-oxide surface area in Chapter 4. The sensitivity of the chemical sensors after the recovery time was also much closer to 0% which demonstrates enhanced chemical reactivity and product removal from ethanol oxidation so that more oxygen can readsorb.

5.2.4 Short Response of 100-nm, As-Deposited ITO to Water

The response to water was studied with the 100-nm, as-deposited ITO chemical sensors at different temperatures with a chemical sensor at the center of the device wafer and is summarized in Figure 5.4.

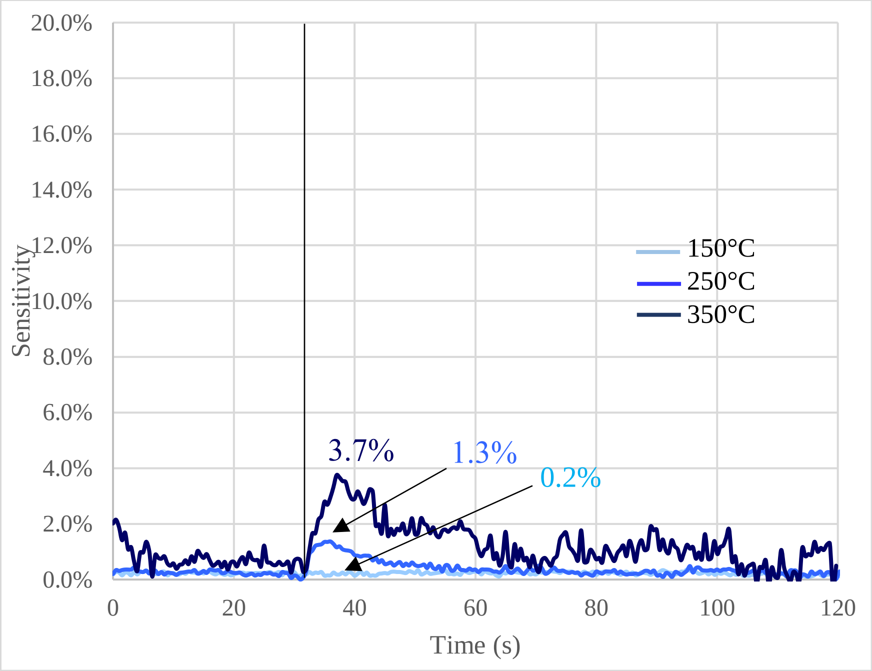

Figure 5.4. 100-nm, as-deposited ITO short response to water at varied temperatures.

The as-deposited ITO chemical sensors had some response to the water, but not as much as to ethanol. The effect is relatively short-lived as the sensor returns back to its original resistance value fairly quickly. High humidity, at temperatures above 200°C, will cause chemisorption of water to the oxygen adsorption sites. Each chemisorbed water molecule dissociates and forms two hydroxyl ions and blocks any further oxygen from adsorbing to those sites. The chemisorption of water increases the conductivity and is suspected to slightly increase the sensitivity in this experiment, but the sensitivity increase is more likely to be from ionic compounds in the water itself. Significant water chemisorption occurs only after prolonged exposure to high humidity whereas the time of exposure to water in the initial tests were relatively small. In practice, a way of mitigating effects of humidity is operating the device at higher temperatures than ones tested in this thesis. At temperatures slightly above 400°C, the hydroxyl ions will begin to desorb from the metal-oxide and the adsorption sites will be freed for oxygen adsorption [33].

5.2.5 *Short Response of 100-nm, Annealed ITO to Water*

The response to water was studied with the 100-nm, annealed ITO chemical sensors at different temperatures with a chemical sensor at the center of the device wafer and is summarized in Figure 5.5.

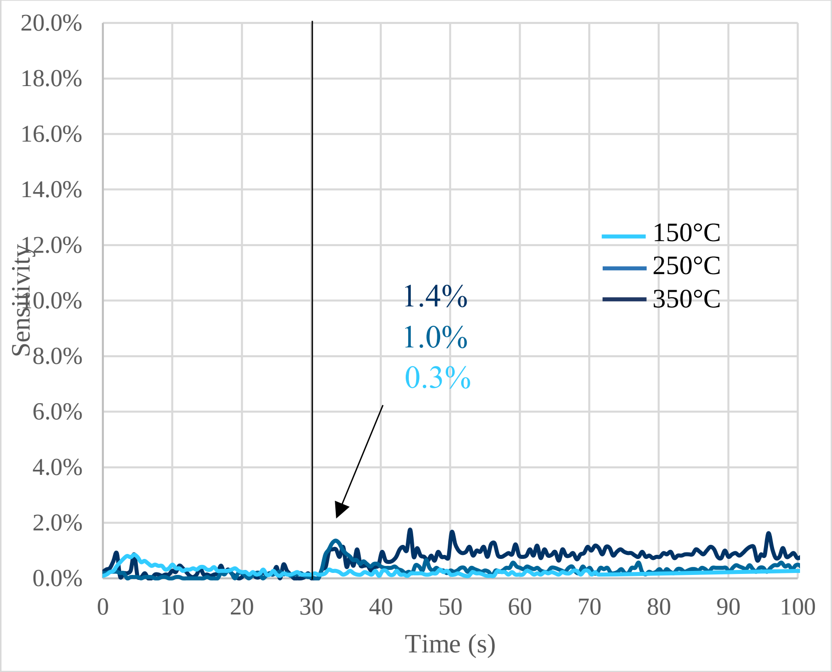

Figure 5.5. 100-nm, annealed ITO short response to water at varied temperatures.

Annealing the metal-oxide layer was shown to mitigate the effects of humidity on sensitivity. This may be due to increased surface area in the annealed ITO compared to as-deposited ITO. The volume of water used in both tests were the same which may indicate both the water adsorption and ionic compounds accounted for smaller fractions of the total surface area. However, after exposure to water at an operating temperature 350°C, the sensitivity reading stayed relatively constant after exposure as it did with the as-deposited ITO sensors which may indicate ionic compounds left on the sensing layer and, to a lesser extent, a greater amount of hydroxyl groups formed. As stated before, heating the sensor to temperatures above 400°C will allow the hydroxyl groups to desorb, allow oxygen to readsorb, and increase the resistance to the sensor's original value of R_0.

5.3 Standard Testing Procedure and Results for Prolonged Exposures

A robust testing procedure was developed to understand the effects of prolonged, constant exposure of pure, 200-proof ethanol at different concentrations in air ambient with 35% RH. The effects of ethanol concentration, crystalline structure, metal-oxide thickness, and temperature were studied. The effects of temperature on steady-state resistance of each device structure were analyzed. An Arrhenius relationship was used to characterize the activation energy of each sensor. As done in the previous testing procedure, a single device in the center of the wafer was analyzed on the same area of each of the device wafers.

5.3.1 Standard Testing Apparatus

The apparatus used for prolonged exposure to ethanol was a burn box with a steel plate insert at the bottom to hold the magnetic probes in place. A square, metal-ceramic 100 mm^2 heater suspended in air was used to heat the devices; the temperature varied depending on the voltage put through the heater. The temperatures at different voltages were determined using a thermocouple and are summarized in Table 5.1. The temperature of the sensor surface was verified to be the temperatures that were found at each voltage.

Table 5.1. Characterization of metal-ceramic heater.

Voltage (V)	**Measured Temperature (°C)**
1	160
2	260
3	360

The wires used to connect the heater and the probes were put through holes in the back of the chamber and secured with HVAC foil tape to maintain relatively consistent ethanol concentration. The inside of the chamber set-up is shown in Figure 5.6.

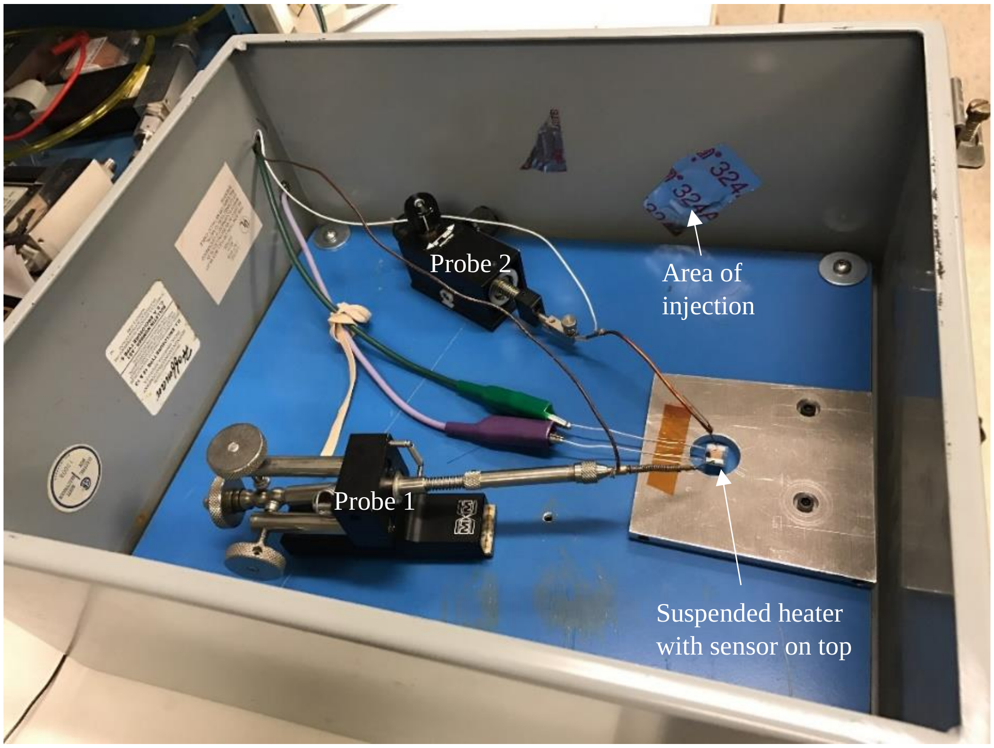

Figure 5.6. Standard chemical sensitivity testing set-up for prolonged exposures.

The ethanol was injected into the test chamber using a micropipette fit with a needle in an opening close to the sensor from the bottom of the box; given the chamber volume, liquid volume, liquid density, molar volume of air, and ethanol's molecular weight, the concentration of ethanol in the chamber, C_E, can be calculated using a manipulation of the ideal gas equation (Equation 5.2).

$$C_E = \frac{\rho_E V_E}{W_E} \frac{V_m}{V_{ch}} \tag{5.2}$$

ρ_E is the density of ethanol (taken to be 789 kg/m^3 at room temperature [34]) and W_E is the molecular weight of ethanol (taken to be 46.042 g/mol [35]). Given a volume of ethanol, V_E, the number of moles of ethanol in the chamber can be calculated. This is subsequently multiplied by the ratio of the molar volume of air (V_m) to the chamber volume (V_{ch}). At standard temperature and pressure (STP), the calculated molar volume of air is roughly 22.4 L/mol. The chamber itself has a volume of roughly 0.01365 m^3. Given these values, the required volumes to emulate specific concentrations in the chamber were calculated and are summarized in Table 5.2. Larger concentrations were used for testing to clearly see the change of resistance due to inherent noise generated from measurements.

Table 5.2. Calculated ethanol volumes for target testing concentrations.

Target concentration (ppm)	**Required Volume (µL)**
500	16
1000	33
1500	49
2000	65

The hole was quickly closed after injection of the ethanol. After each test, the ambient ethanol in the chamber was removed using a portable vacuum and the inside surfaces were wiped with a wet cloth to remove any condensed ethanol vapor. The electrical testing conditions that were done in ICS for the previous resistor testing, including determination of sensitivity, were repeated for this testing set-up as well. All prolonged exposure tests were run for 100 seconds.

5.3.2 Temperature Dependence on Metal-Oxide Resistance

A study of change of resistance was conducted for the metal-oxide layers of each device wafer at different temperatures. Each of the sensors that were salvaged from each device wafer were tested in the chamber. The lid of the testing chamber was left open. The operating temperature was manipulated using the voltages described in Table 5.1. It took about a minute for each of the devices to reach a constant resistance value. The average resistance values and the standard deviation, σ, of the resistance measurements (also denoted by vertical error bars) are summarized in Figure 5.7. Devices that were closest to the average resistance value for each wafer at each temperature were used for testing.

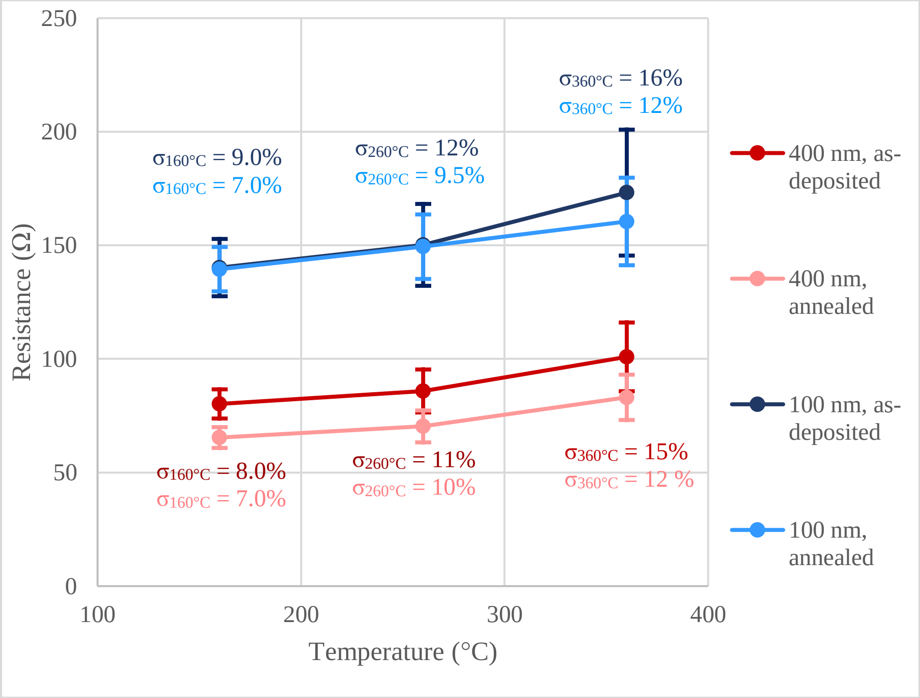

Figure 5.7. Temperature variations of metal-oxide layers for each device wafer.

The resistance variation (as described by the standard deviation) across all sensors in a specific device wafer is more pronounced as the temperature of operation increases.

As confirmed from sheet resistance measurements taken in Chapter 4, annealing the metal-oxide layer decreased the metal-oxide resistance in both the 100-nm and 400-nm processes; however, the drop in resistance was more pronounced with the 400-nm process compared to the 100-nm process. The percent changes of resistance between 160°C and 260°C for the four types of devices (between 7-8%) were found to be less compared to the change of resistance between 260°C and 360°C (between 15-20%). However, this was not found with regards to the 100-nm annealed metal-oxide film, which gave a percent change of resistance from 260°C and 360°C of only 7.5%. This may be an indication that thinner metal-oxide films which are crystalline tend to be more electrically stable with changes of temperatures compared to their amorphous counterparts. More oxygen adsorption sites for the 100-nm annealed metal-oxide layers may have been filled at lower temperatures which also may explain why the resistance did not change as much at higher temperatures compared to other devices; oxygen adsorption may begin to occur at temperatures as low as 250°C assuming the metal-oxide layer has a sufficient amount of surface area [6]. This combination of lower-temperature oxygen adsorption and electrical stability with increasing temperature makes thin, annealed metal-oxide films an optimal choice.

5.3.3 Maximum Sensitivity Determination

Due to large amounts of noise generated from the measurements from the probes measuring high-temperature surfaces, the results were leveled via exponential smoothing using Equation 5.3.

$$s_t = \alpha \cdot x_t + (1 - \alpha) \cdot s_{t-1} \tag{5.3}$$

s_t represents the smoothed value which is a weighted average of the current value, x_t, and the previous smoothed value, s_{t-1}. The weight is carried out by the smoothing factor, α, which was taken to be 0.1; smaller smoothing factors will further level the data. The maximum sensitivity value was taken to be the weighted average of the plateau of the highest sensitivity readings after exposure to ethanol. Each test for each device structure was taken at the same operating temperature with different ambient ethanol concentrations. Figure 5.8 demonstrates an example of exponentially-smoothed results obtained for the response of different ethanol concentrations to 100-nm, annealed ITO at 360°C with average maximum sensitivity values indicated with each concentration. The other smoothed graphs can be found in Appendix A.

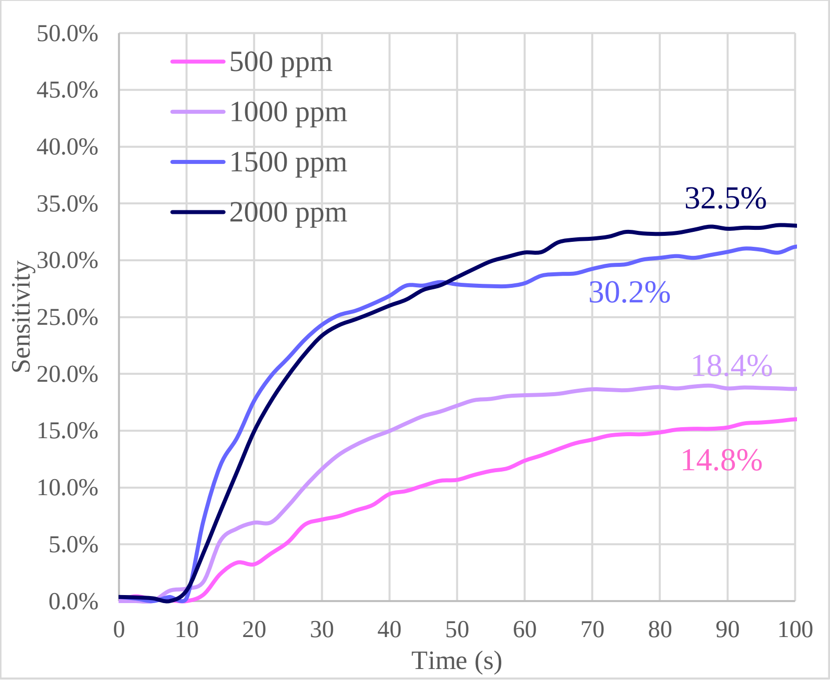

Figure 5.8. 100-nm, annealed ITO response to prolonged EtOH conc. at 360°C.

5.3.4 *Effects of Concentration on Sensitivity of Prolonged Exposures*

The effects of ethanol concentration were similar with all tested device structures; the maximum sensitivity increased as the ethanol concentration increased. However, the increase was much more evident with certain structures as shown in Figure 5.9 with the device operating temperature set at 360°C.

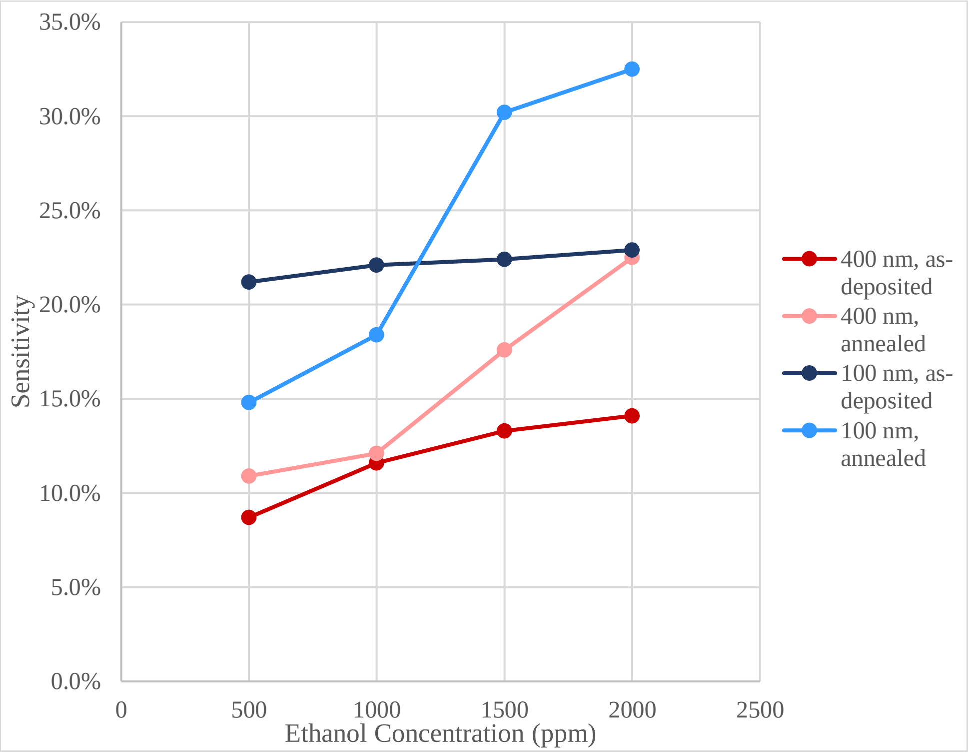

Figure 5.9. Sensor response to ethanol concentrations at 360°C.

Annealing the metal-oxide, in both the 100-nm and 400-nm metal-oxide devices, caused a much greater increase in sensitivity with increase of ethanol concentration. The greater change of sensitivity with crystallinity, as demonstrated by the previous short exposure tests, is also consistent with the Langmuir adsorption isotherm model; a larger change of sensitivity (which can be related to fluctuations in the number of oxygen adsorption sites) with respect to changes in reducing gas concentration is characteristic of larger material surface area with more oxygen adsorption sites. The annealed metal-oxide layers also give more pronounced differences of sensitivity in between concentration readings. Larger changes of sensitivity is beneficial as it creates a larger range of sensitivity values which enables easily-distinguishable values of concentration that correspond to each sensitivity value. As-deposited ITO sensors gave smaller ranges of sensitivity over the tested concentrations which, as demonstrated by Figure 5.10, gave what seemed to be saturated readings that could potentially lead to errors in concentration determination in practical devices.

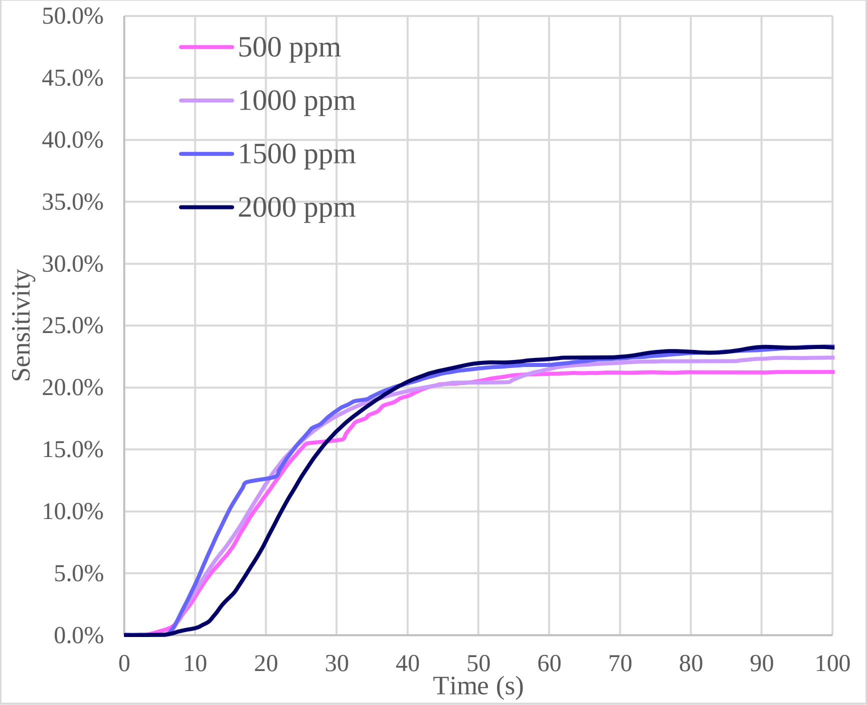

Figure 5.10. 100-nm, as-deposited ITO response to prolonged EtOH conc. at 360°C.

Figure 5.9 also demonstrates the effects of metal-oxide thickness on sensitivity as well. The measured sensitivity of the 400-nm devices at each ethanol concentration was found to be less than the sensitivity found for the 100-nm devices. In addition, the range of sensitivity values was found to be greater for the annealed, 100-nm device compared to its

400-nm counterpart. This may be due to the mass-transfer limited nature of the depletion layer that forms towards the surface of the metal-oxide [16]. A more noticeable change in resistance will occur as the thickness of the oxidized depletion layer becomes comparable to the metal-oxide thickness itself.

5.3.5 Empirical Determination of Activation Energy of Sensors

The effects of annealing the metal-oxide and temperature on activation energy were studied for the four device structures; this energy value was determined for each sensor using an Arrhenius relationship (Equation 5.4) of the changes of resistance for the 2000 ppm concentration tests as they yielded the strongest signals to changes of sensitivity.

$$lnR_g = lnR_0 + \frac{\Delta E_A}{k_B T} \tag{5.4}$$

R_0 and R_g represent the resistance values of the sensors before and after exposure to ethanol, respectively, T is the temperature, k_B is the Boltzmann constant taken to be approximately 8.62×10^{-5} eV/K, and E_A is the activation energy. Equation 5.4 can be manipulated and plotted $\ln(R_g / R_0)$ versus inverse temperature. The Arrhenius relationship of each analyzed device structure is shown in graphical form in Figure 5.11.

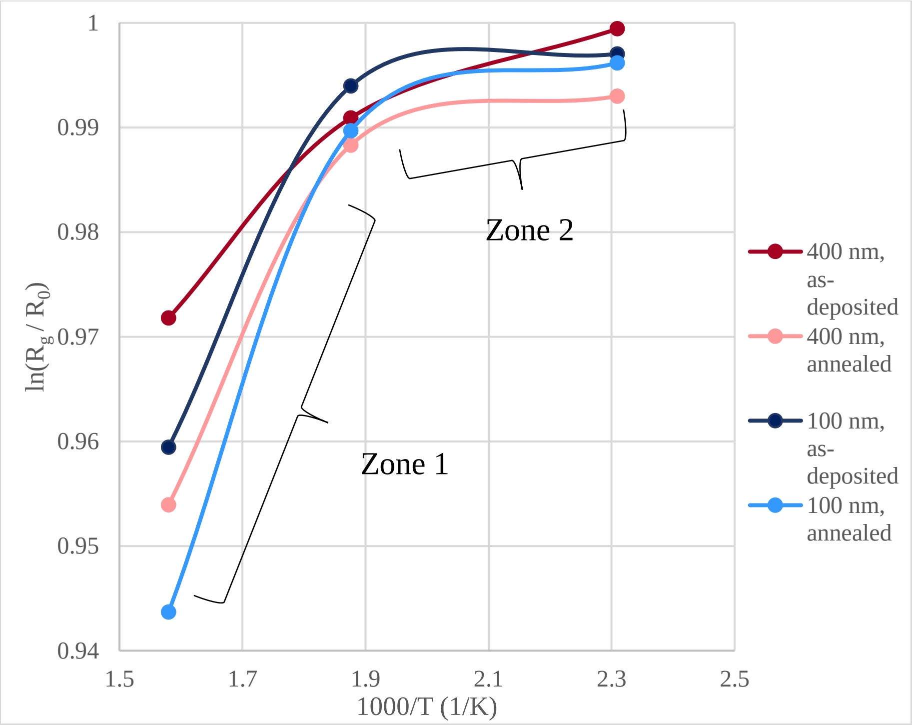

Figure 5.11. Empirical determination of EA with ln(Rg / R0) versus 1000/T.

The Arrhenius relationships shown in Figure 5.11 demonstrate that the activation energy of the ITO material system is very responsive to changes in temperature. This phenomenon can also be seen in other metal-oxides such as n-type zinc oxide as demonstrated by Yadav et al [36]. Due to this effect, there are two linear zones (denoted in Figure 5.11) which exhibit different slopes and, consequently, different activation energies. The slope between two points in this graph represents E_A/k_B; from here, the activation energy can be determined by simply multiplying the slope by the Boltzmann constant. The resulting activation energies for each device structure within each temperature zone are summarized in Table 5.3.

Table 5.3. Activation energies of each device structure at different temperature zones.

Device Structure	E_A between 160°C and 260°C (eV)	E_A between 260°C and 360°C (eV)
400 nm, as-deposited	1.69×10^{-3}	5.56×10^{-3}
400 nm, annealed	9.31×10^{-4}	1.00×10^{-2}
100 nm, as-deposited	6.11×10^{-4}	1.00×10^{-2}
100 nm, annealed	1.29×10^{-3}	1.34×10^{-2}

At higher temperatures, the activation energy was found to increase drastically between one to two orders of magnitude. In most cases, the activation energy was found to increase when the metal-oxide was annealed; higher activation energies, based on findings from Black regarding electromigration in thin films, correlate with larger grain structures [37]. The effects of grain boundary scattering are mitigated as the grain size increases; smaller grains exhibit more grain boundaries which, in return, increases the resistance of the electrical path across the metal-oxide. This phenomenon itself has been documented in studies of annealed ITO and nickel nanostructures from Sobri et al [38]. However, this was not found with the 400-nm devices between 160°C and 260°C which may indicate more grain boundaries beneath the depletion region compared to the 100-nm devices.

5.4 Conclusion

Both the short and prolonged exposure testing procedures were discussed in detail, including the apparatuses and software used to facilitate the measurements. The short exposure tests were done using solutions that were sprayed in a fine mist on the chemical sensors to ensure evaporation on the hot surface of the wafer. The annealed ITO devices tested with both short and prolonged exposures gave higher sensitivity readings to the ethanol compared to their as-deposited ITO counterpart devices. In addition, in the short exposure tests, annealed ITO devices had a more drastic change of sensitivity back to steady state after exposure compared to as-deposited ITO devices which could be due to higher adsorption surface area. The devices did not give a noticeable change of sensitivity to tap water in short exposures; annealing the ITO decreased the sensitivity to water. Increasing the temperature was found to drastically increase the sensitivity for all measurements; at lower temperatures of operation for the devices in short exposures, the resistance did not go back to its normal state which could indicate the blocking of oxygen adsorption sites due to incomplete reaction or physical blocking from the ethanol. The steady-state resistance of the devices in air increased with increasing temperature due to both oxygen adsorption and the metallic nature of the metal-oxide layer itself. The devices showed increased sensitivity to increasing ethanol concentration using the prolonged ethanol exposure test. The variation of sensitivity values, however, was greater for the annealed ITO devices compared to the as-deposited ITO devices; this allows for clearer distinctions between concentration values. Thinner metal-oxide films were found to be more sensitive. The activation energy of each device was strongly dependent on temperature and was split into two separate activation energies in the Arrhenius relationship for each temperature range tested. Annealing the metal-oxide layer increased the activation energy more noticeably in higher temperatures of operation.

Chapter 6

Device Design and Simulations of Chemical Sensor for Future Work

6.1 Introduction

This chapter details electrical and thermal simulations done on a micrometer-scaled chemical sensor designed for future work. The basic design of the simulated chemical sensor is discussed, along with a proposed fabrication process and basic electrical characteristics. The thermal simulation, along with key parameters and assumptions, are discussed. The electrical simulation, along with key parameters and assumptions, is done to explore how metal-oxide thickness and oxygen vacancy concentration affect sensitivity; temperature effects on change of steady-state resistance are also investigated.

6.2 Process/Device Design of Future Work Chemical Sensor

Although the chemical sensors fabricated and tested in this thesis proved core concepts of metal-oxide chemical sensor working mechanisms, it is unlikely that these specific sensors could be put into a true microsystem because the active sensing area is too large and the device itself does not have a reliable way of heating itself to high temperatures without the use an external heating source. To address these two matters, a micrometer-scaled metal-oxide chemical sensor was designed in Mentor Graphics software. A basic fabrication process for the sensor was also developed.

6.2.1 High-Level Fabrication Process of Proposed Chemical Sensor

To discuss the structure of the device and corresponding dimensions of the sensor features, a scope of the process flow of the fabrication process, including 3-D views of each step in both directions, is summarized in Figure 6.1.

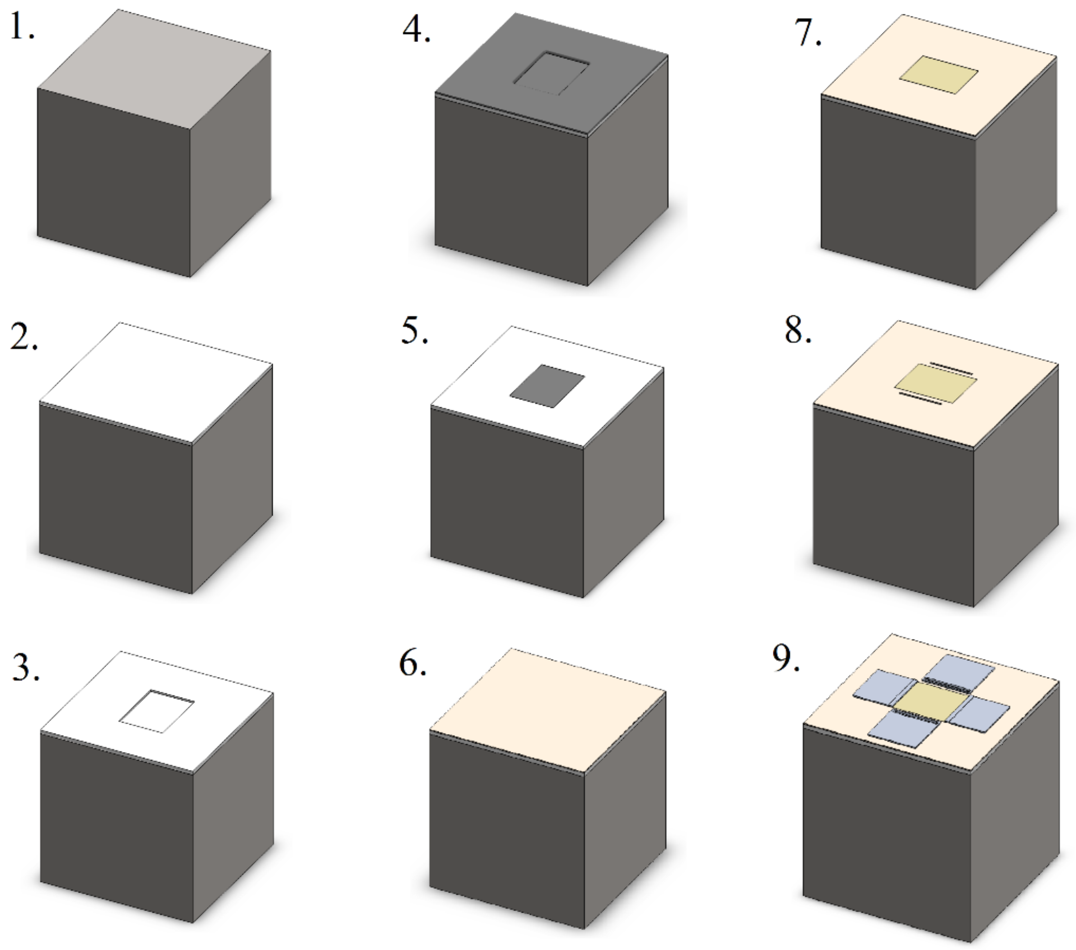

Figure 6.1. Process flow of future work chemical sensor at key points in fabrication.

Each device model above is discussed in detail in the following steps, including processing done which may not inherently change the device structure.

1. Before fabrication is done, an RCA clean (as described in Chapter 3.3) is done to clean the substrate surface (shown in greyish brown) and grow a thin passivating oxide layer to prevent contamination.
2. A 2000-Å oxide layer (shown in white) is grown on the wafer surface via wet oxidation. A proposed oxidation process based on thickness results from furnace recipes utilizing Bruce Furnace Tube #1, is summarized in Table 6.1.

Table 6.1. Proposed wet oxidation process of future work chemical sensors.

Interval	Description	Temperature	Time at Step	N_2 flow rate (lpm)	O_2 flow rate (lpm)	H_2 flow rate (lpm)
0	Boat Out / Load	25°C	N/A	N/A	N/A	N/A
1	Boat In / Push	800°C	12 min	10	0	0
2	Stabilization	800°C	15 min	10	0	0
3	Ramp-up	800°C to 1000°C	20 min	5	0	0
4	Flood	1000°C	5 min	0	10	0
5	Soak	1000°C	40 min	0	3.6	2.0
6	Anneal	1000°C	5 min	15	0	0
7	Ramp-down	1000°C to 800°C	15 min	10	0	0
8	Boat Out / Pull	800°C	15 min	15	0	0

3. Utilizing positive photoresist as an etchant mask, a 23 µm × 32 µm rectangle is imaged on the surface of the oxide and the oxide in the imaged area is etched down 1 µm to make room for the underlying MEMS heater. Using etch rates confirmed for the SMFL website [39], 1 µm of thermally-grown oxide can be etched in roughly two minutes using 10:1 buffered oxide etch at 20.7°C.
4. Two sub-processes are done in this specific step. First, 1 µm of polysilicon (shown in black) is deposited via low-pressure chemical vapor deposition

(LPCVD) to ensure enhanced uniformity. This can be done using a MEMS LPCVD recipe [40] using the SMFL's LPCVD tool with specifications in Table 6.2. The average deposition rate of this process is roughly 200 Å/min.

Table 6.2. MEMS LPCVD polysilicon process parameters.

Temperature (°C)	650°C
Process pressure (mtorr)	300
Reactive gas species	Silane (SiH_4)
Gas flow rate (sccm)	400

In addition, to achieve certain resistance values of the heater which will be further discussed in the next section, the LPCVD polysilicon must be doped via ion implantation using the Varian 350D Implanter. A total dose of 10^{16} cm^{-2} phosphorus is used to ensure a total average dopant concentration of 10^{20} cm^{-3} within the polysilicon layer.

5. A chemical-mechanical planarization (CMP) process using the Strausbaugh CMP tool would most likely be used to create a level polysilicon layer inside the heater region equal to the surrounding oxide layer. The CMP process, including the polish rates with different slurries and processing conditions, must be characterized to ensure the removal of 1 µm of polysilicon.
6. Using LPCVD, a 0.5-µm layer of silicon nitride (shown in light orange) is deposited onto the wafer surface. Silicon nitride ensures optimal heat transfer from the heater to the metal-oxide layer as silicon nitride has higher thermal conductivity compared to basic silicon oxide. A proposed uniform process [40] is explained in Table 6.3. The deposition rate is roughly 55 Å/min.

Table 6.3. Silicon nitride deposition process parameters.

Temperature (°C)	Ramped from door to pump (790°C – 800°C – 810°C)
Process pressure (mtorr)	300
Reactive gas species	Dichlorosilane (SiH_2Cl_2) Ammonia (NH_3)
Gas flow rates (sccm)	60 (SiH_2Cl_2) 150(NH_3)

7. Using a lift-off process similar to what was done with metal-oxide patterning in this thesis described in Chapter 3.5, a 29 µm × 23 µm metal-oxide (shown in dark yellow) rectangle is patterned and placed perpendicular and centered across the polysilicon heater. The longer length is to ensure ample room for metal connections on both sides, which take up 3 µm of length for each. The target thickness of this metal-oxide was designed to be 100 nm as it yielded the most promising sensitivity from results tested in Chapter 5. Assuming a sputter rate and process similar to what was done in Chapter 3.5.2, the deposition would take roughly 25 minutes.
8. 21 µm × 1 µm aluminum contacts (shown in solid grey) would be patterned in the silicon nitride for the polysilicon heater at each end, ensuring a spacing of 1 µm from each of the heater dimensions. Using experimentally-determined etch rates of silicon nitride [41], proposed process parameters for the anisotropic etch of silicon nitride in the Drytek 482 Quad Etcher are presented in Table 6.4. The etch rate of this process is roughly 375 Å/min.

Table 6.4. Proposed silicon nitride etching parameters.

Process pressure (mtorr)	75
Power (W)	600 (@13.56 MHz)
Reactive gas species	Dichlorodifluoromethane (CCl_2F_2) Oxygen (O_2)
Gas flow rates (sccm)	35 (CCl_2F_2) 15 (O_2)

9. As in the previous lift-off process for the metal-oxide, a lift-off process would pattern 23 µm × 23 µm aluminum contacts for both the MEMS heater and metal-oxide sensing layer. A lift-off process is proposed over blanket deposition with wet etch due to either potential contamination of the metal-oxide surface with leftover aluminum or etchant chemicals or over-etch which may remove the metal-oxide layer itself due to its small thickness. To ensure the contact cuts are filled completely, the total deposition thickness of aluminum would be 600 nm; the processing conditions would be the same used in Chapter 3.5.2. Due to the high thickness of aluminum for the lift-off process, more lift-off photoresist should be used to ensure complete lift-off of the metal contacts. Additionally, the same annealing process used in this thesis described in Chapter 3.6 would also be applied to the finished device. Due to the relative low temperature of the annealing process (450°C), phenomena such as dopant migration in the polysilicon is mitigated. At this temperature, it would also allow the aluminum contacts to sinter as done in CMOS processes.

6.2.2 *Electrical Layout / Operational Characteristics*

A 3-D rendered device from SolidWorks, along with the layout designed in Mentor Graphics and associated voltages for each aluminum probe pad, is shown in Figure 6.2.

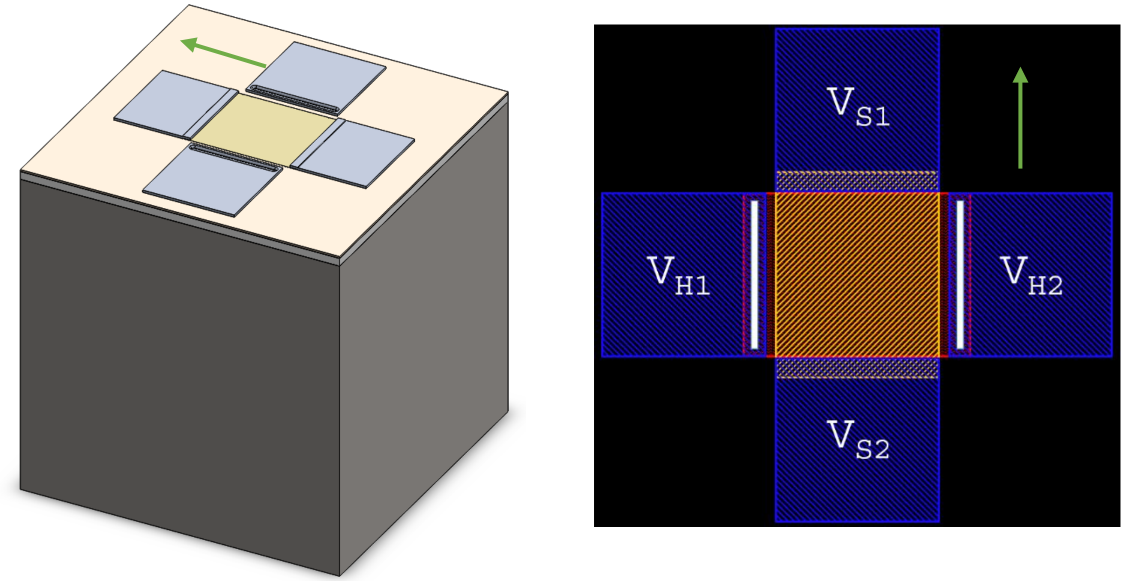

Figure 6.2. 3-D render (left) and IC layout (right) of future work chemical sensor.

V_{S1} and V_{S2} represent the voltages of the probe pads of the metal-oxide sensor; because the metal-oxide layer acts as simple resistor with a direct relationship between voltage and current, the voltage was arbitrarily set at 3 V like the devices fabricated in this thesis. V_{H1} and V_{H2} represent the voltages of the probe pads of the MEMS heater; in operation, V_{H2} would be set to ground. The temperature of the polysilicon heater required to elevate the temperature of the metal-oxide layer to a set temperature (630 K) was determined through a thermal simulation analysis done in SolidWorks. To simplify the mesh of the model, the aluminum contacts were taken out. The steady-state temperature of the exposed surfaces in the model was set at 300 K. The polysilicon heater was assumed to have a consistent temperature on all six faces inside the oxide layer. The analysis was also done using a “worst-case scenario” in which convection from the sensor surface to air was taken into account; the convective heat transfer coefficient was taken to be 27 W/m^2·K [42], which is characteristic of air traveling roughly 5 m/s perpendicular across the surface. The material properties used in this simulation are shown in Table 6.5 and, unless otherwise denoted, were values in predefined materials in SolidWorks.

Table 6.5. Densities and thermal conductivities used for simulated materials.

Material	**Density (kg/m^3)**	**Thermal Conductivity (W/m·K)**
Silicon / Polysilicon	2330	124
Silicon oxide	2648	1.4
Silicon nitride	3170 [34]	18.5 [43]
Indium tin oxide	7140 [44]	11 [44]

Cut-through and top-down views of the temperature simulation are shown in Figure 6.3. Thermal expansion in the simulation was assumed to be negligible as the thermal expansion coefficients of silicon, silicon oxide, and silicon nitride are rather small.

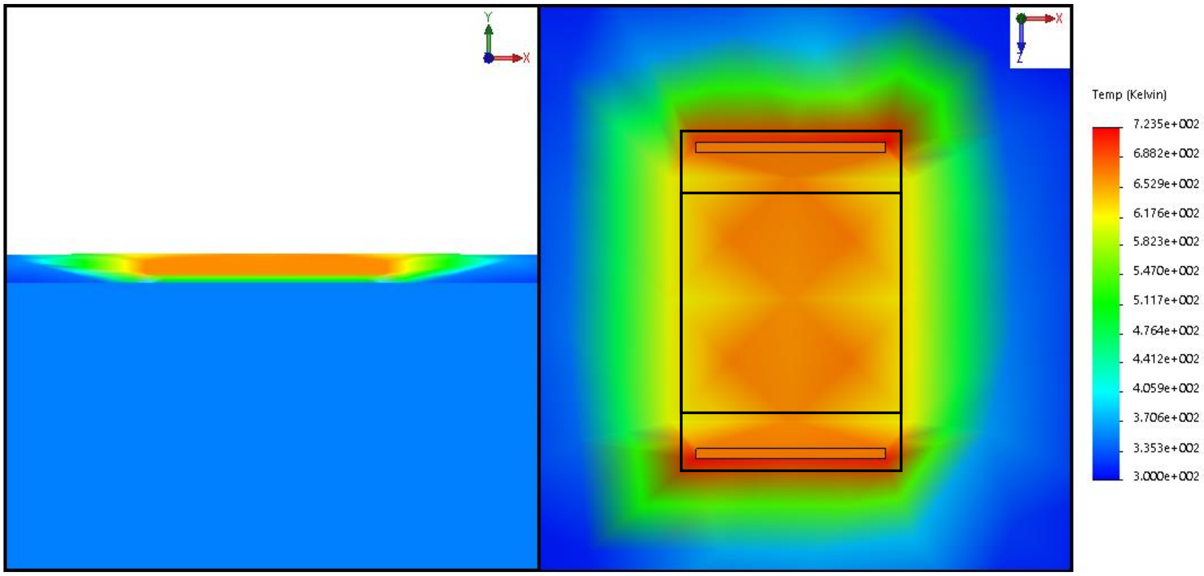

Figure 6.3. Cut-through (left) and top-down (right) temperature distribution of heater.

The temperature output from the MEMS heater was manipulated until the calculated average temperature of the sensor surface was roughly 630 K. It was found the polysilicon heater needed to be roughly 725 K to accomplish this. From here, the required voltage to obtain a temperature of 725 K was back-calculated using relations between thermal resistance with respect to heat transfer through the oxide to the silicon substrate, R_{th}, and power, P, supplied to the resistor itself using Equation 6.1.

$$T_F = T_0 + P \cdot R_{th} \tag{6.1}$$

T_0 and T_F represent the ambient temperature (taken to be 300 K) and the desired temperature, respectively. The power is calculated using a relationship between voltage, V, and resistance, R (Equation 6.2).

$$P = \frac{V^2}{R} \tag{6.2}$$

The resistance of the heater is dependent on the sheet resistance, R_S, the dimensions of the heater (L, W, H), the implanted dose, ϕ, an empirically-determined mobility based on dopant concentration [45], μ, and a correction factor (shown in parentheses in Equation 6.3) which takes grain boundaries of polysilicon into account and assumes an empirically-determined resistance per polysilicon grain boundary, R_{GB}, of 0.9 Ω. It also assumes a grain size of half the polysilicon thickness with a total number of grains equal to the electical path length of the heater divided by the grain size [43] (hence the multiplication of 2 in the numerator). The resistance of the heater was calculated to be roughly 46 Ω.

$$R = \frac{1}{q\mu\phi} \cdot \frac{L}{W} \cdot \left(\frac{2R_{GB}L}{H}\right) \tag{6.3}$$

The thermal resistance is calculated through manipulation of the basic heat conduction equation in Equation 6.4a to 6.4b.

$$Q = kA\frac{dT}{dx} \tag{6.4a}$$

$$\frac{1}{Q}\int_{T_F}^{T_0} dT = \frac{1}{kA}\int_0^d dx \qquad R_{th} \tag{6.4b}$$

Q is the power dissipation (in W), k is the thermal conductivity of silicon oxide (taken to be 1.4 W/m·K from Table 6.5), A is the area of heat transfer (taken to be the area of the bottom of the heater, 23 µm × 32 µm), and d is the distance through which heat is transferred in the material (taken to be the thickness of silicon oxide under the heater, 1 µm). The computation of the left-hand side of Equation 6.4b directly represents the thermal resistance, which has units of K/W. The assumed boundary conditions are $T = T_F$ at $x = 0$ and $T = T_0$ at $x = d$, where d is taken to be the thickness of the oxide under the polysilicon heater. Using this relation, the right-hand side of Equation 6.4b can be calculated to solve for the thermal resistance, which was found to be roughly 1116.1 K/W. Knowing both the heater resistance and the thermal resistance, the voltage and associated power were calculated using Excel's solver function and found to be 4.2 V and 381 mW, respectively. Although this is a relatively easy heater to fabricate, the power required to heat the device is relatively high compared to other MEMS heaters. Ways to mitigate this power loss is to etch underneath the heater itself to expose it to air [46] or run it in a power-compensated pulsed mode which can significantly reduce the amount of power [47]. Running the heater in a power-compensated mode is feasible as the required time to heat the sensor to the required temperature is small due to the small mass of the polysilicon and have been achieved in heaters similar in scale with pulses of 1 ms every second [46].

6.3 Silvaco Atlas Electrical Simulation of Chemical Sensor

The chemical sensor was electrically simulated using Silvaco Atlas to undertand the effects of physical parameters on change of resistance. The simulation structure, testing conditions, and summaries of the effects of metal-oxide thickness and oxygen vacancy concentration on changes of resistance are described in this section. The effects of annealing the metal-oxide layer were not studied due to the complexity of modeling adsorption sites with respect to fixed charge in Silvaco Atlas. Additionally, the effects of change of temperature on reaction kinetics were also not investigated as it would require an advanced model to portray how the amount of alcohol reacted (assumed to be a fixed charge set on the metal-oxide surface) changes with temperature; each sensitivity simulation was tested with discrete values of fixed charge on the metal-oxide surface.

6.3.1 2-D Silvaco Atlas Device Structure

The device itself was designed to have an metal-oxide path length of 23 µm which was exposed to air. Like the device processing discussed earlier, the aluminum contacts were 600 nm thick and placed with 2 µm of overlap on the ITO layer. The heater was not put into the device structure; instead, the temperature of the simulation was set externally to set the temperature of the metal-oxide layer. The ITO material properties, including the density of states (taken to be the same for the conduction and valence bands, $N_{CV} = N_{CC}$), bandgap (E_g), electron mobility (μ_n), and oxygen vacancy concentration (N_{OV}), were taken from a publication [10] which utilized a similar sputtering method and deposition thickness; these properties are summarized in Table 6.6. These aforementioned parameters, along with the values in Table 6.6, were set as default values to compare subsequent simulations to. The device structure is shown Figure 6.4 with an ITO thickness of 100 nm.

Table 6.6. ITO material properties used in Silvaco Atlas simulations.

$N_{CV} = N_{CC}$ (cm^{-3})	2.3×10^{19}
E_g (eV)	3.5
μ_n (cm^2/V·s)	40
N_{OV} (cm^{-3})	9×10^{20}

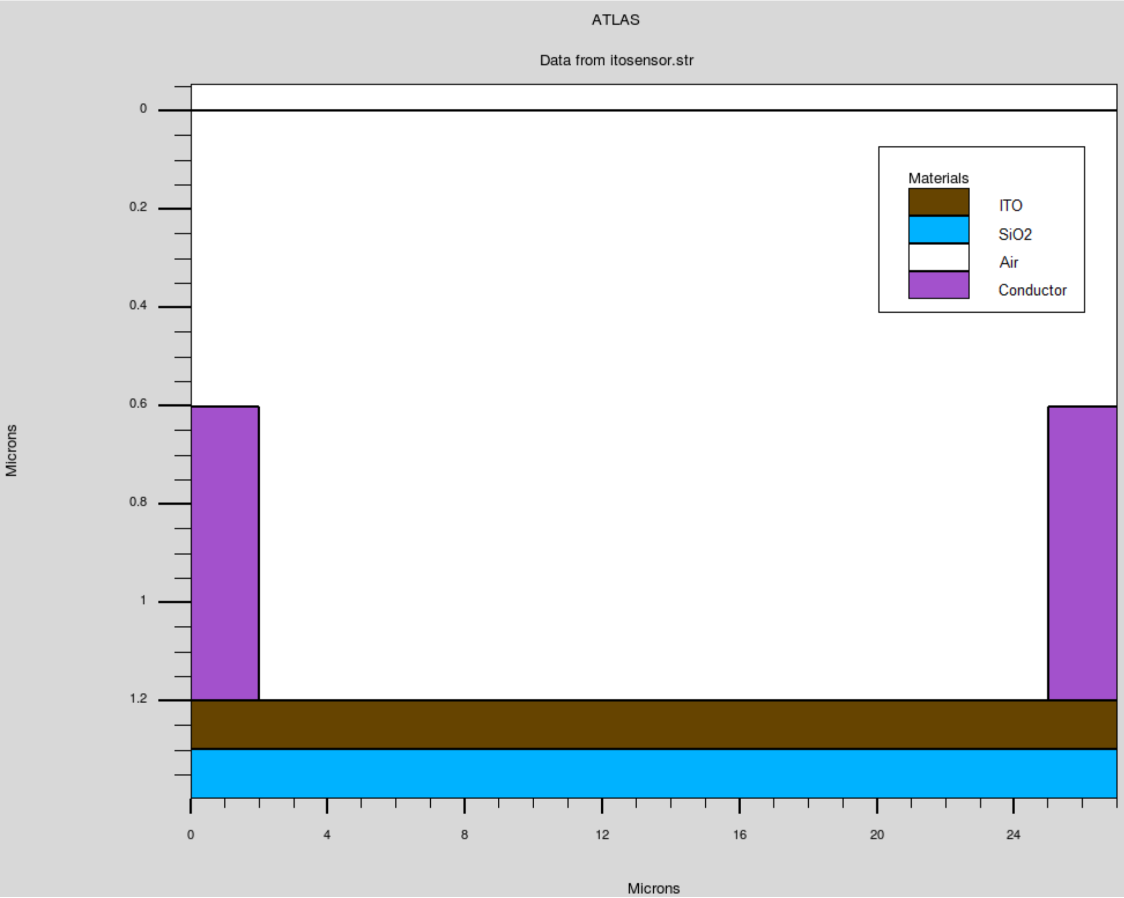

Figure 6.4. Silvaco Atlas chemical sensor device structure.

The oxygen vacancy concentration, N_{OV}, was set close to the metal-oxide surface at an energy level equal to the bandgap of the material. The device was modeled using the Fermi model to study temperature effects. For each simulation, the voltage was swept from 0 V to 4 V and, using the resulting I-V curve, the resistance using Ohm's Law was determined. However, the current values obtained at each voltage value represent current per micron of length; to determine the actual resistance value, the current was multiplied by the length into-the-page of the sensor. Because the length and width of the metal-oxide sensor were the same, the calculated resistance was equal to the sheet resistance of the material. The steady-state sheet resistance, at a temperature of 300 K with parameters taken from Table 6.6 and a "base" interfacial fixed charge (Q_{ss}) of 10^{11} cm^{-2}, was roughly 117.6 Ω/sq. This value is similar to sheet resistance values obtained via characterization of the ITO material in Chapter 4. Thus, this sheet resistance value was taken to be the default. However, each simulation was done at an elevated temperature of 625 K to best reflect device operating conditions. Each simulation study is summarized in the sections below.

6.3.2 Simulated Electrical Effects of ITO Thickness

Keeping the parameters described in Table 6.6 constant, the metal-oxide thickness was varied at thicknesses of 10 nm, 100 nm, and 500 nm to understand how thickness affects sensitivity as interfacial fixed charge changes. Using the sensitivity equation described in Chapters 2 and 5, sensitivity was calculated with the steady-state value of resistance taken to be at an interfacial fixed charge of 10^{11} cm^{-2}. The resulting sensitivity curves at each aforementioned thickness is summarized in Figure 6.5.

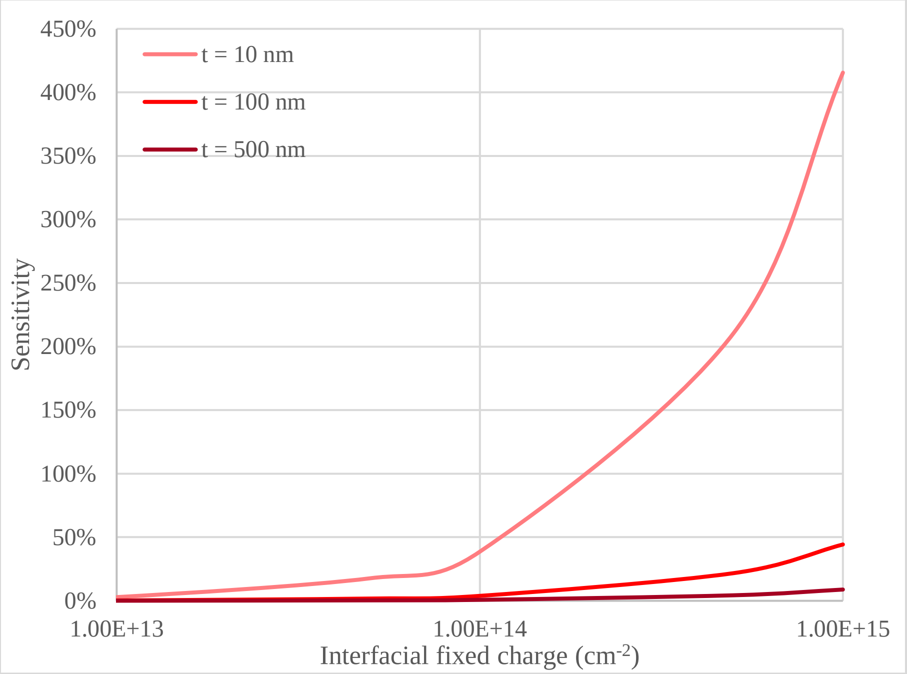

Figure 6.5. Sensitivity at different metal-oxide thicknesses with changes in Qss.

As confirmed from experimental findings in Chapter 5, decreasing the thickness of the metal-oxide layer significantly improves the sensitivity of the device as the interfacial fixed charge increases. This is due to the fixed charge with respect to the total mass of the metal-oxide layer; as the thickness increases, the presence of surface charges are mitigated as there is already substantial current flow throughout the thickness of metal-oxide layer. Although there is great potential for thinner metal-oxide films for chemical sensors, pitting in the sensing material begins to form at lower thicknesses [17] and may potentially cause shorting of the electrical path in the metal-oxide. Thus, it is crucial to find the correct balance of overall sensitivity and film continuity.

6.3.3 Simulated Electrical Effects of Oxygen Vacancies

A material characteristic that was not investigated in the fabricated devices was the effects of oxygen vacancy concentration on sensitivity. The oxygen vacancy concentration essentially describes how conductive or insulative the metal-oxide material is. In practice, ways of increasing the oxygen vacancy concentration is via reactive sputtering in an oxygen. The oxygen vacancy concentration, assuming other parameters held constant, was varied with increasing conductive nature at concentrations of 9.0 × 10^{19} cm^{-3}, 9.0 × 10^{20} cm^{-3}, and 9.0 × 10^{21} cm^{-3}. These simulations are summarized in Figure 6.6.

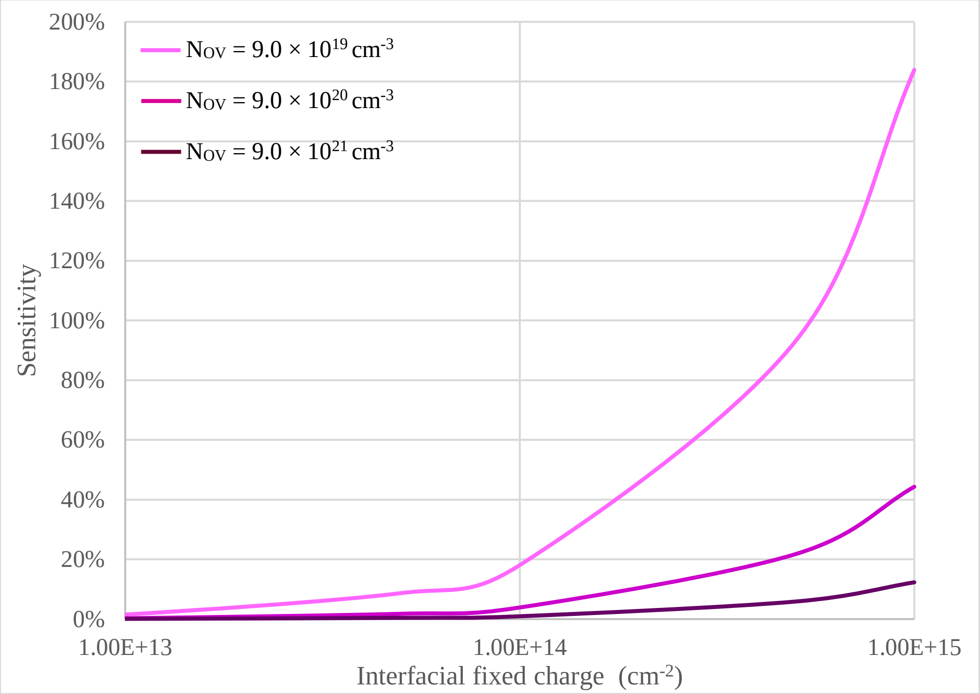

Figure 6.6. Sensitivity at different NOV with changes in Qss.

As demonstrated, decreasing the oxygen vacancy concentration in the metal-oxide layer increases the sensitivity as the interfacial fixed charge increases. This may be due to a greater percent change in electron carriers of a highly-resistive metal-oxide compared to that of a conductive metal-oxide. The effect is very similar to the effect of thickness on sensitivity, but not as exaggerated; as the resistance of the electrical path decreases, the ability of the sensing material to detect subtle changes of electron carriers from the interfacial fixed charge also decreases. In addition to these simulations, the percent change of resistance with respect to a change of temperature at different oxygen vacancy concentrations was also studied keeping other device parameters constant. The resistance values were taken for each material at 300 K given a "base" interfacial fixed charge of 10^{11} cm^{-2}. These results are shown in Figure 6.7.

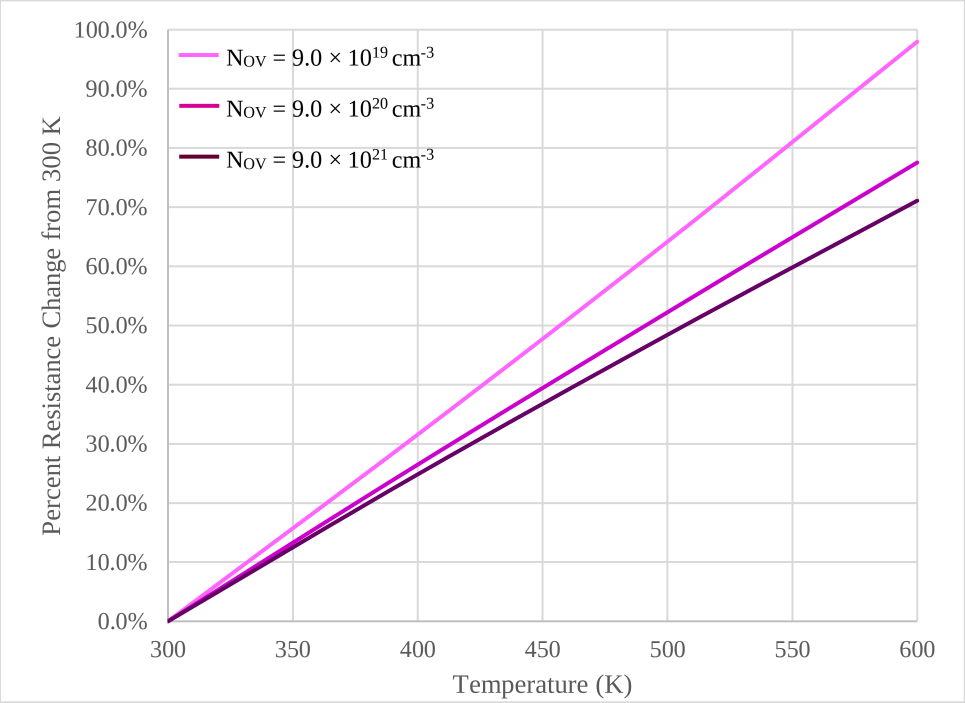

Figure 6.7. Percent resistance change with change of temperature.

Although lower oxygen vacancy concentrations yield higher sensitivity to the interfacial fixed charge, they will also result in higher resistance fluctuations with changes of temperature. Thus, it is crucial to ensure the sensing material is kept at a relatively constant temperature with the polysilicon heater to ensure false positives or negatives are mitigated if there are slight fluctuations in power from the heater to the metal-oxide. With that being said, there exists an inherent tradeoff between sensitivity from change oxygen vacancy concentration and need for precise electronics to ensure the temperature of the metal-oxide is kept at a constant value.

6.4 Conclusion

The design of a micrometer-scaled chemical sensor using metal-oxide sensing technology was discussed, including a feasible way of fabricating the device using tools available in the SMFL. In addition, basic electrical operating characteristics of the device, including the sensing layer and the polysilicon heater, were found and discussed using both SolidWorks thermal simulations and Silvaco Atlas electrical simulations. The basic device was modeled in Silvaco Atlas with similar properties to what was found in ITO material characterization in Chapter 4; in addition, oxygen vacancy concentration was analyzed as a potential parameter which can be further investigated in future work via reactive sputtering of ITO in the presence of oxygen.

Chapter 7

Potential Areas for Future Work

7.1 Introduction

This chapter discusses three potential future work concepts, other than fabrication of the sensor design described in Chapter 6, which can be investigated further. Initial starting points of each concept are given.

7.2 Analyzing Different Metal-Oxide Materials / Additives

This thesis focused on the incorporation of n-type ITO films to sense reducing gases. However, there are a variety of other metal-oxide materials that can be used to sense a variety of reducing gases that have been documented in literature.

7.2.1 Metal-Oxide Materials

Other metal-oxides have been documented in literature to be sensitive to either reducing or oxidizing gases. Highly-conductive n-type metal oxides, such as gallium oxide (Ga_2O_3), aluminum oxide (Al_2O_3), zinc oxide (ZnO), vanadium oxide (V_2O_3), and other stable transition metals, have been proven to be sensitive to reducing gases such as nitrous oxide [5] with similar reaction characteristics to the ITO tested in this thesis. In addition, a variety of other n-type composite materials have also been studied and have proven to work more effectively compared to each specific material. Material systems which facilitate each portion of a catalytic reaction have been hypothesized to be more efficient than single components. In a study done on a SnO_2 / ZnO composite, research has found that, in the catalytic reaction of butanol to the composite material, the tin oxide most effectively dehydrogenated the butanol to butanal and, subsequently, the zinc oxide catalyzes the butanal so electrons in the chemisorbed oxygen can be reinjected [48]. This synergy allows for both higher and faster rates of reaction of the analyte to the sensing material and, ultimately, higher sensitivity. However, further characterization of these metal-oxides must be done to fully understand the effects of each constituent in a metal-oxide material system with regards to the role it plays in catalysis of a given analyte. P-type metal-oxide materials, such as perovskite compounds (i.e. $LaCoO_3$, $NdCoO_3$) have been found to be effective at detecting oxygen and harmful gases normally found in mining/petroleum refining environments such as carbon monoxide, nitrous oxide, and sulfurous oxide [9]. In addition, p-type materials may pave the way towards lower operating temperatures as they have been found to be more sensitive to reducing gases at low temperatures relative to n-type materials [49]; lower operating temperatures allows for power reduction of the sensor microsystem and practical applications in wearable technology. However, to test these devices, it is important to ensure a safer testing apparatus in a well-ventilated area as the effects of the aforementioned gases are much more hazardous compared to ethanol.

7.2.2 Noble Metal Functionalization

Metal-oxides are favored for their ability to both act as a semiconductor in integrated circuitry and serve as a catalyst for redox reactions. However, to further enhance the sensitivity of a metal-oxide chemical sensor, precious metal nanostructures of palladium, gold, and platinum can be deposited on the surface of the metal-oxide to facilitate catalytic reactions. The precious metal structures usually participate in the splitting of the oxygen for the initial sensitizing reaction required for subsequent analyte reaction. The functional mechanism is highly debated, but it is proposed it to be based equally on both electronic and catalytic phenomena. Precious metals are able to easily dissociate oxygen due to their overabundance of electrons that atmospheric oxygen is able to adsorb with; after dissociation, the high-energy oxygen radicals formed on the precious metal structures are transferred to the metal-oxide surface via charge transfer where they are subsequently adsorbed. An example of a proposed mechanism of these phenomena is shown in Figure 7.1 [50].

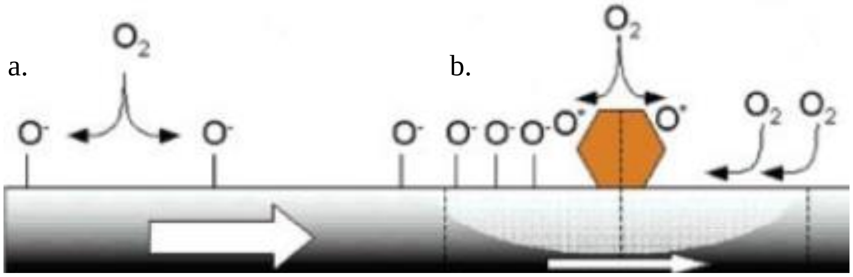

Figure 7.1. Normal (a) adsorption compared to noble metal (b) adsorption.

An easy, cost-effective method of fabricating these precious metal structures is through nanosphere lithography. Nanosphere lithography is a type of lift-off process which utilizes a self-assembling mask of polystyrene nanospheres which, when coated with lift-off resist and subsequently removed, leave a holed pattern in the lift-off photoresist which can be used to fabricate precious metal particles. The size of the holes can be varied via reactive ion etch of the polystyrene balls. Although work has been done to characterize the process in the SMFL clean room [51], further development into the process must be done to ensure robust fabrication techniques for geometrically-constrained surfaces such as the metal-oxide sensing layer.

7.3 Development of Metal-Oxide Nanostructures

As discussed in Chapter 2, surface-area-to-volume ratio is crucial in ensuring enough active space for the sensitizing reaction to take place. Although as-deposited ITO crystallites have a significantly higher surface-area-to-volume ratio than annealed ITO crystallites, the benefits are mitigated due to their closely-packed nature which limits the available adsorption surface area to the geometric surface of the layer. Some research has been done in an effort to increase the available surface area for the sensitizing reaction via metal-oxide nanostructures. Perpendicular nanostructures to the sensor surface, as demonstrated in Figure 7.2 [52], allow for greater surface area for oxygen adsorption in geometrically-constrained metal-oxide layers, which is important as the pressing need for increasingly smaller devices with high surface area grows.

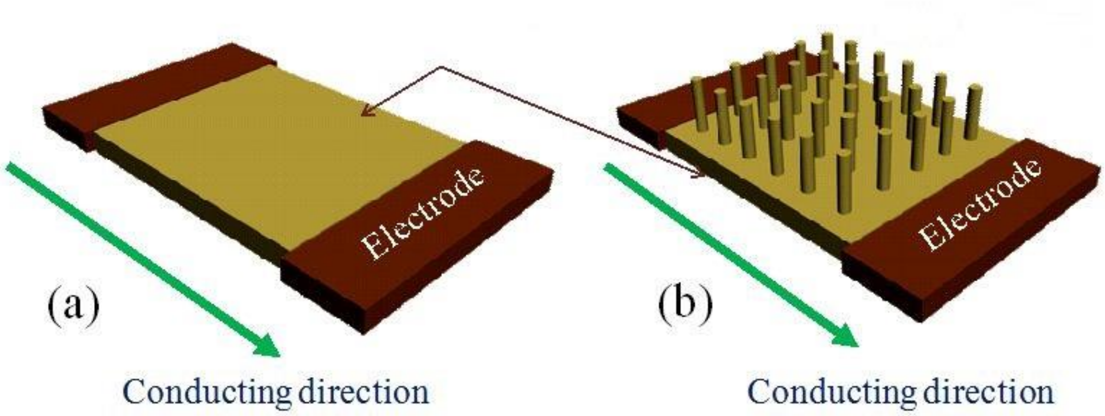

Figure 7.2. Geometric (a) surface area compared to nanostructured (b) surface area.

Fabrication techniques utilizing vapor-liquid-solid (VLS) growth have been used to grow certain metal-oxides. The process normally uses nanoscale precious metal surface particles as a catalyst which are placed directly on the substrate surfaces. At high temperatures, the metal-oxide is evaporated in a crucible via electron beam evaporation and, through atomic supersaturation of the metal-oxide material in the catalyst metal, the nanowire is growth underneath the catalyst particle as the temperature of the metal-oxide reaches the catalyst's melting point [53].

7.4 Determination of Chemical Identity via Metal-Oxide Sensors

The focus of this thesis was to analyze the responses of a variety of chemical sensors to a certain analyte at a variety of concentrations. A future study could be done regarding the selectivity of the devices with respect to certain chemicals. However, it has been shown in publications [49] that metal-oxide chemical sensors have poor selectivity as any reducing gas will reinject electrons trapped by the adsorbed oxygen. At high temperature ranges of operation, several gases may have the potential of reacting with the chemisorbed oxygen. Two methods, discussed further in the following subsection, have the potential ability of determining the identity of the analyte.

7.4.1 "E-tongue" Technology

The changes of sensitivity to similar organic compounds (i.e. alcohols, ketones) may be hard to detect due to their similarity in chemical reaction regarding their functional groups. The ability to detect this change may be subtle and inconclusive to the actual analyte determination. In certain biological microsystems, the poor selectivity of metal-oxide materials is exploited and multiple metal-oxide materials are utilized in an array which outputs multiple electrical signals from each metal-oxide. Due to several material parameters such as active surface area, catalytic activity (dependent on temperature), and band gap, the ability of metal-oxides to detect both reducing and oxidizing gases is unique. Creating an array of different metal-oxide layers can allow for higher-dimensional data collection which may give distinct characteristic signals as opposed to just one. Some publications have been able to create an array of metal-oxide materials to detect air pollutants (i.e. CO, NO_2, SO_2) out of both n-type and p-type materials with optimal operating temperatures for each sensing material [54].

7.4.2 Pulsed Electrical Testing

If the geometrical surface area of the sensing region is constrained and an array of metal-oxides cannot be fabricated, pulsed electrical testing can be done on the sensor's heater to determine the identity of an analyte. Each gas has a unique optimal temperature of oxidation which is dependent on stereochemistry, molecular weight, and functional group. Because of this, accurately varying the temperature (in the form voltage change) of the heater will yield different responses for each unique analyte. These electrical signals can be processed via fast Fourier transform (FFT). One publication has demonstrated that applying a rectangular waveform on the heater, which varied from 1 V, 3V, and 5V on packaged tin oxide chemical sensor devices, yielded different electrical signals when exposed to ethanol, benzene, isopropyl alcohol, isoamyl alcohol, and 1-butanol [55].

7.5 Conclusion

Potential ideas of future work, including utilizing different metal-oxide materials and noble metal additives, forming metal-oxide nanostructures for geometrically-constrained sensing regions for surface area enhancement, and formulating device structures and testing methods for analyte determination, were discussed. The importance of material selection for metal-oxides, including what makes optimal composite metal-oxide materials, was discussed. The importance of noble metals' effects on sensitivity enhancement, and a potential way of fabricating noble metal nanodots, were both discussed. The enhancement of sensitivity in geometrically-constrained metal-oxide layers via nanostructures, including a method of fabricating nanowires/nanocolumns, were both discussed. The formulation of an "E-tongue" and electrical tests that can be done to determine the identity of an analyte, were discussed.

Chapter 8

Executive Summary of Thesis Research

8.1 Overall Summary and Conclusions

The research undertaken in this thesis project was to understand the effects of both device and testing parameters on sensitivity of metal-oxide chemical sensors. Before any fabrication work was done, initial research was done to determine key parameters that have been found to greatly affect the sensitivity of n-type metal-oxide gas sensors to volatile organic compounds. In addition, to realize how each parameter affects device sensitivity, a literature research was done to understand how the sensing mechanism works in this type of technology, including models and assumptions taken to characterize the sensitizing reaction and subsequent chemical reaction of the analyte. Research was also done regarding metal-oxide material selection and what makes favorable candidacy of certain materials as chemical sensing layers.

A basic metal-oxide chemical sensor, including a robust and predictable fabrication process, were both developed with ease of device testability in mind. The device was designed in millimeter-scale to ensure that both the active area was large enough for reactivity to most certainly occur and the metal connections were large enough to probe to without the use of a microscope. This scale also ensured easy fabrication techniques without the use of the photolithography stepper machines in the clean room which were also consistently down throughout the semester. The basic fabrication process consisted of a basic thermal oxide growth and two lift-off processes for both the metal-oxide and aluminum layers. Although this type of device would not be incorporated into an actual microsystem due to the external heater required to heat the large device, it allowed for rapid prototyping for device testing and mitigated wait time from commonly-used machines and process modules in the clean room.

Characterizing the metal-oxide was found to be a crucial component of the thesis research as it determined crucial properties which made devices either more or less sensitive. The important conclusions obtained from the material characterization were mostly from the effects of annealing the metal-oxide. Annealing the metal-oxide in inert conditions yielded larger grain structures and more of a presence of indium oxide's base-centered cubic structure, cubic bixbyite, via XRD analysis and the Scherrer equation. Both of these properties are crucial in metal-oxide chemical sensor development, as the former ensures ample surface area for the sensitizing reaction to occur and the latter ensures relatively low resistance values in which changes of reinjected carriers can easily be output as electrical signals.

Both chemical testing procedures undertaken in this thesis yielded crucial results regarding device functionality and how device/testing parameters affected overall sensitivity. The first testing procedure, consisting of short-exposure to an ethanol/water mixture, demonstrated how annealed ITO samples had slightly improved sensitivity compared to as-deposited ITO. In addition, the change of sensitivity from the point of maximum signal output to the metal-oxide's steady-state resistance demonstrated the increase of surface area of annealed ITO compared to as-deposited ITO when compared with the theory behind the Langmuir isotherm model. Larger changes of sensitivity, which can be related to the amount of available oxygen adsorption sites defined in the isotherm model, are characteristic of materials with large surface areas and was concluded with the results obtained for the annealed ITO compared to the as-deposited ITO. The increase of adsorption sites also allowed for larger concentrations to be detected as low-surface area metal-oxide devices were oversaturated which caused reaction-rate limitations with respect to the adsorbed oxygen. Lastly, the effects of the larger grain sizes also affected the activation energies of electrical conduction when exposed to ethanol. Because the material's activation energy was dependent on temperature, the activation energy was found via Arrhenius relationships of each temperature zone and was found to increase with temperature which could be due to greater oxygen adsorption at higher temperatures.

Thickness was also found to be another crucial aspect of analyte sensitivity due to the mass-transfer limited adsorption of oxygen within one Debye length into the metal-oxide surface. In the prolonged exposure tests, it was found that shrinking this metal-oxide thickness increased both the maximum sensitivity and the range of sensitivity values with different analyte concentrations. This ultimately allowed for easier signal processing of the resulting change of conductivity of the metal-oxide layer.

The sensitivity of the devices tested was found to increase with an increase of the analyte rate of reaction which was dependent on both the concentration of analyte and operating temperature. Both the sensitizing adsorption reaction of oxygen and subsequent analyte reaction requires high temperatures to take place so it is crucial for the device to be operated at an elevated temperature. At lower temperatures, the sensitivity dropped significantly due to either lower amounts of oxygen adsorption or incomplete analyte reaction which may have led to the blocking of oxygen adsorption sites. In addition, with basic characteristics of Le Châtelier’s principle, adding more analyte pushes the oxidation process to the right and subsequently increases the rate of reaction, leading to higher sensitivity measurements.

A variety of future work building off what was done in this thesis has been presented, including the design of a micrometer-scale chemical sensor device which utilizes a built-in MEMS heater rather than the external heater used to heat the proof-of-concept chemical sensors tested. In addition, a plausible fabrication process along with theoretical characterization of the device via thermal and electrical simulations done in SolidWorks and Silvaco Atlas, respectively, were all discussed and have given reasonable results regarding the simplicity of the device design. Other than the effects of metal-oxide thickness in the electrical simulations done in this thesis, the manipulation of oxygen vacancy concentration has been examined as well; it was found that decreasing the oxygen vacancy concentration led to higher sensitivity values but at the cost of increased fluctuation with temperature. This leads to a trade-off between sensitivity and regulation of temperature control within the MEMS heater.

Other future work topics that can be examined further are the use of other metal-oxides and precious metals for analyte detection, metal-oxide nanostructure integration for enhanced surface area in geometrically-constrained areas in microsystems, and abilities of chemical identification via metal-oxide layer arrays through an “E-nose” or via pulsed electrical signaling of the chemical sensor’s heater to both classify analytes based on their oxidation at a variety of temperatures and mitigate operational power.

References

[1] Global Industry Analysts, "Chemical sensors market trends," 9 December 2016. Available: http://www.strategyr.com..

[2] H. Patel, "Sensor Used in E-nose," in *The Electronic Nose: Artificial Olfaction Technology*, Springer India, 2014, pp. 143-180.

[3] E. E. Bassey, "Development and Characterization of Metal Oxide Gas Sensors, PhD Dissertation," Auckland University of Technology, New Zealand, 2014.

[4] B. Szulczyński and J. Gebicki, "Currently Commercially Available Chemical Sensors Employed for Detection of Volatile Organic Compounds in Outdoor and Indoor Air," *MDPI Journals: Environmental,* 6 March 2017.

[5] E. Kanazawa, G. Sakai, K. Shimanoe, Y. Kanmura, Y. Teraoka, N. Miura and N. Yamazoe, "Metal Oxide Semiconductor Nitrous Oxide Sensor for Medical Use," *Sensors and Actuators B,* pp. 72-77, 2001.

[6] L. Filipovic and S. Selberherr, "Performance and Stress Analysis of Metal Oxide Films for CMOS-Integrated Gas Sensors," *MDPI Journals: Sensors, 15,* 25 March 2015.

[7] J. Ding, T. J. McAvoy, R. E. Cavicchi and S. Semancik, "Surface state trapping models for SnO2-based microhotplate sensors," *Sensors and Actuators B,* pp. 597-613, 2001.

[8] V. S. Vaishnav, P. D. Patel and N. G. Patel, "Indium Tin Oxide thin film gas sensors for detection of ethanol vapours," *Thin Solid Films 490,* pp. 94-100, 26 July 2005.

[9] G. Korotcenkov, "Metal oxides for solid-state gas sensors: What determines our choice?," *Materials Science and Engineering B, 139,* pp. 1-23, 2007.

[10] S. A. Bashar, "Study of Indium Tin Oxide (ITO) for Novel Optoelectronic Devices, PhD Dissertation," University of London, Department of Electronic Engineering, London, 1998.

[11] N. Hishimoto, Y. Yamada, Y. Ohnishi, N. Imawaka and K. Yoshino, "Effect of temperature on the electrical properties of ITO in a TiO2/ITO film," *Physica Status Solidi A 210, No.3,* pp. 589-593, 27 November 2012.

[12] S. H. Brewer and S. Franzen, "Calculation of the electronic and optical properties of indium tin oxide by density functional theory," *Chemical Physics 300,* pp. 285-293, 21 November 2003.

[13] W. Zachariasen, "The Crystal Structure of the Modification C of the Sesquioxides of the Rare Earth metals, and of Indium and Thallium," *Norsk Geologisk Tidsskrift, 9,* pp. 310-316, 1927.

[14] N. Nadaud, N. Lequeux and M. Nanot, "Structural Studies of Tin-Doped Indium Oxide (ITO) and In4Sn3O12," *Journal of Solid State Chemistry 135,* pp. 140-148, 1998.

[15] R. Lal, in *Encyclopedia of Soil Science*, New York, Taylor & Francis Group, L.L.C., 2006, p. 1088.

[16] S. Chandra, H. J. Pandya and A. L. Vyas, "ITO Thin Films by RF Sputtering for Ethanol Sensing," in *First International Conference on Sensor Device Technologies and Applications*, Rome, 2010.

[17] E. Guo, H. Guo and H. Lu, "Structure and characteristics of ultrathin indium tin oxide films," *Applied Physics Letters, Vol.98, Issue 1,* January 2011.

[18] S. Goyal and V. VasanthiPillay, "Influence of Sputtering Power, Annealing on the structural properties of ITO films, for Application in Ethanol Gas Sensor," *Materials Today: Proceedings 2,* pp. 4609-4619, 2015.

[19] L. Fuller, "Wafer Cleaning and Oxide Growth Laboratory," 21 September 2010. [Online]. Available: https://people.rit.edu/lffeee/1st_oxide.pdf.

[20] Clariant Corporation, "AZ nLOF 2000 Series i-Line Photoresists Datasheet," AZ Electronic Materials, 2002.

[21] L. Fuller, "Physical Vapor Deposition - Evaporation and Sputtering," 26 November 2013. [Online]. Available: https://people.rit.edu/lffeee/PVD_Recipes.pdf.

[22] D. R. Pelleymounter, D. J. Christie and B. D. Fries, "Pulsed DC Power for Magnetron Sputtering: Strategies for Maximizing Quality and Flexibility," *Society of Vacuum Coaters, Inc.,* p. 1, 2014.

[23] S. O'Brien, "Tencor SpectraMap Manual," 2014. [Online]. Available: http://www.smfl.rit.edu/pdf/manual/Manual_Prometrix_SpectraMap.pdf.

[24] W. Callister, in *Materials science and engineering: an introduction, Chapter 3,* New York, John Wiley & Sons, 1997.

[25] F. Bloss, "Indexing Powder Patterns for Cubic Materials," Virginia Polytechnic Institute, Blackburg, 1969.

[26] Powder Diffraction File, "ITO Material Properties," International Centre for Diffraction Data, 2017.

[27] E. Andrei, "Experiments in Modern and Applied Physics, Lecture 2," Rutgers University, 2011.

[28] Y. Liu, G. Štefanić, J. Rathousky, O. Hayden, T. Bein and D. Fattakhova-Rohlfing, "Assembly of Mesoporous Indium Tin Oxide Electrodes from Nano-Hydroxide Building Blocks," *Royal Society of Chemistry, Electronic Supplementary Material (ESI) for Chemical Science,* 2014.

[29] B. E. Warren, X-ray Diffraction, New York: Dover Publications, Inc., 1990.

[30] S. O'Brien, "Amray 1830 Scanning Electron Microscope Manual," 18 March 2016. [Online]. Available: http://www.smfl.rit.edu/pdf/manual/Manual_Amray_1830_SEM.pdf.

[31] N. Barsan and U. Weimar, "Conduction Model of Metal Oxide Gas Sensors," *Journal of Electroceramics*, pp. 143-167, 2001.

[32] MicroChemicals, "AZ nLOF Negative Resist Complement Information for Processing," 07 November 2005. [Online]. Available: http://www.microchemicals.com/technical_information/az_nLof_20xx_additional_informations.pdf.

[33] E. Traversa, "Ceramic sensors for humidity detection: the state-of-the-art and future developments," *Dipartimento di Scienze e Tecnologie Chimiche, Universita di Roma,* 1994.

[34] W. M. Haynes, "CRC Handbook of Chemistry and Physics (92nd Ed.)," Boca Raton, CRC Press, 2011, p. 3.246.

[35] PubChem Project, "Ethanol Properties," National Center for Biotechnology Information, 2013.

[36] B. C. Yadav, R. Srivastava, C. D. Dwivedi and P. Pramanik, "Moisture sensor based on ZnO nanomaterial synthesized through oxalate route," *International Symposium on Olfaction and Electronic Noses, Vol. 131, Issue 1,* pp. 216-222, 14 April 2008.

[37] J. Black, "Electromigration - A Brief Survey and Some Recent Results," *IEEE Transactions on Electron Devices, Ed.16, No.4,* April 1969.

[38] M. Sobri, A. Shuhaimi, K. M. Hakim, V. Ganesh, M. H. Mamat, M. Mazwan, S. Najwa, N. Ameera, Y. Yusnizam and M. Rusop, "Effect of annealing on structural, optical, and electrical properties of nickel (Ni) / indium tin oxide (ITO) nanostructures prepared by RF magnetron sputtering," *Superlattices and Microstructures, 70,* pp. 82-90, 2014.

[39] S. O'Brien, "Wet Etch Rates," 30 July 2013. [Online]. Available: https://wiki.rit.edu/display/smfl/Wet+Etch+Rates.

[40] L. Fuller and B. Tolleson, "Low Pressure Chemical Vapor Deposition," 26 November 2013. [Online]. Available: https://people.rit.edu/lffeee/LPCVD_Recipes.pdf.

[41] B. D. Pant and U. S. Tandon, "Etching of Silicon Nitride in CCL2F2, CHF3, SiF4, and SF6 Reactive Plasma: A Comparative Study," *Plasma Chemistry and Plasma Processing, Vol.19, No.4,* 3 February 1999.

[42] The Engineering Toolbox, "Convective Heat Transfer," 2013. [Online]. Available: http://www.engineeringtoolbox.com/convective-heat-transfer-d_430.html.

[43] L. Fuller, "Resistors: Heaters and Temperature Sensors," 30 January 2017. [Online]. Available: https://people.rit.edu/lffeee/resistor_mems.pdf.

[44] Umicore, "Indium Tin Oxide (ITO) for deposition of transparent conductive oxide layers," 2013. [Online]. Available: http://www.thinfilmproducts.umicore.com/Products/TechnicalData/show_datenblatt_ito.pdf.

[45] T. Kamins, M. Chan and R. Muller, Device Electronics for Integrated Circuits, 2nd Edition, Wiley & Sons, 1986.

[46] Q. Zhou, A. Sussman, J. Chang, J. Dong, A. Zettl and W. Mickelson, "Fast response integrated MEMS microheaters for ultra low power gas detection," *Sensors and Actuators A223,* pp. 67-75, 3 January 2015.

[47] W. Hwang, K. Shin, J. Roh, D. Lee and S. Choa, "Development of Micro-Heaters with Optimized Temperature Compensation Design for Gas Sensors," *MDPI Journals: Sensors, 11,* pp. 2580-2591, 1 March 2011.

[48] C. L. Zhu, Y. J. Chen, R. X. Wang, L. J. Wang, M. S. Cao and X. L. Shi, "Synthesis and Enhanced Ethanol Sensing Properties of α-Fe2O3/ZnO Heteronanostructures," *Sensors and Actuators B,* pp. 185-189, 2009.

[49] X. Liu, S. Cheng, H. Liu, S. Hu, D. Zhang and H. Ning, "A Survey on Gas Sensing Technology," *MDPI Journals: Sensors, 12,* pp. 9635-9665, 16 July 2012.

[50] C. Wang, L. Yin, L. Zhang, D. Xiang and R. Gao, "Metal Oxide Gas Sensors: Sensitivity and Influencing Factors," *Sensors (Basel) 10(3),* pp. 2088-2106, 15 March 2010.

[51] X. Lei, "Development of Nanosphere Lithography for Semiconductor Device Applications, Master's Thesis," Rochester Institute of Technology, Kate Gleason College of Engineering, Rochester, 2016.

[52] S. Choopun, N. Hongsith and E. Wongrat, "Metal-Oxide Nanowires for Gas Sensors," in *Nanowires - Recent Advances*, Chiang Mai, Thailand, Chiang Mai University, 2012.

[53] H. Yu and J. Lee, "Growth mechanism of metal-oxide nanowires synthesized by electron beam evaporation: A self-catalytic vapor-liquid-solid process," *Scientific Reports, 4, Article Number: 6589,* 10 October 2014.

[54] C. S. Prajapati, R. Soman, S. B. Rudraswamy and N. Bhat, "Single Chip Gas Sensor Array for Air Quality Monitoring," *Journal of Microelectromechanical Systems PP(99),* February 2017.

[55] R. Chutia and M. Bhuyan, "Study of Temperature Modulated Tin Oxide Gas Sensor and Identification of Chemicals," in *5th International Congress on Image and Signal Processing Proceedings, pg.181*, Chongqing, 2012.

Appendix A

Sensitivity versus Time Graphs of Chemical Sensors in Prolonged Exposure to Ethanol

A.1 Sensor Exposures to Ethanol at 160°C

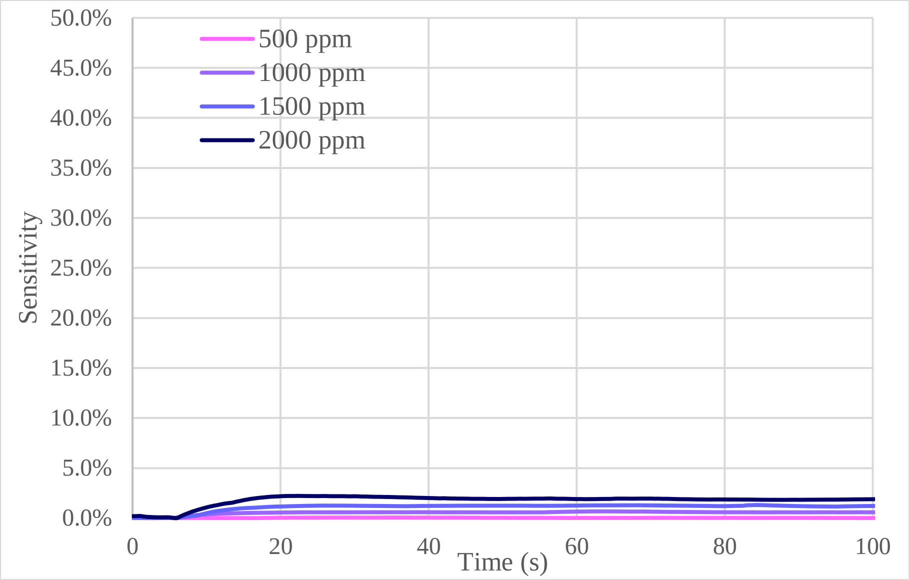

Figure A.1. 100-nm, annealed ITO response to prolonged EtOH conc. at 160°C.

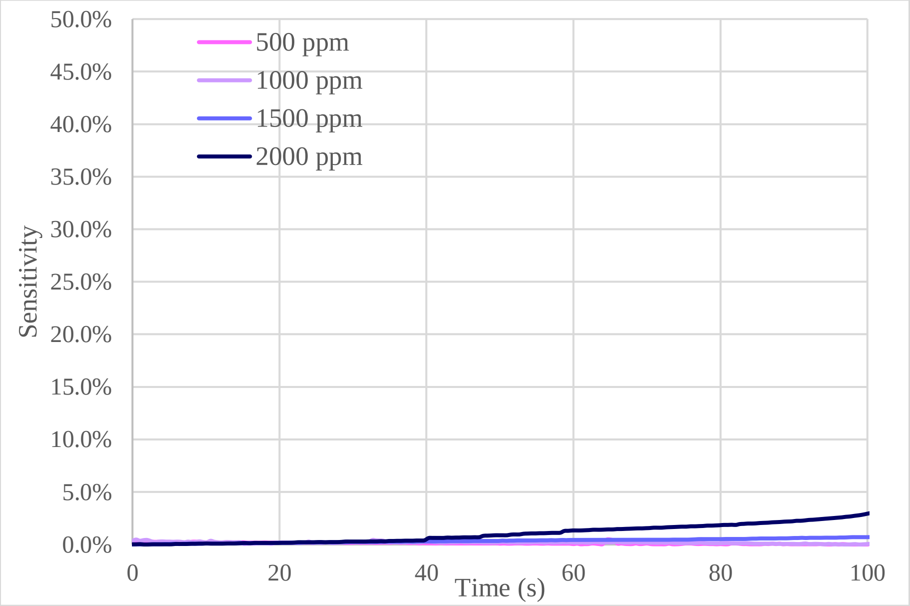

Figure A.2. 100-nm, as-deposited ITO response to prolonged EtOH conc. at 160°C.

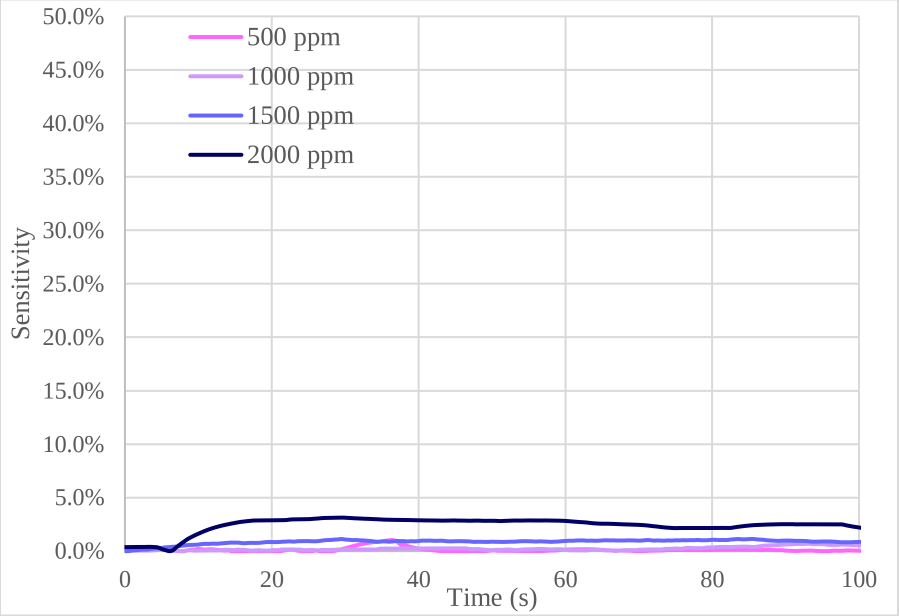

Figure A.3. 400-nm, annealed ITO response to prolonged EtOH conc. at 160°C.

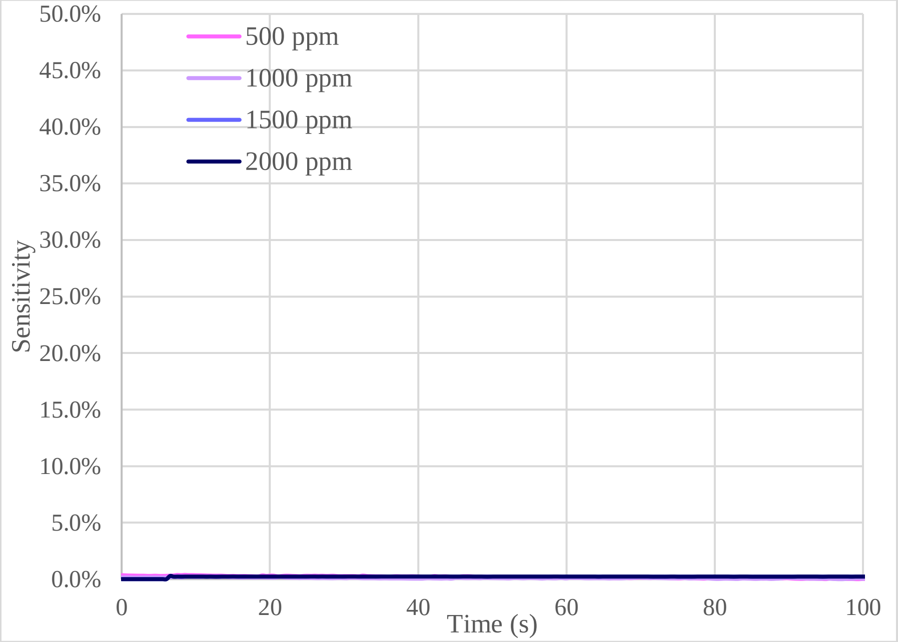

Figure A.4. 400-nm, as-deposited ITO response to prolonged EtOH conc. at 160°C.

A.2 Sensor Exposures to Ethanol at 260°C

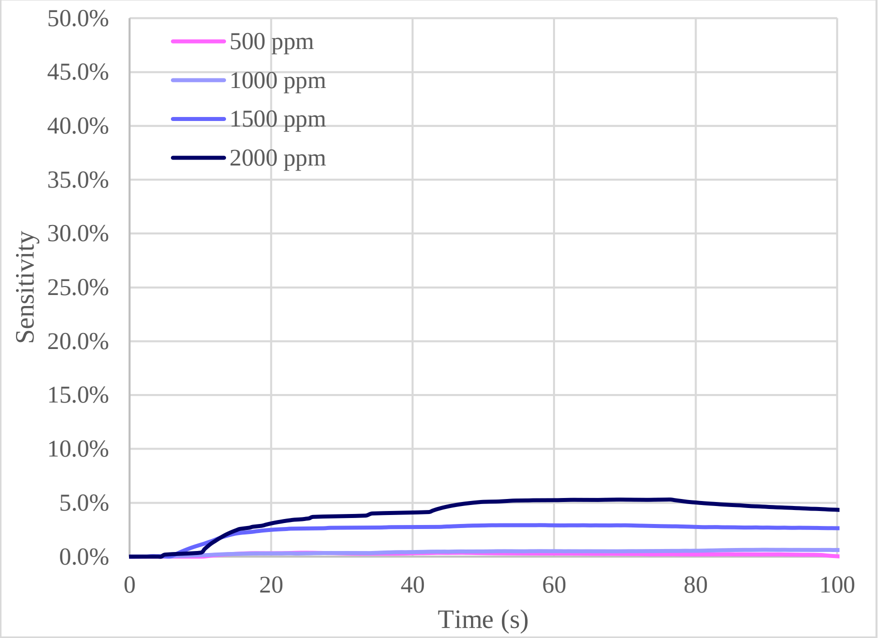

Figure A.5. 100-nm, annealed ITO response to prolonged EtOH conc. at 260°C.

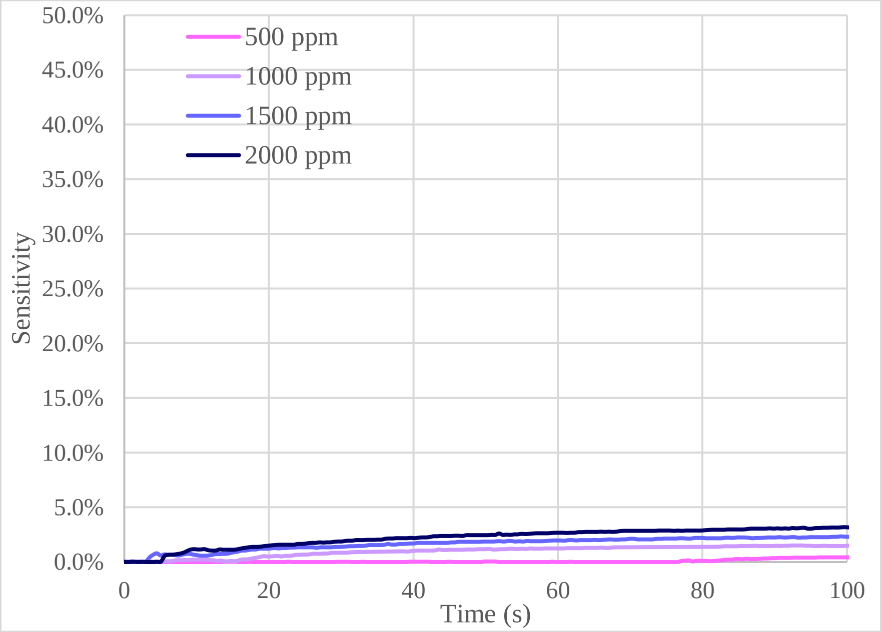

Figure A.6. 100-nm, as-deposited ITO response to prolonged EtOH conc. at 260°C.

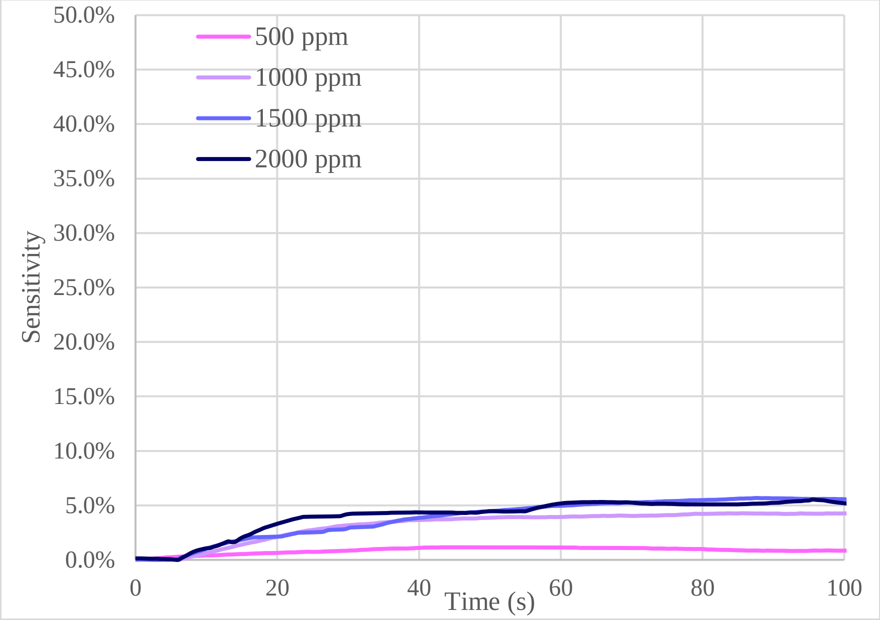

Figure A.7. 400-nm, annealed ITO response to prolonged EtOH conc. at 260°C.

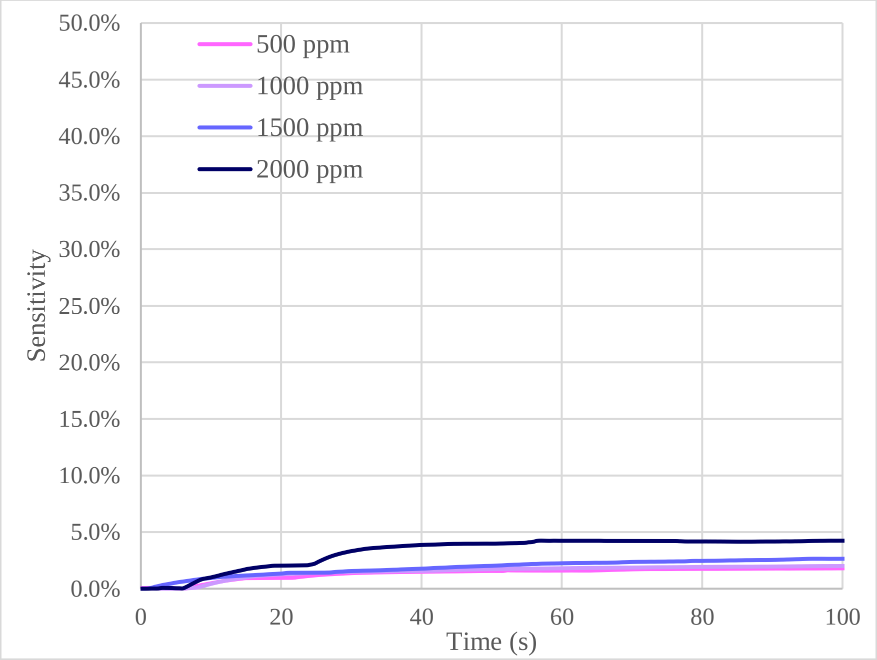

Figure A.8. 400-nm, as-deposited ITO response to prolonged EtOH conc. at 260°C.

A.3 Sensor Exposures to Ethanol at 360°C

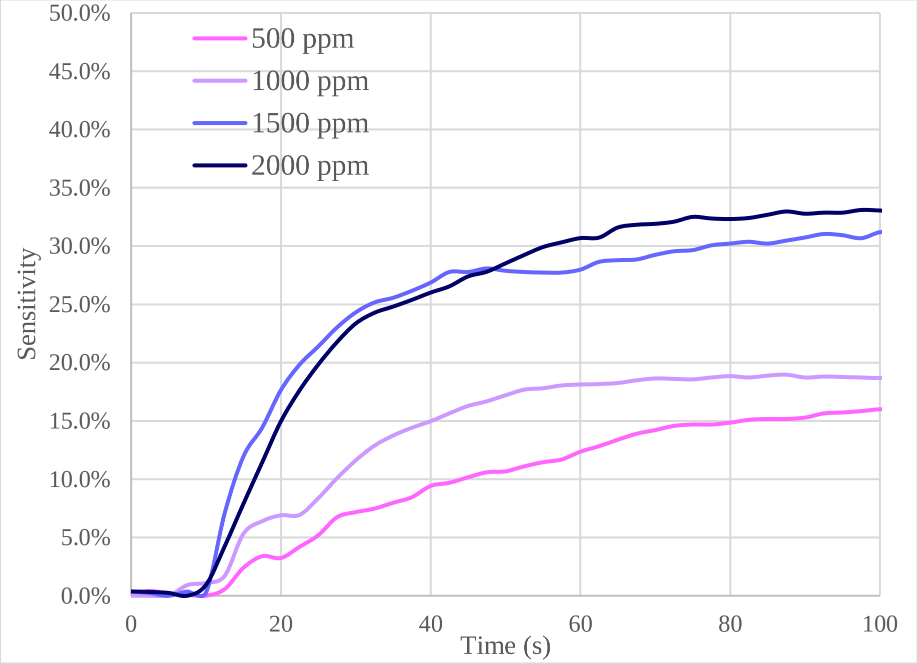

Figure A.9. 100-nm, annealed ITO response to prolonged EtOH conc. at 360°C.

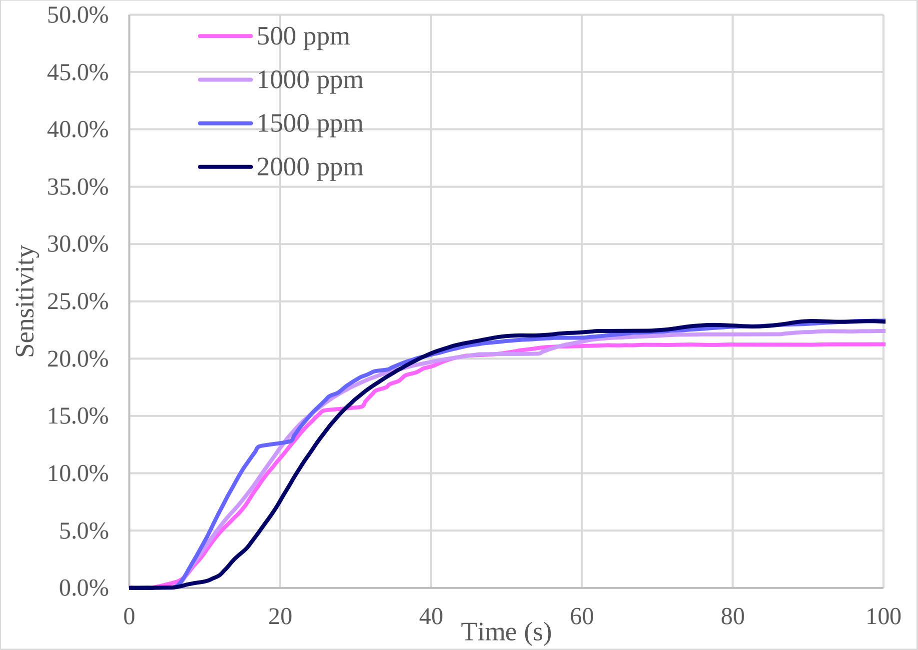

Figure A.10. 100-nm, as-deposited ITO response to prolonged EtOH conc. at 360°C.

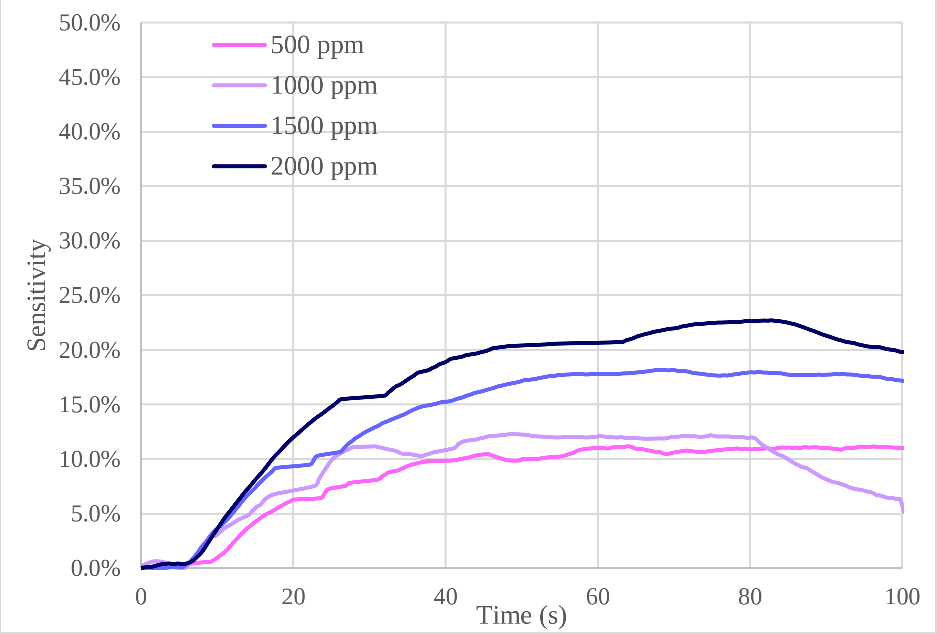

Figure A.11. 400-nm, annealed ITO response to prolonged EtOH conc. at 360°C.

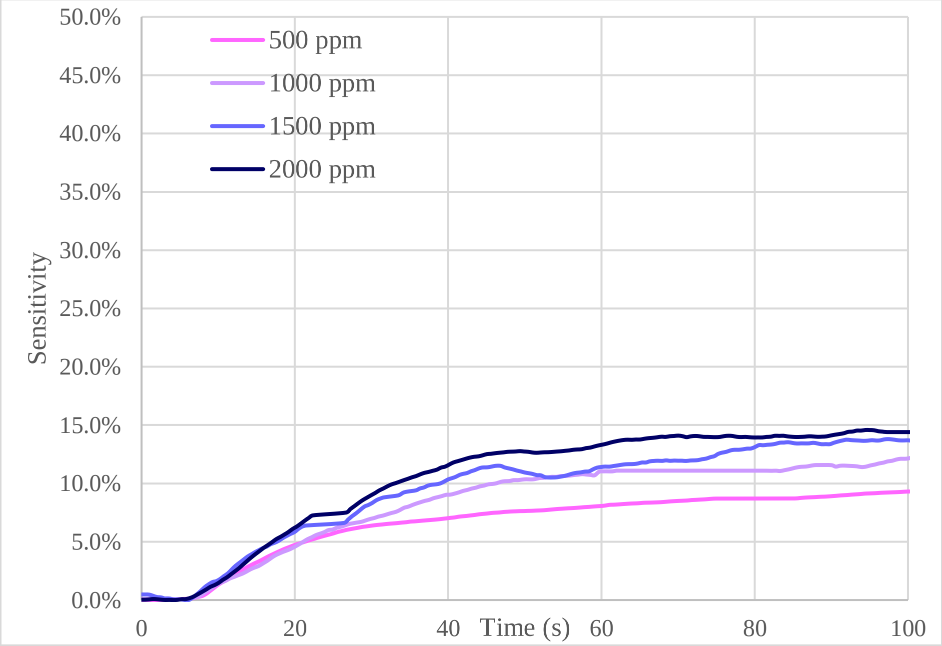

Figure A.12. 400-nm, as-deposited ITO response to prolonged EtOH conc. at 360°C.

Appendix B

Silvaco Atlas Simulation Code for Future Work Chemical Sensor

```
go atlas simflags="-P 8"

############## BG

# Set Variables
#----ITO Thickness (um)
set T=0.1
#----Channel Length
set L=23
#----“S/D-gate Overlay"
set OL=2
#----Gate dielectric thickness
set BGI=0.1
#----Top gate dielectric thickness
set TGI=1.2
#----Density of Oxygen Vacancies (OV), donor type
set nov=9e20
#---------- Fixed charges, ITO Surface
set qf=5e11
#-----------Capture cross-section
set sig=1e-15
#-----------Temperature
set temp=300

# Mesh Outfile Statement

mesh width=1 master.out

x.m l=0 s=0.25
x.m l=2*$"OL"+$"L" s=0.25
y.m l=0 s=0.01
y.m l=$"TGI" s=0.001
y.m l=$"TGI"+$"T" s=0.001
y.m l=$"TGI"+$"T"+$"BGI" s=0.01


# Define ITO
region num=1 material=ito y.min=$"TGI" y.max=$"TGI"+$"T"
region num=2 material=sio2 y.min=$"TGI"+$"T"
y.max=$"TGI"+$"T"+$"BGI"
region num=3 material=vacuum y.max=$"TGI"

# elec num=1 name=gate bottom
elec num=1 name=source y.max=$"TGI" y.min=$"TGI"/2 x.min=0.0
x.max=$"OL"
elec num=2 name=drain  y.max=$"TGI" y.min=$"TGI"/2 x.min=$"OL"+$"L"
x.max=2*$"OL"+$"L"
```

```
# “S/D” Contacts
contact num=1 workf=4.28
contact num=2 workf=4.28


models fermi print temp=$temp


# Set ITO Parameters
material region=1 mun=35 nc300=1e20 nv300=1e20 eg300=3.5

# Defects
# Bulk defects
trap donor e.level=3.5 density=$"nov" degen=1 sign=$"sig"
sigp=$"sig"
#defects nga=0.0 ngd=$"nov" egd=3.4 wgd=0.1

# ITO fixed charge on surface
interface y.min=$"TGI" y.max=$"TGI" qf=$"qf"

method autonr climit=1e-4 carrier=1 electron

#structure outfile=itosensor.str
#tonyplot itosensor.str

# Id-Vd

log outf=L=$"L"-T=$"T"_qf=$"qf"_nov=$"nov"_temp=$"temp".log
solve vdrain=0 vstep=0.1 vfinal=4 name=drain

log off

quit
```